HIGH-SPEED MILLIMETER-WAVE ACTIVE INCOHERENT FOURIER DOMAIN IMAGING

By

Stavros Vakalis

A DISSERTATION

Submitted to
Michigan State University
in partial fulfillment of the requirements
for the degree of

Electrical Engineering – Doctor of Philosophy

2022

ABSTRACT

HIGH-SPEED MILLIMETER-WAVE ACTIVE INCOHERENT FOURIER DOMAIN IMAGING

By

Stavros Vakalis

Millimeter-wave imaging is used in applications such as security screening, remote sensing, medical imaging, and non-destructive testing due to the good penetration characteristics of millimeter-wave radiation which can provide "see-through" capabilities. Electromagnetic signals in the frequency range of 30 - 300 GHz can penetrate easily through materials like clothing, fog, and smoke, and at the same time provide image reconstruction with fine spatial resolution. Millimeter-wave imaging is typically implemented by means of mechanical or electrical scanning which requires long data acquisition times or a large number of active components. Computational imaging can reduce both the data acquisition time and the number of active components, but this comes at the cost of heavy computational loads, which makes real-time operation challenging. Passive millimeter-wave imaging systems that capture thermal signals and operate similarly to optical cameras, are very costly because they need to employ highly sensitive receivers due to thermal radiation being extremely low power at millimeter-wave frequencies. A paradigm shift is needed in order to advance the current imaging modalities in millimeter-wave frequencies.

In this dissertation, I present a newly developed millimeter-wave imaging technique called active incoherent millimeter-wave (AIM) imaging which combines the benefits of active and passive millimeter-wave imaging. This approach combines the high signal-to-noise ratio capabilities of active millimeter-wave imaging systems with the fast image formation potential of passive millimeter-wave imaging systems. The combination is achieved by illuminating the scene with multiple spatially distributed noise transmitters that mimic the randomness of thermal radiation. Because the concept of incoherent noise illumination has not been investigated thoroughly in the literature of millimeter-wave imaging, I discuss design considerations for creating a space-time incoherent transmitter and novel measurements for characterizing space-time incoherence. Start-

ing from my earlier work in microwave frequencies, I present the system design and calibration approach, along with an experimental demonstration of a millimeter-wave active incoherent digital array. The array is capable of generating millimeter-wave video at very high frame rates, and millimeter-wave imaging results of 652 frames per second of a sphere moving in a pendulum motion are included. The scenario of using the stray reflections from a small set of communications transmitters is also examined and I present results using WiFi and fifth-generation (5G) communications signals. I also expand interferometric imaging to three dimensions using a novel pulse modulation as an envelope on the noise signals to provide differentiation along the range dimension. Prior to this work, three-dimensional interferometric millimeter-wave imaging had only been implemented in the near-field region or using three-dimensional volumetric arrays, which pose significant size and volume concerns. A new algorithm for three-dimensional interferometric image formation is presented along with simulated results and experimental measurements.

ACKNOWLEDGEMENTS

I would like to thank, first and foremost, my advisor, Dr. Jeffrey A. Nanzer, for guiding me through the PhD journey. Since my first semester at Michigan State University, he has provided a significant amount of his time for guidance on my research and advice for future career goals and opportunities. His support has helped me explore a variety of topics and advance myself as a researcher and a person.

I am thankful to the Electromagnetics Research Group Faculty, Dr. Edward Rothwell, Dr. Shanker Balasubramaniam, Dr. Premjeet Chahal, and Dr. Leo Kempel who have helped me significantly through this journey and were always there in my talks and presentations and they were always available for a short talk. I would like to thank my other committee members, Dr. Ming Yan and Dr. Selin Aviyente for giving me valuable feedback and helping me with research questions. I am also thankful to Dr. John Papapolymerou for his help and time during the graduate school experience and Brian Wright who helped me with multiple experimental setups and fabrication of structures and equipment.

I am grateful to the student members and postdoctoral researchers of the Electromagnetics Research Group and fellow Michigan State University graduate students. Namely, I want to thank Serge Mghabghab, Xenofon Konstantinou, Liang Gong, Anton Schlegel, Daniel Chen, Jorge R. Colon-Berrios, William Stevers, Saranraj Karuppuswami, Saikat Mondal, Eric Klinefelter, Yuxiao He, John Doroshewitz, Jason Merlo, Abdel Alsnayyan, Omkar Ramachandran, Sean Ellison, Neda Nourshamsi, Mohammed Rashid, Jacob Randall, Ahona Bhattacharyya, Amer Abu Arisheh, William Torres, Cory Hilton, Michael Craton, Vincens Gjokaj, Chris Oakley, Mohd Ifwat Mohd Ghazali, Jennifer Byford, and everyone else who was part of the group while I was there and made graduate school a fun experience.

I want to thank Dr. Panagiotis Cottis who supervised my Diploma thesis in National Technical University of Athens and helped me prepare for my graduate studies and career. I also want to acknowledge the National Science Foundation for funding my graduate studies and research, the

IEEE Microwave Theory and Techniques Society for honoring me with the Tom Brazil Graduate Fellowship, and the IEEE Antennas and Propagation Society for entrusting me with the Doctoral Research Grant. Their support has been very valuable.

Last but not least, I want to thank my family, friends, and my fiancée Sofia for their support and for believing in me during my graduate studies. I do not know where I would be without them.

TABLE OF CONTENTS

LIST OF TABLES

LIST OF FIGURES

CHAPTER 1

INTRODUCTION

1.1 Microwave and Millimeter-Wave Imaging

Imaging refers to the process of creating visual representations using observations from sensors. It has traditionally been an optical technique, using light sources and signals in the visible spectrum, but imaging in general can take place with all kinds of waves including X-rays [16], microwaves [17], ultrasound [18] and seismic waves [19]. Imaging using electromagnetic waves has attracted a lot of interest since the work of Christiaan Huygens in optics where he described light as a wave [20]. It was some centuries later that James Clerk Maxwell's research predicted that electromagnetic waves can propagate at the known speed of light [21]. Some years after that, Heinrich Hertz published the experimental demonstration that showed that electromagnetic signals can travel at the same speed as optical signals, as Maxwell had predicted [22]. Despite the fact that electromagnetic and optical signals share the same nature, imaging efforts focused mostly on optical frequencies, due to the availability of ambient light sources. Interest in microwave and millimeter-wave frequencies became more evident before and during World War II, where the deployment of some of the first actual radar systems took place including the Chain Home, developed by the United Kingdom Royal Air Force and the Freya radar developed by the Germans.

Nowadays, microwave and millimeter-wave imaging systems are used in a plethora of applications that require good penetration capabilities such as contraband detection [23, 24], remote sensing [25], medical imaging [26, 27], and non-destructive testing [28]. Microwave (3 - 30 GHz) and millimeter-wave (30 - 300 GHz) frequencies represent a unique space for imaging due to the very good propagation characteristics of the radiation in these bands. Materials that are nontransparent at optical and infrared wavelengths, including smoke, fog, and clothing, among others, have minimal or very low loss at millimeter-wave frequencies [29]. Furthermore, recent advances in microwave and millimeter-wave hardware design and fabrication have made millimeter-wave com-

ponents significantly more efficient and affordable [30], making the implementation of such imaging systems significantly cheaper. Due to the aforementioned reasons, although millimeter-wave imaging has been traditionally an unfathomed area, it has recently attracted significant research and commercial interest.

Various approaches have been developed for imaging at microwave and millimeter-wave frequencies, including mechanically-scanning systems and phased arrays [31, 32]. Mechanically-scanning imagers usually utilize a single large antenna that is raster-scanned to each spatial location representing a pixel in the image. While such systems can require only a single transceiver, their size requirements and their image formation time are often significantly larger when compared to other methods. Phased arrays electronically scan the beam, however such systems utilize many antenna elements and active components, requiring significant power consumption and system complexity. Microwave and millimeter-wave holography techniques have been implemented [23, 33], however these systems require long data acquisition time to produce high resolution images along with multi-element antenna arrays.

Millimeter-wave imagers such as focal plane arrays [34, 35] form images in a staring fashion without the need for beam scanning, however these approaches generally require quasi-optical apertures such as lenses or reflector antennas and a large array of detectors which increase the total system cost and size. Computational imaging approaches can reduce the number of active components, but utilize computationally expensive image formation algorithms, which leads to long image formation time [36]. While the number of measurement modes is reduced in computational imaging, the total aperture area is still large, which can still lead to large systems.

Most of the above forms of microwave imaging require a large aperture that is fully or mostly filled, which can result in large occupied areas and high cost. This requirement has led recently to interest in sparse array interferometric imagers which sample the scene information in the spatial frequency domain rather than the spatial domain. First developed in radio astronomy, interferometric imagers utilize sparse antenna arrays [37], resulting in a significant reduction in the number of elements, aperture size and weight compared to other imaging techniques. More recently, such

imagers have been developed primarily for security imaging purposes due to the fact that the interferometric image reconstruction necessitates that the incident electromagnetic fields be spatially and temporally incoherent. Thermal radiation generated by the human body, as well as the radiation from celestial bodies, satisfies this requirement, and furthermore human radiation has generally higher power than the environmental objects to enable the detection of the shapes of objects hidden beneath a person's clothing, for example. The drawback of passive interferometric imagers is that thermal emissions have extremely low power at millimeter-wave frequencies, and therefore interferometric imagers have to employ very high sensitivity receivers, which are costly.

The current state of the art of millimeter-wave imaging systems can be characterized with multiple inefficiencies including:

1. Slow operation: Many current millimeter-wave imaging techniques necessitate long data acquisition or image formation times. For many applications, including security screening, this means that they cannot operate in real-time.

2. Bulky systems: Most techniques utilize a large antenna aperture which is fully-populated or almost fully-populated. This results in systems with significantly large dimensions that exhibit space and weight concerns.

3. Significantly high system cost: Due to the large number of active components and the use of significantly large apertures, the cost of many millimeter-wave imaging systems tend to be prohibitive for many commercial applications.

1.2 Overview of Microwave and Millimeter-Wave Imaging Techniques

1.2.1 Mechanically Scanning Millimeter-Wave Imagers

Mechanically scanning imagers utilize an electric motor drive to raster scan the antenna response in the spatial domain as it is shown in Fig. 1.1. These systems can utilize single-antenna transmit and receive configurations or more complicated antenna array configurations. In general, the

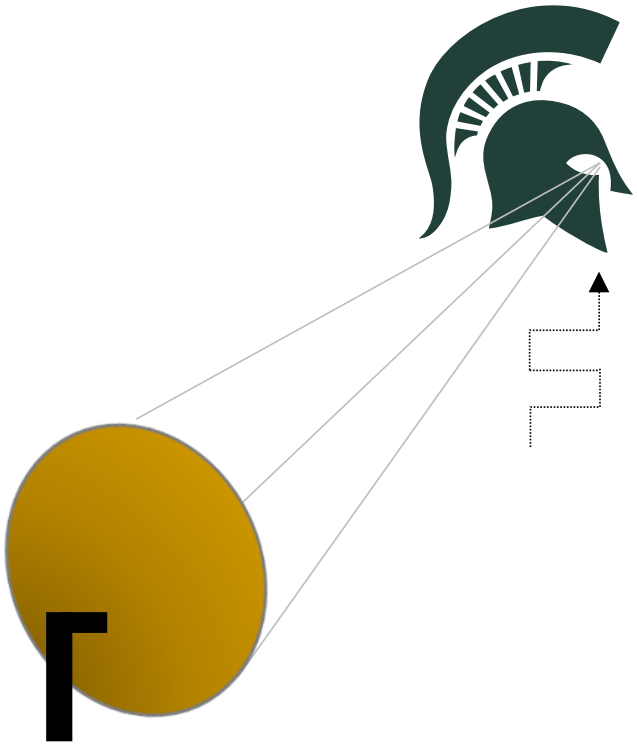

Figure 1.1: Conventional mechanical scanning imagers focus the radiated energy at a specific point in space and raster-scan the antenna beam in space to form an image.

cost of mechanically scanning imagers tends to be lower than the other imaging modalities' cost, discussed in the following paragraphs, due to the reduced requirements in active radio-frequency hardware. Nevertheless, mechanical scanning is slow, and this translates to slow data acquisition and image formation speed. This is the most significant drawback of these imagers, which makes them prohibitive for most real-time imaging applications of moving targets. Another challenge is that mechanical vibrations, which happen due to the scanning motion, may be a large fraction of a wavelength at millimeter-wave frequencies. Additionally, the electric motor that performs the mechanical scanning is the most common point of failure, which can make the system non-operational for scanning. Finally, these systems usually tend to utilize large platforms which results in bulky and heavy systems.

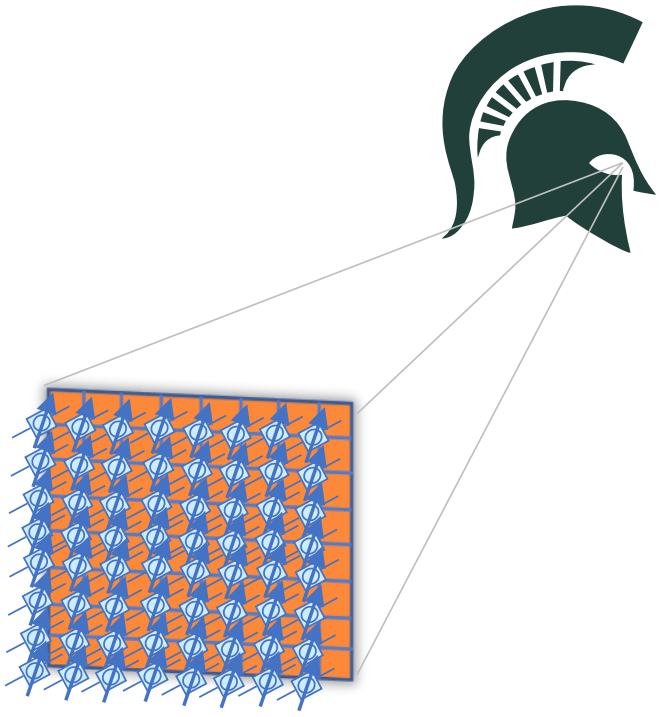

Figure 1.2: Electronically scanning imagers focus the radiated energy at a specific point and scan the beam in the spatial domain using phase shifts.

1.2.2 Electronically Scanning Millimeter-Wave Imagers

Electronically scanning imaging systems utilize an array of antennas, whose relative phase is controlled, in order to scan the spatial domain. The most famous electronically scanning imaging system is that of a phased array [31, 38, 39], which utilizes a large amount of active components in order to perform these phase shifts. Active millimeter-wave components on a filled two-dimensional aperture can increase the total system cost significantly. Combining everything into a single system and performing calibration can also become two very challenging tasks. Large power dissipation on a two-dimensional aperture can lead to heat concerns. An example of electronically scanning phased array can be seen in Fig. 1.2. While electronic steering mitigates the long data acquisition times of mechanical motion, this comes at the expense of increased hardware complexity and significantly greater cost.

1.2.3 Computational Imaging Systems

A significant improvement on shortening the data acquisition time and reducing the number of active components can be achieved by using computational imaging. Using coded apertures, measurement modes from the scene reflections can be obtained without scanning. An example of a computational imaging modality can be seen in Fig. 1.3. The coding can be achieved by means of frequency scanning on frequency selective elements or by switching between element configurations using active hardware which changes the radiation pattern as a function of space or with a receiver binary mask. Unfortunately, these techniques are prone to the need for solving an inverse problem of a set of linear equations $y = Ax$, where y corresponds to the measurement samples, A is the sensing matrix, and x is the imaging scene. This problem can be computationally expensive and time consuming. Although the data acquisition time of computational techniques is shorter than scanning techniques, it is still not sufficiently fast for high-speed imaging due to the need to sweep over a large enough bandwidth or switching between measurement modes [33, 36, 40]. In both cases, a large filled aperture is generally required. For high-resolution imagery, the result is a bulky and expensive aperture.

1.2.4 Multiple-Input Multiple-Output Imaging Systems

A significant reduction in the total number of antenna elements and aperture area used by an imaging system can be achieved by combining different combinations of transmitters and receivers in a multiple-input multiple-output (MIMO) fashion [41, 42]. MIMO radar is used extensively in automotive systems, where multiple transmitters transmit orthogonal signals and synthesize virtual arrays with the receive array. The same idea has been applied to the problem of near-field security screening [43, 44] with very good imaging results. The limitations of these systems are related with the use of the additional transmitters, which increases the system complexity and power consumption. Additionally, these systems can still require a large number of active components, although they do not traditionally use phase shifters. An example of a MIMO imaging modality can be seen in Fig. 1.4 where the red color represents the transmit array and the blue color represents the

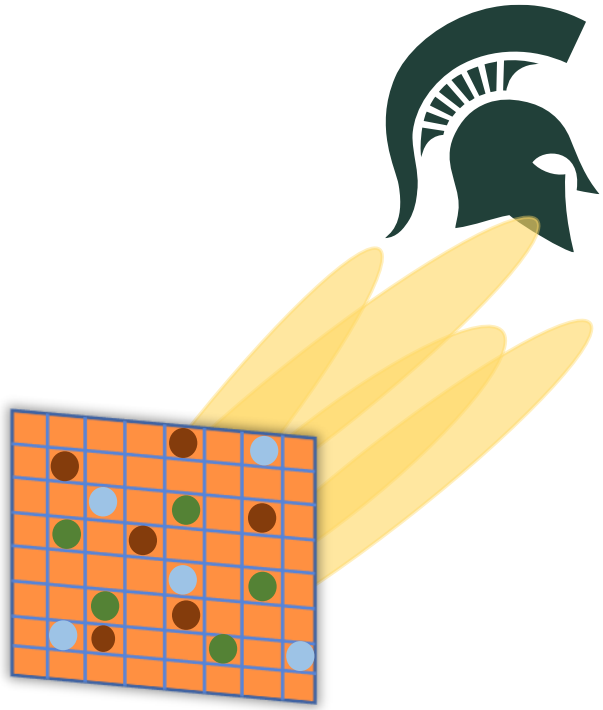

Figure 1.3: Computational imaging can reduce the measurements using coding on the measurement surface. This can be achieved by means of frequency scanning on frequency selective resonators or by switching between element configurations using active hardware. Image [1] © 2021 IEEE.

receive array.

1.2.5 Interferometric Imaging Systems

Interferometry was first developed in radio astronomy where large antenna arrays were used to produce visual mappings of stars and stellar objects without the need for a fully-populated aperture [45, 46]. Interferometric antenna arrays are sparse, with significantly less elements than traditional filled aperture arrays. Their operation is similar to an optical camera but the image reconstruction requires cross-correlations between receiver pairs.

Interferometric image formation takes advantage of the pairwise information between every two antenna elements in an antenna array. Unlike a traditional antenna array with N antenna

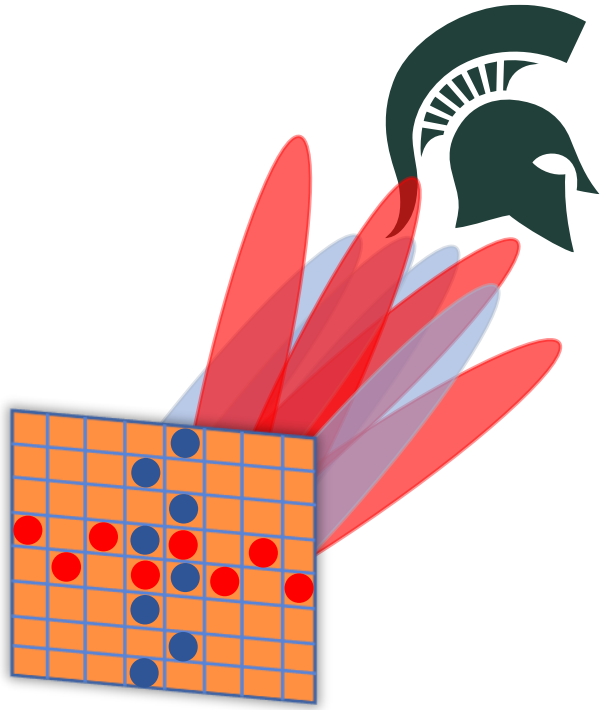

Figure 1.4: MIMO imaging can reduce the total number of antennas and aperture area used by traditional array systems by utilizing the concept of a virtual aperture with different transmit and receive combinations. Red color represents the transmit array of they system and blue color represents the receive array. The empty squares represent the antenna elements that are not used compared with a fully-populated aperture.

elements that usually has N measurement modes, an interferometric antenna array can synthesize up to $\binom{N}{2} = \frac{N(N-1)}{2}$ measurement modes by comparing the pairwise information between all the antenna elements, which leads to improved image formation. One other significant benefit of interferometric antenna arrays, compared to electronically-scanned phased arrays, is that while all antenna elements in phased arrays capture information associated with a specific point in space at every time instance, in interferometric antenna arrays every antenna element captures information associated with the entire scene simultaneously, which makes interferometric image formation faster, similar to a camera with a global shutter.

The main challenge of interferometric imaging systems is that in order for the interferomet-

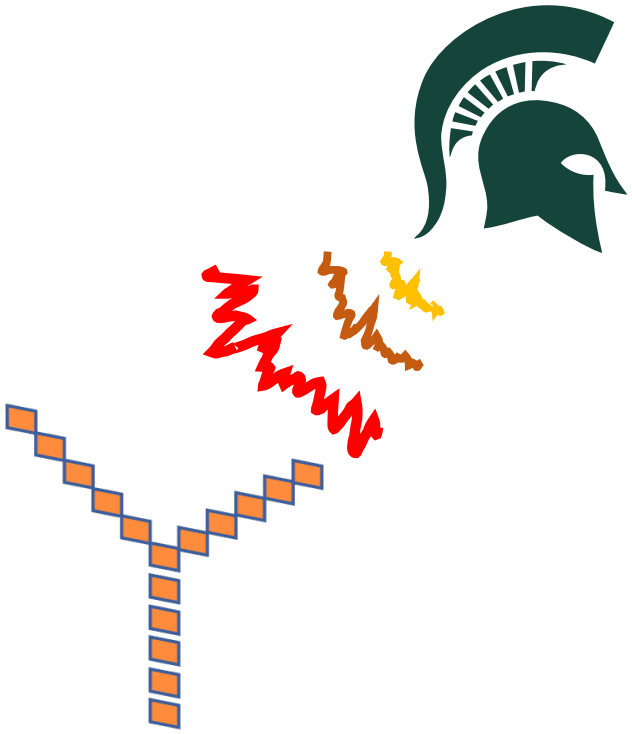

Figure 1.5: Interferometric imaging systems capture spatiotemporally incoherent signals that are emitted from the scene. Interferometric antenna arrays are sparse and reconstruct the scene intensity by performing correlation between antenna pairs.

ric image formation to succeed, they require spatio-temporally incoherent signals, according to the Van Cittert-Zernike requirements [46–48] and therefore interferometric imaging systems have been traditionally passive. However, thermal radiation has extremely low power at millimeter-wave and therefore passive interferometric imaging systems need to employ very high sensitivity receivers which require very high amplification, wide bandwidth, and long integration time [49–51]. This increases the total system cost of an interferometric imager significantly. An example of an interferometric imaging modality can be seen in Fig. 1.5, where a sparse array is capturing random thermal signals from the scene of interest.

1.3 Research Problem and Significance

The work presented in this dissertation attempts to combat the inefficiencies found in millimeter-wave imaging systems by combining the benefits of active and passive millimeter-wave imaging systems in a newly developed approach called active incoherent millimeter-wave imaging. Passive millimeter-wave imaging systems combine staring operation with sparse antenna arrays. Active systems operate with a high signal-to-noise ratio (SNR), and therefore do not need high sensitivity receivers. Active incoherent millimeter-wave imaging utilizes transmission of incoherent signals, in order to mimic the spatio-temporal incoherence properties of thermal radiation and use fast passive image reconstruction with sparse antenna arrays.

Active incoherent millimeter-wave imaging can achieve high-speed millimeter-wave imagery which can revolutionize imaging applications, such as airport security screening, an imaging application which is currently non real-time and therefore can cause significant time delays in airports along with a stressful experience for the flight passengers. Additionally, another benefit of incoherent imaging techniques is that transmitters and receivers do not need to be synchronized, which makes the imaging modality using third party communications signals a very tempting application.

Another application that can benefit from this work is rapid millimeter-wave imaging for fast-moving production belt lines. As of 2022, the world is experiencing a supply chain crisis, where production cannot keep up with demand. Millimeter-waves can easily pass through the cardboard boxes in factories and packaging facilities and give information about the contents of a shipment. This way, production does not need to be stopped for someone to open the box and check if any of the appropriate items is missing. Depth information is needed for this particular millimeter-wave imaging scenario, and three-dimensional imagery will be investigated at chapter 6.

1.4 Dissertation Organization

In this chapter I introduce the research problem, the background, and the significance of this work. In chapter 2 I introduce the theory behind interferometric imaging and active incoherent millimeter-wave imaging. In chapter 3, the problem of designing an incoherent transmitter in both space and

time is discussed along with some simulated and experimental image reconstructions. In chapter 4, I focus on system design of active incoherent imaging arrays and I discuss a calibration process that does not require any prior information regarding the imaging scene. A high speed digital array millimeter-wave imager is shown, focusing on both hardware and software. In chapter 5, I discuss the scenario of using incoherent stray reflections from communications transmitters in order to create two-dimensional microwave and millimeter-wave imagery. In chapter 6, I extend my incoherent imaging work to three-dimensional imaging and in the chapter 7, I conclude with summarizing the contributions presented in this dissertation and discuss directions for future research.

CHAPTER 2

MICROWAVE AND MILLIMETER-WAVE IMAGING USING INCOHERENT SIGNALS

2.1 Interferometric Imaging Fundamentals

A two-dimensional image, which is a two-dimensional signal, can be represented by the superposition of an infinite series of spatial sinusoidally-varying signals of different spatial frequencies and orientations. This can be viewed as the spatial equivalent of a voltage pulse being represented by an infinite set of complex exponential functions. Imagers that operate on the spatial frequency domain can measure information by capturing the electromagnetic information associated with a specific set of spatial frequencies. In an interferometric antenna array, each antenna pair corresponds to a specific spatial frequency which is dictated by the spacing and orientation of the baseline, and by correlating the received signals between the antennas in a pair, a sample of this spatial frequency information is obtained, as shown in Fig. 2.1.

For a pair of antennas in an interferometric antenna array observing a radiating point source as shown in Fig. 2.2, the received signals at the two antennas can be given by [3, 29]

$$V_1(t) = \cos(2\pi f t) + n_1(t) \tag{2.1}$$

$$V_2(t) = \cos[2\pi f(t - \tau_g)] + n_2(t) \tag{2.2}$$

where f represents the carrier frequency, θ is the residing angle of the point source relative to the baseline, $\tau_g = \frac{D}{c}\sin\theta$ is the geometric time delay, which is the difference in time the wavefront faces in reaching the two elements seperated by the baseline length D, c is the wavefront propagation speed, and $n_1(t)$ and $n_2(t)$ respresent the noise in the received signals 1 and 2, respectively. Correlation is performed between the two voltages, which in this dissertation refers to multiplication and integration. Because the signal from the point source is statistically independent from the noise on each receiver, and the noise in both receivers is uncorrelated with one another, both $n_1(t)$ and $n_2(t)$ will average to zero as integration time increases; this process can take place both

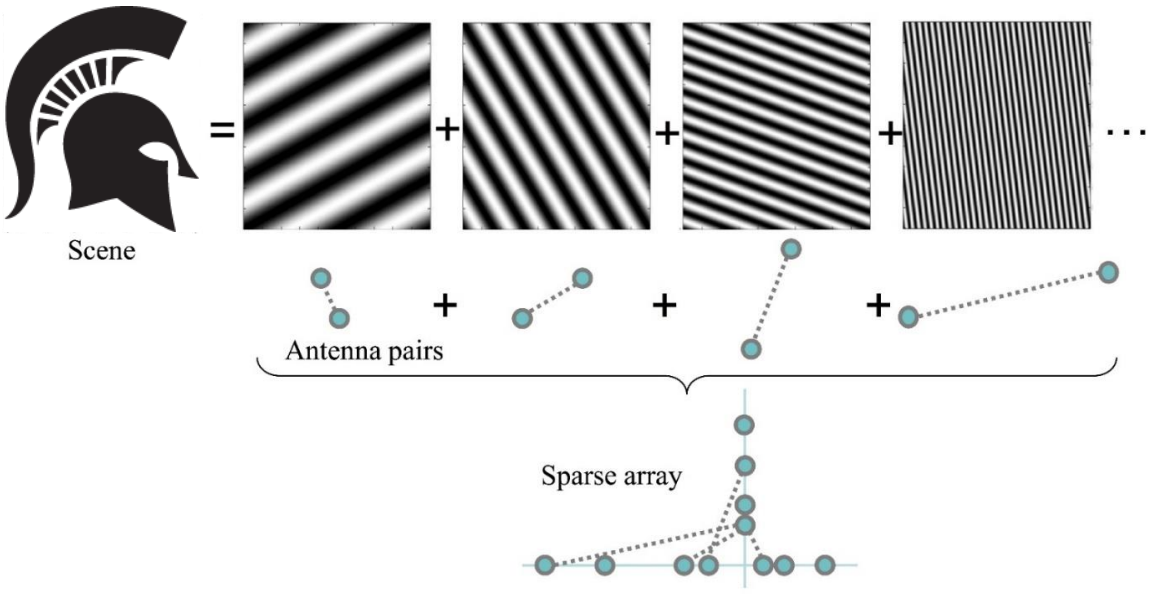

Figure 2.1: Two-dimensional images can be represented by a superposition of sinusoidally-varying signals of different spatial frequencies and orientations. An interferometric antenna array can use its multiple antenna pairs to capture those sinusoidally-varying signals at different spatial frequencies [2].

digitally but also in the analog domain with means of filtering. The response of the correlation interferometer at its output at can be written as

$$r(\theta) = \langle V_1 V_2 \rangle = \langle \cos(2\pi f t) \cos[2\pi f (t - \tau_g)] \rangle \tag{2.3}$$

where the angle brackets represent time-averaging. The integration will cut off the higher frequency terms, resulting in

$$r(\theta) = \frac{1}{2} \cos\left(\frac{2\pi}{\lambda} D \sin\theta\right) \tag{2.4}$$

where $\lambda = c/f$ is the free-space wavelength. The output of the correlation interferometer is an oscillating response relative to $\sin\theta$. The result is a spatial pattern that includes a number of grating lobes, depending on the electrical length of the baseline, which defines a specific spatial frequency whose units are cycles per radian. The information represented by (2.4) is thus the scene information in a single spatial frequency. This behavior can become more clear by observing the fringe response of the correlation interferometer in Fig. 2.3. The grating lobe structure is essentially a filter in the spatial frequency domain.

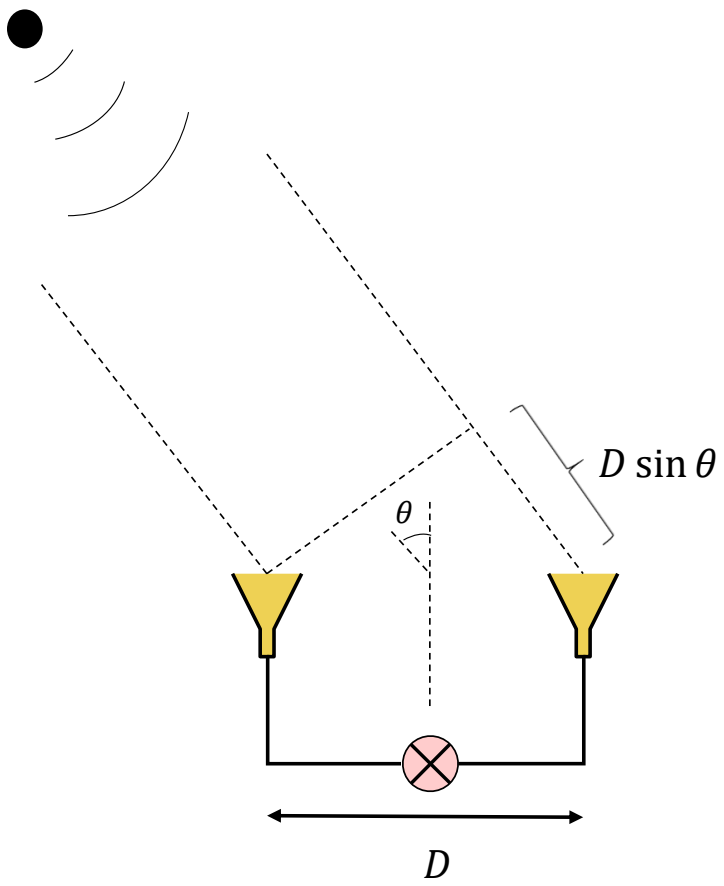

Figure 2.2: Correlation interferometer, composed of two widely separated antennas, observing the signal emanating from a point source. Image [3] © 2018 IEEE.

2.1.1 Visibility Sampling

A correlation interferometer is observing the signals emitted from a scene in space, whose spatial intensity is $I(\gamma)$, and $\gamma = \sin\theta$, $u = D_\lambda = D/\lambda$ is the spatial frequency corresponding to the baseline D, which is then normalized to the wavelength λ and

$$\mathcal{V}(u) = \int_{-\infty}^{\infty} I(\gamma) K(\gamma) e^{j2\pi u\gamma} d\gamma \tag{2.5}$$

is the complex scene visibility, which is the spatial Fourier transform of the scene intensity. $K(\gamma)$ is the system beam pattern which includes the spatial domain effects of the antenna radiation pattern and receiver bandwidth [29]. Under the assumption that the signals emanating from the scene are spatially and temporally incoherent, which means that every spatial point has an independent

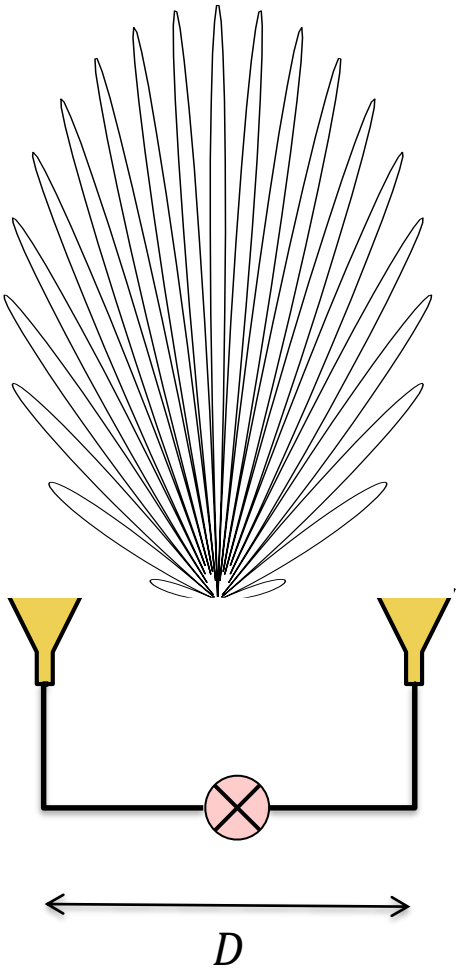

Figure 2.3: The fringe response of the correlation interferometer formed by two antenna elements separated at a large number of wavelengths. It is the grating lobe structure that serves as the spatial frequency filter. Image [3] © 2018 IEEE.

response as a function of time, and when the field of view is narrow, such that $\gamma^2 \ll 1$, and centered close to broadside, it follows from the Van Cittert-Zernike theorem [45–48] that the correlations between the antenna array elements yield samples of the complex scene visibility. These samples give rise to the sampled visibility $\mathcal{V}_s$, which is related to the reconstructed scene intensity I_r through a Fourier transform

$$I_r(\gamma) = \int_{-\infty}^{\infty} \mathcal{V}_s\,(u)\, e^{-j2\pi u\gamma} d\gamma. \tag{2.6}$$

The Van Cittert-Zernike theorem suggests that the mutual coherence function of a distant, incoherent source is equal to its complex visibility, and therefore the above equation holds. As a result, with a sufficient number of antenna elements and baselines, a large number of visibility samples can be acquired, and the scene intensity information, multiplied by the system beam pattern, can be acquired.

In some cases, such as in the radio astronomy antenna arrays, the visibility sampling can take place continuously as a function of the electrical baseline, as indicated by the integration in (2.5), by capturing the signals emitted by a celestial object as the earth rotates. The baseline is changing as the earth is rotating which enables the synthesis of different baselines. However, this cannot take place in many applications that require real-time operation, so an antenna array with a fixed set of antennas is the preferred choice, which can perform visibility sampling in real-time using a certain set of baselines. The spatial frequency function that summarizes which visibility samples are retained is usually referred as the sampling function

$$S(u) = \sum_{n}^{N} \delta(u - u_n) \tag{2.7}$$

where N is the number of baselines that are present in the antenna array. The reconstructed scene intensity can be found with

$$I_r(\gamma) = \sum_{n}^{N} \mathcal{V}_s(u_n) e^{-j2\pi u_n \gamma}. \tag{2.8}$$

The above relationships can be directly extended for a two-dimensional scene intensity and visibility by using means of a two-dimensional antenna array. The two-dimensional complex scene visibility can be written as

$$\mathcal{V}(u, v) = \iint_{-\infty}^{\infty} I(\alpha, \beta) K(\alpha, \beta) e^{j2\pi(u\alpha + v\beta)} d\alpha d\beta \tag{2.9}$$

where $\alpha = \sin\theta\cos\phi$ and $\beta = \sin\theta\sin\phi$ are the direction cosines relative to the u and v spatial frequency dimensions. The angles θ and ϕ can be seen in Fig. 2.4 in relation to a two-dimensional antenna array. The two-dimensional reconstructed scene intensity I_r can then be computed as

$$I_r(\alpha, \beta) = \sum_{n}^{N} \sum_{m}^{M} \mathcal{V}_s(u_n, v_m) e^{-j2\pi(u_n\alpha + v_m\beta)}. \tag{2.10}$$

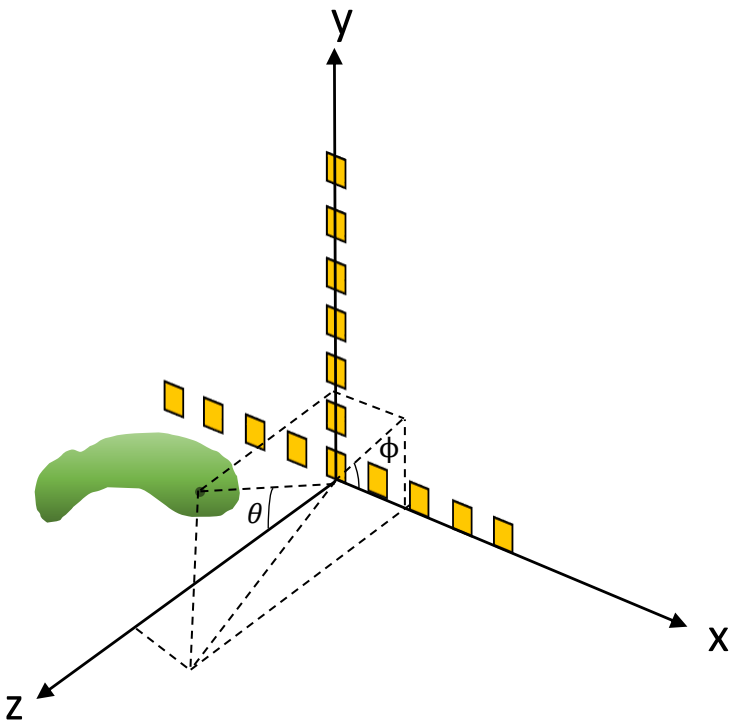

Figure 2.4: Two-dimensional array of antennas observing the signals from a distributed spatial source. Image [3] © 2018 IEEE.

The interferometric image reconstruction algorithm, which takes place in the spatial frequency domain, can be seen in Fig. 2.5. The sampling function is given by all the combinations of the antenna pairs in the antenna array, which then multiplies the scene visibility and dictates the spatial frequency content which is retained. The reconstructed scene intensity I_r is then acquired through an inverse fast Fourier transform (IFFT).

2.1.2 Spatial Domain Interpretation

Although interferometric image reconstruction takes place in the spatial frequency domain through visibility sampling, it can be very helpful to consider the interferometric image reconstruction in the spatial domain as well. Both complex visibilities and sampling functions reside in the spatial frequency domain and the last step in Fig. 2.5 reconstructs the scene in the spatial domain through means of Fourier processing. The response of the imaging array in the spatial domain, or the

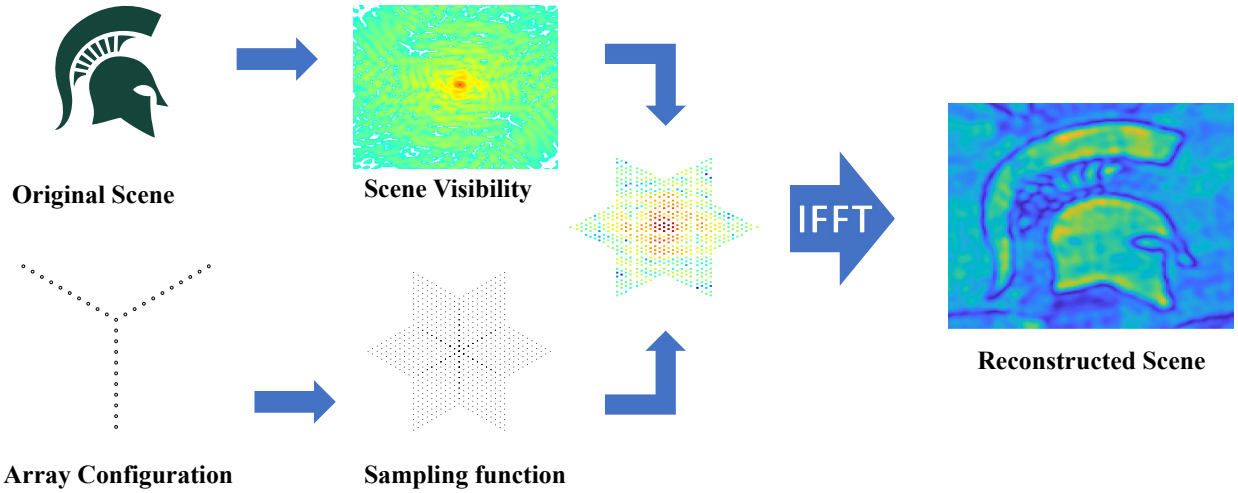

Figure 2.5: Image Reconstruction Algorithm: The image is reconstructed by taking the Fourier transform of the sampled scene visibility $\mathcal{V}$, the latter being the scene information in the spatial-frequency domain. The sampled visibility $\mathcal{V}_s$ is the product of the scene visibility $\mathcal{V}$ and the sampling function S, which is the set of spatial frequencies measured by the array. Image [4] © 2020 IEEE.

imaging system's impulse response, is the point-spread function (PSF) of the array, where

$$\mathrm{PSF}(\alpha, \beta) = \mathrm{IFT}\{S(u, v)\}. \tag{2.11}$$

The PSF is usually a synthesized beam in the spatial domain, and is a result of the different baselines included in the array. Because inteferometric imaging is incoherent imaging and reconstructs image intensities, the PSF is usually substituted by $|\mathrm{PSF}|^2$. The reconstructed scene intensity I_r can be written as a convolution between the spatial scene intensity I and the PSF:

$$I_r(\alpha, \beta) = |\mathrm{PSF}(\alpha, \beta)|^2 * I(\alpha, \beta) \tag{2.12}$$

where $*$ indicates convolution in the spatial domain. It is clear that the reconstructed scene intensity will be distorted by the shape of the PSF. Ideally, the PSF will be a delta function, which can be written as $\mathrm{PSF}(\alpha, \beta) = \delta(\alpha, \beta)$, and therefore $I_r(\alpha, \beta) = I(\alpha, \beta)$. Unfortunately, in order for the PSF to be a delta function, an infinite amount of spatial frequency samples would be required which translates to an infinite number of antennas. In actual imaging systems the PSF is usually composed of a main beam and a number of sidelobes with different extent and magnitude.

In the spatial domain some important image reconstruction metrics can be defined. In many microwave imaging techniques, the unambiguous field of view of the system in azimuth and elevation planes is defined by the minimum antenna separation in the antenna grid. In interferometry, it is the sampling function that operates as a virtual array and dictates the unambiguous field of view. The half-angle unambiguous field of view of an interferometric imager with grid spacings d_x and d_y across the horizontal and vertical array axes can be expressed for the two direction cosines α and β as

$$FOV_{\frac{\alpha}{2},\frac{\beta}{2}} = \frac{\lambda}{2 \cdot d_{x,y}} \quad . \tag{2.13}$$

The resolution of the imager in the azimuth and elevation planes can be approximated by the half-power beamwidth θ_{HPBW} of the sinc-squared response from the largest baselines D_x and D_y in the horizontal and vertical axes of the array x and y, respectively [52]. This can be defined as

$$\mathrm{sinc}^2(\frac{\theta_{HPBWD_{x,y}}}{2\lambda}) = \frac{1}{2} \tag{2.14}$$

$$\frac{\theta_{HPBWD_{x,y}}}{2\lambda} \approx 0.44 \tag{2.15}$$

and the θ_{HPBW} along α and β can be found through

$$\Delta\theta_{\alpha,\beta} \approx \theta^{(\alpha,\beta)}_{HPBW} \approx 0.89\frac{\lambda}{D_{x,y}} \quad . \tag{2.16}$$

2.1.3 Fourier Domain Relationships

While interferometric imaging operates predominantly in the spatial frequency domain, some metrics can be intuitively defined in the spatial domain. It is instructive to consider the relationships between the quantities in the spatial and spatial frequency domains. A flowchart that describes the Fourier transform relationship between the spatial and spatial frequency image reconstruction process can be seen in Fig. 2.6 [53]. Similarly to the impulse and frequency response of a system,

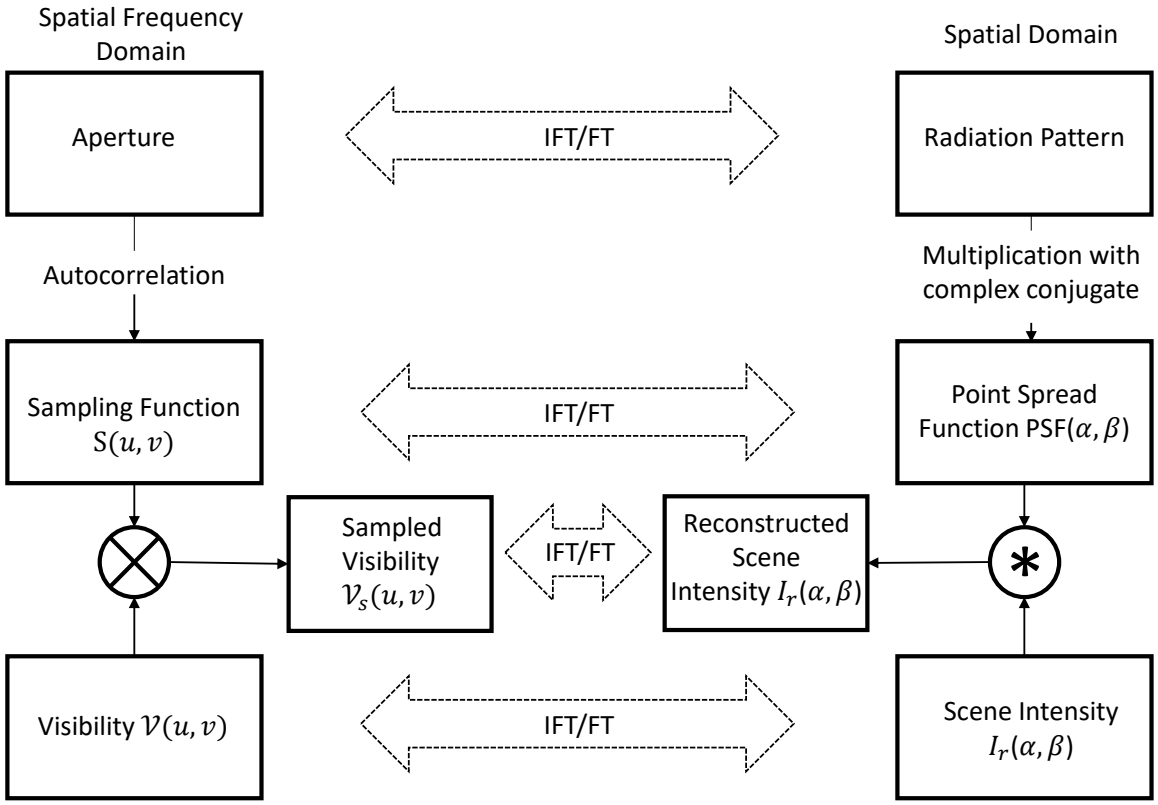

Figure 2.6: Flowchart that describes the Fourier transform relationships between the image reconstruction in the spatial and spatial frequency domains. The Fourier transform relationship is valid in every step of the process.

the PSF and the sampling function $S(u,v)$ are connected through a Fourier transform relationship. The sampling function is obtained through all the pairwise combinations in an array, which can be interpreted as an autocorrelation, and the PSF can be found through the multiplication of the array radiation pattern with its complex conjugate. The sampling function reconstructs the sampled scene visibility $\mathcal{V}_s(u,v)$ through a multiplication while the reconstructed scene intensity $I_r(\alpha,\beta)$ is found through a convolution of the PSF with the actual scene intensity $I(\alpha,\beta)$. Both sampled visibility $\mathcal{V}_s(u,v)$ and reconstructed scene intensity $I_r(\alpha,\beta)$ are connected through a Fourier transform pair.

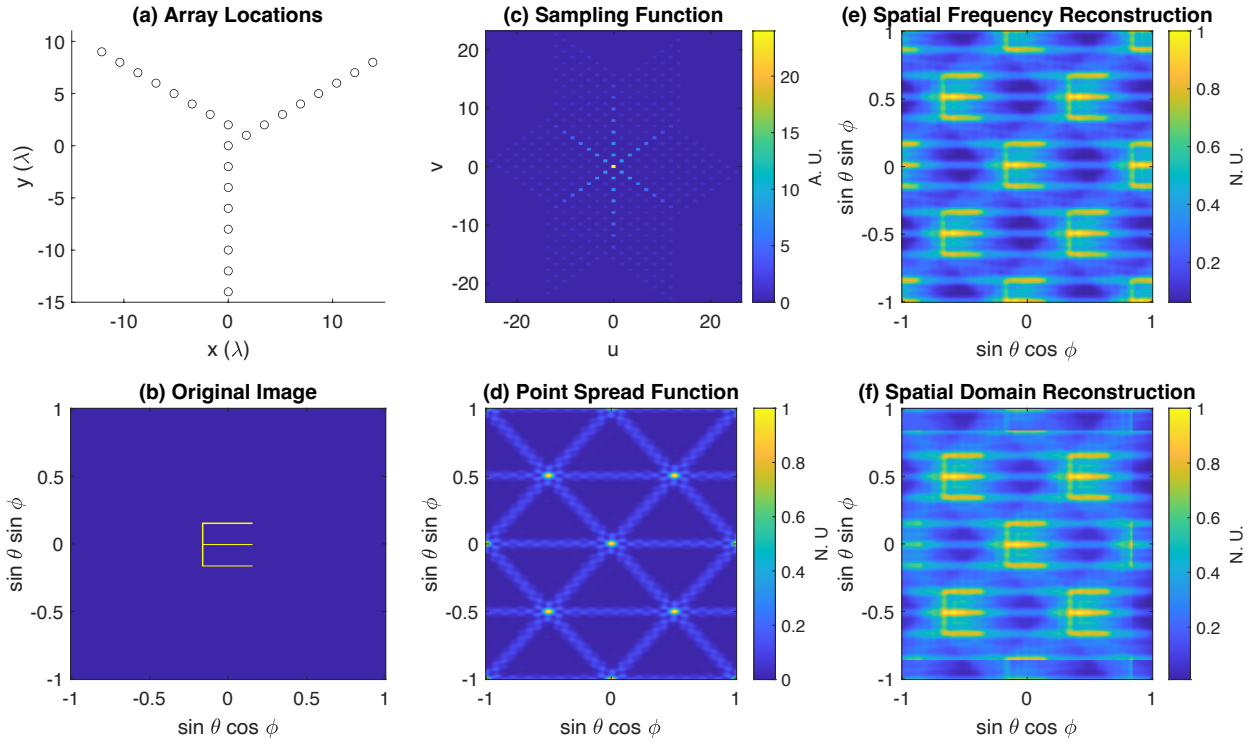

Figure 2.7: (a) Antenna element locations of a 24-element asymmetric Y-shaped array as a function of wavelength. (b) Original image with the letter "E" in the center of it used as the simulated scene. (c) Sampling function and (d) PSF of the antenna array. (e) Spatial frequency reconstruction using multiplication of the Fourier transform of the original scene with the sampling function. (f) Spatial domain reconstruction using convolution of the original image with the PSF.

Simulated results that demonstrate the spatial frequency and spatial domain equivalence can be found in Fig. 2.7. The locations of an asymmetric Y-array in wavelengths are shown in Fig. 2.7(a). The array is composed of three linear arms that share an angular separation of 120° between every two of them. The design of the Y-array is chosen because it offers a dense spatial frequency coverage, and plenty of redundancy which can be helpful for calibration purposes, as we will see in chapter 4. In Fig. 2.7(b) the spatial scene with the letter "E" in the center can be seen. The sampling function of the antenna array can be seen in Fig. 2.7(c) which is the autocorrelation of the antenna array element locations. The array PSF can be seen in Fig. 2.7(d). The spatial frequency domain reconstruction takes place by multiplying the Fourier transform of the original image with the sampling function and can be seen in Fig. 2.7(e). The spatial domain reconstruction, which

is achieved through spatial convolution of the PSF with the original spatial image, can be seen in Fig. 2.7(f). Both spatial and spatial frequency domain approaches give almost identical image reconstructions, with aliasing present due to element spacing larger than $\frac{\lambda}{2}$. The MATLAB script that was used to generate the plots in Fig. 2.7 can be found in Appendix A.

2.2 Incoherence of Signals and the Van Cittert-Zernike theorem

A requirement for the interferometric image reconstruction to succeed is the Van Cittert-Zernike theorem, which dictates that the signals emanating from the scene must be spatio-temporally incoherent. The thermal signals emitted by humans and celestial objects satisfy the incoherence requirement, however thermal radiation has exceedingly low power at microwave and millimeter-wave frequencies. This means that passive interferometric imaging systems need to employ very high sensitivity receivers. This translates to very high gain amplifiers with very small noise figure, wide bandwidth, and long integration times, leading to prohibitively expensive microwave and millimeter-wave hardware and slow image formation.

The importance of the Van Cittert-Zernike theorem requirements can become more clear by considering an incoherent radiating source as shown in Fig. 2.8. The signals emanating from the source are captured at the locations of the antenna elements 1 and 2. The signals received by the antennas are cross-correlated which is a measure of the spatial coherence of a signal. The analysis in this section is very similar to the one given by Thompson, Moran and Swenson in [45]. The mutual coherence function Γ_{ij} for an electric field E measured at two different locations i and j, can be written as

$$\Gamma_{ij}(u,v,\tau) = \lim_{T\to\infty} \frac{1}{2T} \int_{-T}^{T} E_i(t) E_j^*(t-\tau)\, dt \tag{2.17}$$

where u and v are the electrical coordinates of the spacing between the two measurement points, $u = \frac{(x_i - x_j)f}{c}$ and $v = \frac{(y_i - y_j)f}{c}$, and (x_i, y_i), (x_j, y_j) are the spatial locations of antenna elements i and j.

If the distance between the radiating source and the antenna elements is significantly larger than the baseline between them, then it can be deduced that the direction cosines α, β (on the azimuth

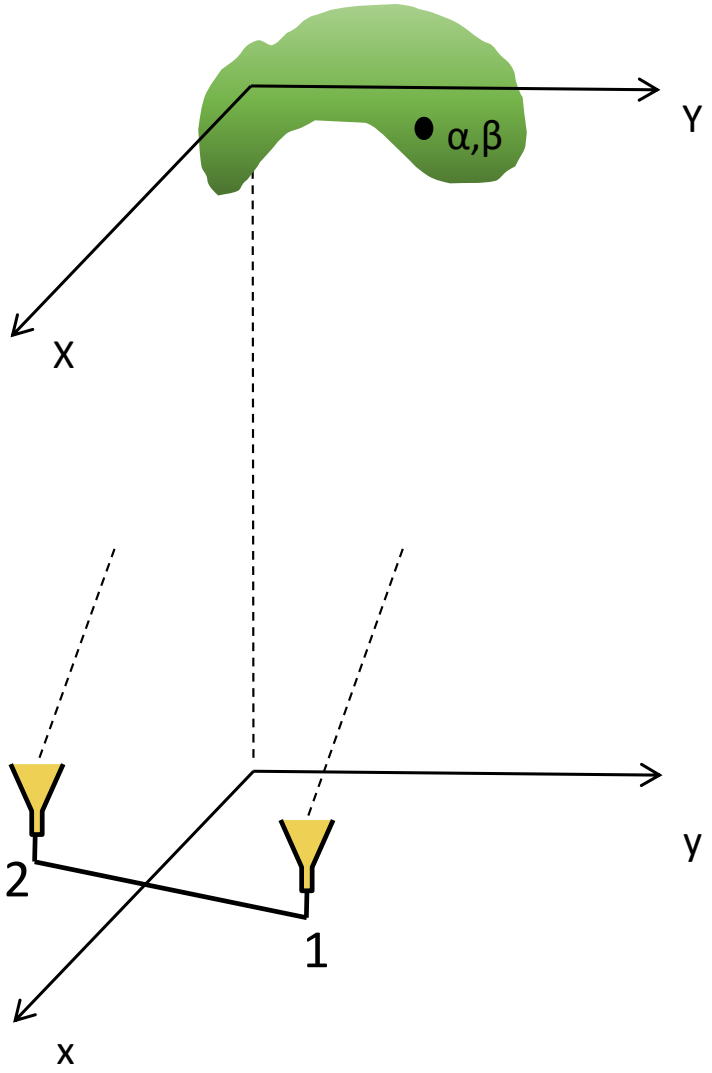

Figure 2.8: Two antenna elements forming a baseline observing the signals emanating from a distributed source. Image [5] © 2019 IEEE.

and elevation planes respectively) that an antenna observes the radiating point source from, are approximately the same for both the antenna elements 1 and 2 in Fig. 2.8. The amplitude of the electric fields at both elements can be assumed to be approximately the same, because the source resides close to broadside and both antennas reside on the same plane, at a large distance away from the source. The phase term though will be shifted because of the slight differences in distance for both elements from the source. As a result, the electric field originating from a single point of the

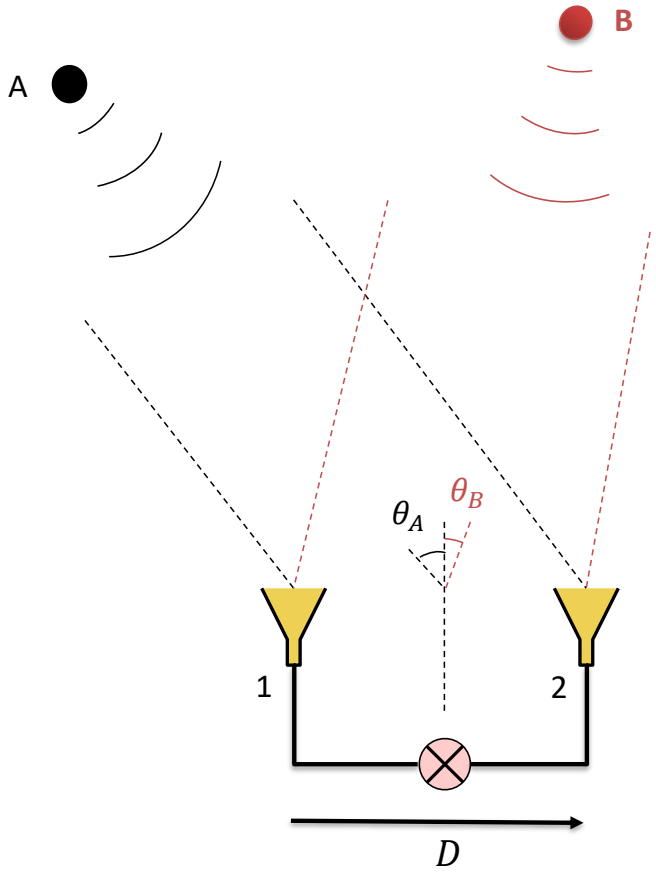

Figure 2.9: A correlation interferometer observing the signals originating from two point sources. Image [4] © 2020 IEEE.

source captured at locations 1 and 2 can be written as

$$E_1(\alpha, \beta, t) = \mathcal{E}(\alpha, \beta, t) \frac{e^{-j2\pi f(t-R_1/c))}}{R_1}$$
$$E_2(\alpha, \beta, t) = \mathcal{E}(\alpha, \beta, t) \frac{e^{-j2\pi f(t-R_2/c))}}{R_2} \tag{2.18}$$

where $\mathcal{E}(\alpha, \beta, t)$ represents the magnitude of the electric field, R_1 and R_2 are the distances of the antenna elements from the point source. In this chapter, the effects of polarization of the electric field are not considered but can be included using vector quantities and the polarization

loss factor. By performing a cross-correlation between the two electric fields quantities in (2.18), a measurement of their mutual coherence can be written as

$$\begin{aligned}&\langle E_1(\alpha,\beta,t)E_2^*(\alpha,\beta,t)\rangle = \\ &\langle \mathcal{E}(\alpha,\beta,t)\mathcal{E}^*(\alpha,\beta,t)\rangle \frac{e^{-j2\pi f((R_2-R_1)/c))}}{R_1R_2}.\end{aligned} \tag{2.19}$$

By performing an integration over all points in the distributed source, the intensity $I(\alpha,\beta)$ of the source can be written in terms of the mutual coherence of the source at the two antenna elements' locations as

$$\Gamma_{12}(u,v,0) = \int_{source} \frac{I(\alpha,\beta)e^{-j2\pi f((R_2-R_1)/c)}}{R_1R_2} ds \tag{2.20}$$

where $(R_2 - R_1)$ is the difference in the distances from a point source to locations 1 (x_1, y_1) and 2 (x_2, y_2). The time difference τ is equal to zero, because the two electric fields are captured at the same time. For the magnitude terms we can again approximate $R_1 \approx R_2 \approx R$ and $ds = R^2 d\alpha d\beta$. As a result, (3.6) can be turned into

$$\Gamma_{12}(u,v,0) = \int_{source} I(\alpha,\beta)e^{-j2\pi(u\alpha+v\beta)} d\alpha d\beta. \tag{2.21}$$

It is evident that that the mutual coherence is the two-dimensional Fourier transform of the intensity of the source, which is the definition of the visibility, hence

$$\Gamma_{12}(u,v,0) = \mathcal{V}(u,v). \tag{2.22}$$

which is the most well known property of Van Cittert-Zernike theorem.

In the aforementioned analysis, the signals emanating from the spatial points in the scene have been assumed to be perfectly incoherent. As a result, after the cross-correlation process, only the common signals originating from the same point remain. Unwanted mixing terms between different spatial points in the form of $\langle E_1(\alpha_l,\beta_l,t){E_2}^*(\alpha_m,\beta_m,t)\rangle$ where l and m denote different spatial points of the scene, tend to vanish as integration time increases. If the spatial and temporal incoherence properties do not hold, and therefore the radiation emanating from different points is not incoherent, then the unwanted mixing terms do not vanish, which could make interferometric image reconstruction fail. Thermally generated electromagnetic signals show noise-like behavior

in both the spatial and temporal domain, and thus the mixing terms vanish for sufficiently long integration times. Passive systems do not suffer from these unwanted cross-product terms and this is why most inteferometric systems have been passive utilizing thermal signals.

The following example further explores what happens in the presence of multiple targets. In a correlation pair in the antenna array that observes the signals emitted by two point sources as shown in Fig. 2.9, the voltage signals on the two receivers can be given by:

$$V_1 = s_{1A} + s_{1B} + n_1 \tag{2.23}$$

$$V_2 = s_{2A} + s_{2B} + n_2 \tag{2.24}$$

where s_{iA}, s_{iB} are the signals captured by the ith antenna element due to the point sources A and B respectively, and n_i is the receiver noise at the ith element. After performing the cross-correlation between the two receiver responses, the output voltage can be written as

$$\begin{aligned} V_{out} &= \langle V_1 V_2 \rangle \\ &= \langle s_{1A} s_{2A} \rangle + \langle s_{1B} s_{2B} \rangle + \langle s_{1A} s_{2B} \rangle + \langle s_{1B} s_{2A} \rangle. \end{aligned} \tag{2.25}$$

If the spatio-temporal incoherence assumption holds, then after sufficient time-averaging, the terms $\langle s_{1A} s_{2B} \rangle$ and $\langle s_{1B} s_{2A} \rangle$ would vanish and therefore the correlation ouput can be approximated as

$$V_{out} = \langle V_1 V_2 \rangle = \langle s_{1A} s_{2A} \rangle + \langle s_{1B} s_{2B} \rangle \tag{2.26}$$

which is the desired result. This is easily satisfied in passive systems but in active systems that employ transmitters it is challenging to make the cross-product mixing terms vanish. In the following chapter, I discuss a way to simulate incoherent illuminations, and investigate incoherent transmitter design such that the unwanted terms will be mitigated.

CHAPTER 3

SPACE-TIME INCOHERENT TRANSMITTER DESIGN AND MEASUREMENTS

3.1 Transmit Signal Analysis for Incoherent Imaging

The spatio-temporal coherence of the signals emitted or reflected from the scene is essential so that the relationships between the mutual coherence, visibility, and scene intensity are valid, according to the Van-Cittert Zernike theorem [46], which was reviewed in chapter 2. And while for thermal sources this requirement is easily satisfied, because of the inherent randomness, an active system must illuminate the scene with signals that are sufficiently incoherent in space and time to ensure a proper image reconstruction. Using traditional coherent signal transmission, such as a Frequency-Modulated Continuous-Wave (FMCW) or stepped-frequency transmit signal, to illuminate the scene will give a strong coupling in the spatial domain and nearby points in the scene therefore will reflect back a very similar response. This why interferometry traditionally does not work with coherent illuminations and previous work had to rely on thermally generated electromagnetic signals. In this chapter, I explore how we can mimic the properties of thermal radiation by illuminating the scene with random noise-like signals. These signals are reflected from the spatial scene and when captured by the receiving array, should be sufficiently uncorrelated in space and time to use Fourier-based interferometric image reconstruction. The array of transmitters can thus be incoherent, requiring minimal coordination between the transmit and receive hardware.

The use of an array of noise transmitters that illuminate the scene on the far-field is investigated first. To determine the spatio-temporal properties of the transmitted signals, I consider the case of a one-dimensional scene spanning $\theta \in (-\frac{\pi}{2}, \frac{\pi}{2})$. Using an array of L noise transmitters, the response of the lth transmitter can be modeled as

$$x_l(t) = a_l(t)e^{j[2\pi f_c t + p_l(t)]} \tag{3.1}$$

where $a_l(t), p_l(t)$ are the random amplitudes and phases of the lth transmitter which follow a

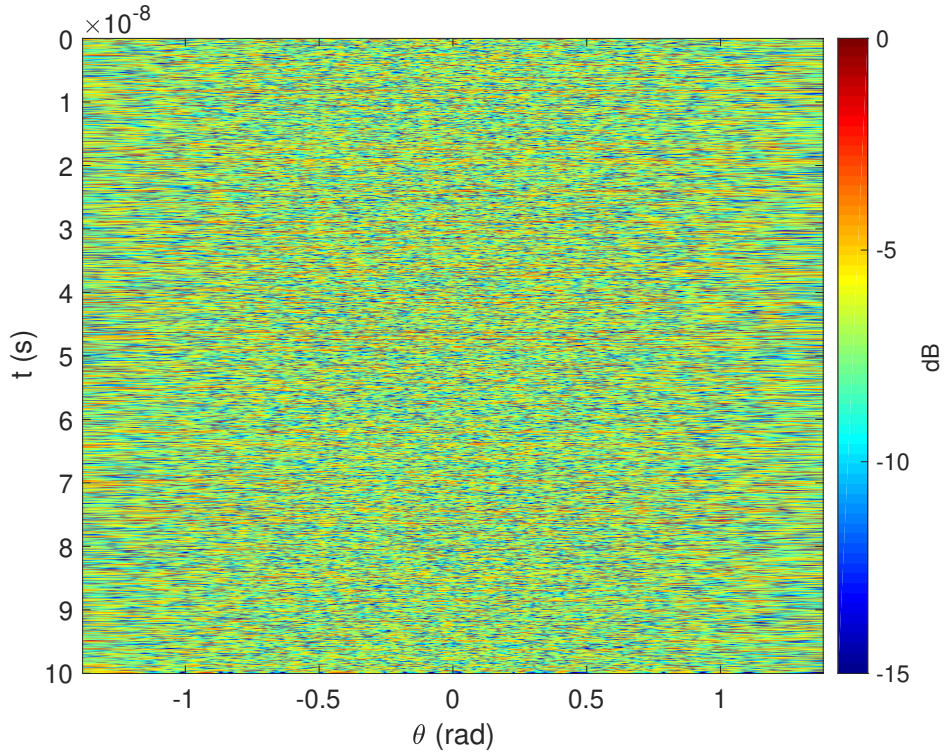

Figure 3.1: Normalized transmitted noise signal in the spatial domain (horizontal axis) and the temporal domain (vertical axis). The uncorrelated nature of the signal in both space and time can be seen, however the autocorrelation of the signal in Fig. 3.2 provides a more concrete metric for spatio-temporal incoherence. Image [3] © 2021 IEEE.

Gaussian distribution. In a single dimension and at a much larger distance than the array maximum dimension, the spatio-temporal radiation from the incoherent transmit L-element array for narrow bandwidth Δf can be approximated as

$$A(\theta, t) = \sum_{l=1}^{L} x_l(t) \int_{f_c - \frac{1}{2}\Delta f}^{f_c + \frac{1}{2}\Delta f} e^{-j\frac{2\pi f}{c} d_l \sin\theta} df \tag{3.2}$$

where d_l represents the location of the lth transmitter in the array.

The spatio-temporal scene is proportional to the reflected radiation from the scene $s_r(\theta)$, and can be calculated from

$$s_{st}(\theta, t) = A(\theta, t) s_r(\theta) \tag{3.3}$$

The received radiation of the lth element of the array can be expressed as a sum of the spatio-

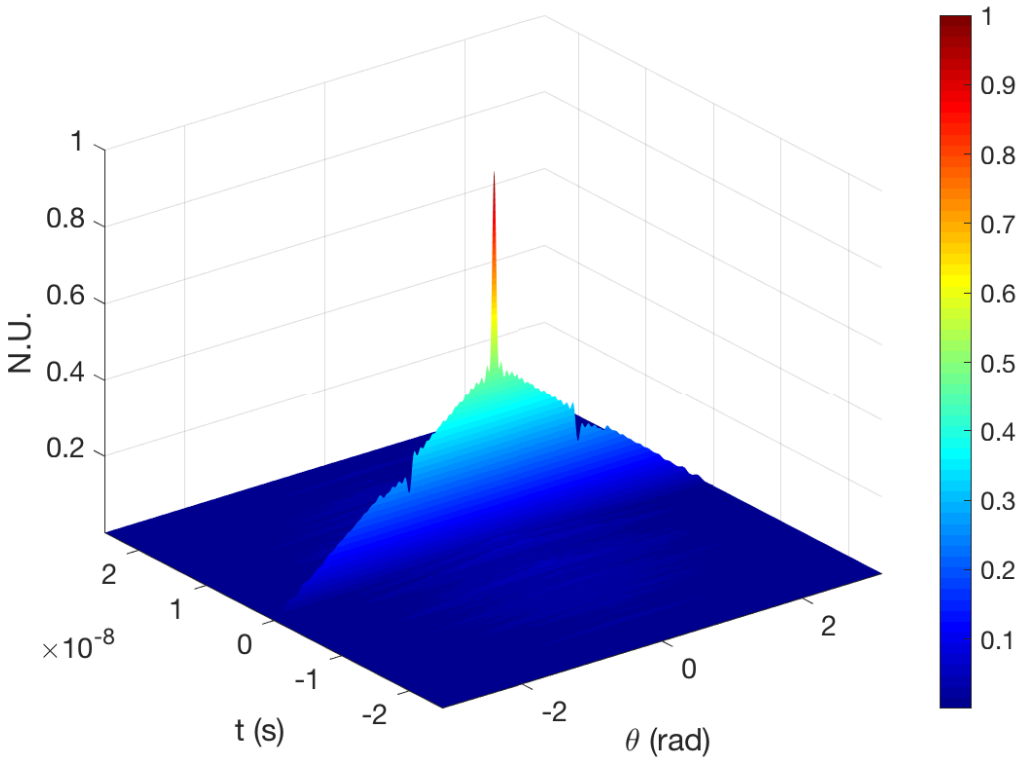

Figure 3.2: The two-dimensional autocorrelation of the spatio-temporal transmit pattern displays a strong response at (0,0), with lower responses elsewhere, demonstrating that the signal is sufficiently uncorrelated in both time and space, thereby indicating the feasibility of its use for active spatial frequency sampling. The amplitude is normalized, hence the vertical axis is in normalized units (N.U.). Image [3] © 2021 IEEE.

temporal scene over angle by

$$r(l,t) = \int_{-\frac{\pi}{2}}^{\frac{\pi}{2}} s_{st}(\theta,t) e^{-jkd_l \sin\theta} d\theta. \tag{3.4}$$

Fig. 3.1 shows the far-field transmitted signals from a 31-element linear antenna array with 1 λ spacing. From Fig. 3.1, the radiation in both space (horizontal axis) and time (vertical axis) appears to be noise-like, however to analyze this property more concretely, the autocorrelation of the transmitted waveform is shown in Fig. 3.2. The autocorrelation displays a strong peak at (0,0), with much lower amplitudes elsewhere, indicating that the transmitted signal is sufficiently uncorrelated in the spatio-temporal domain. The slightly raised area in the spatial domain (along the θ-axis) indicates that the signal is more correlated in the spatial domain than the temporal

domain. This means that there is particular room for investigating how coherence propagates in the spatial domain, which will take place in the next sections of this chapter. Such a problem has not been investigated thoroughly before in the microwave and millimeter-wave imaging literature.

3.2 Spatial Coherence of Incoherent Transmitters

One important advantage of incoherent imaging techniques [54] compared to coherent approaches is that the exact knowledge of the transmitter space-time modulation is not needed. The significance of this becomes apparent when considering the necessary knowledge and synchronization needed to implement other sparse array imaging techniques such as multiple-input multiple-output (MIMO), where the individual code on each transmitter must be known and appropriately coordinated among all receivers in the array. In incoherent imaging, no synchronization is necessary between transmitters and receivers. In interferometry, the received signals are cross-correlated, and image formation is then obtained directly using an inverse Fourier transform (IFT).

In this section, I explore and experimentally demonstrate a technique for measuring the spatial coherence in the image plane of signals emitted by a set of incoherent transmitters. Currently, no metrics exist for characterizing the image plane coherence in an active interferometric imaging system. This work provides a fundamental first step towards a comprehensive design approach for AIM transmitter arrays.

The superposition of two completely incoherent signals transmitted from two different points in space exhibits uniqueness across space and time. The way and the degree that two points in space can be correlated impacts the residual terms in (2.25) and as a result the image reconstruction quality, because these terms should not be present. The spatial coherence from the superposition of the two transmitted signals, such as shown in Fig. 3.3, can be analyzed by considering the signals to be emitted by two point sources. The two transmitters generate two incoherent spherical waves. Any point along the same phase wavefront will be perfectly coherent with itself in this model. There will be two points that can have identical and coherent responses because two circles with different centers in a two-dimensional plane can have up to two intersecting points. Due to

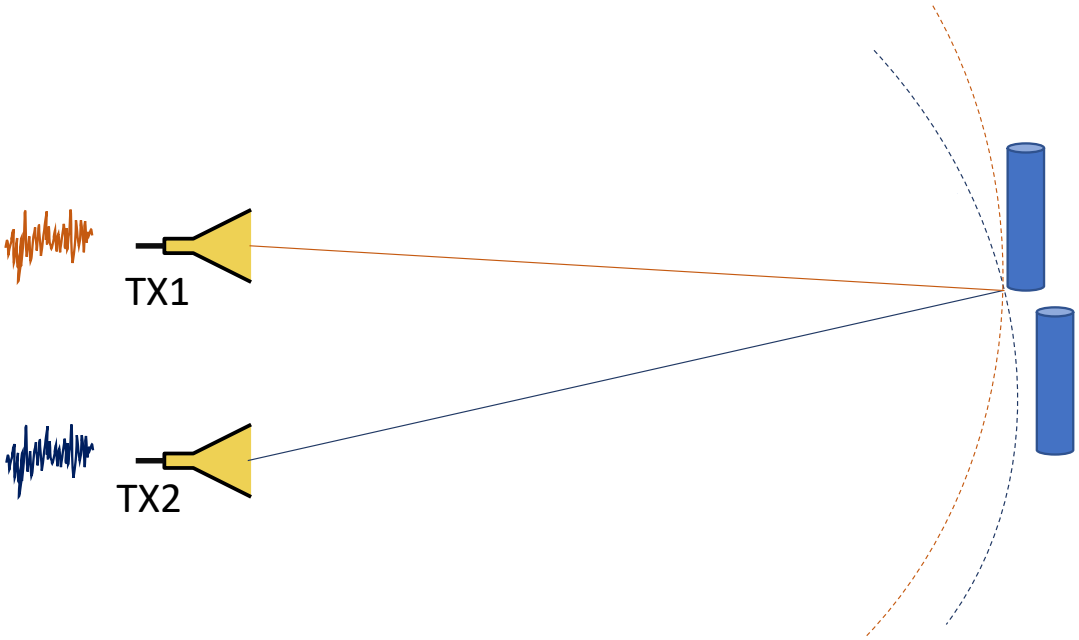

Figure 3.3: Two incoherent sources illuminating two targets. Image [6] © 2021 IEEE.

the symmetry of our case it will be one intersecting point in the front and one in the back of the array. Using directive antennas, the ambiguous "image" point located behind the antennas can be ignored. Therefore, the intersection of the waves from separate equal amplitude transmitters represents a unique point, as shown in Fig. 3.3.

The argument extends directly to three-dimensional spaces, where three spherical wavefronts emitted by the three sources intersect. With the same front-back symmetry and directive antennas, an unambiguous measurement is thus obtained in three-dimensions using three emitters. A simple solution to the problem when all three transmitters are coplanar is to conveniently choose the coordinate frame such as $(x_1, y_1, 0)$=$(0, 0, 0)$, $(x_2, y_2, 0)$=$(\alpha, 0, 0)$ and $(x_3, y_3, 0)$=$(\beta, \gamma, 0)$, where α, β, γ are variables that describe the three transmitter locations $(x_1, y_1, 0)$, $(x_2, y_2, 0)$, and $(x_3, y_3, 0)$. The equations for the three spheres are

$$(x - x_i)^2 + (y - y_i)^2 + (z - z_i)^2 = r_i^2 \tag{3.5}$$

and their intersecting points (when they exist) can be found through

$$(x, y, z)^T = \Big(\frac{r_1^2 - r_2^2 + \alpha^2}{2\alpha}, \\ \frac{r_1^2 - r_3^2 + \beta^2 + \gamma^2 - 2\beta x}{2\gamma}, \pm\sqrt{r_1^2 - x^2 - y^2}\Big).$$

The points that will have exactly the same superposition will have the same x and y coordinates, but opposite z coordinate. This is not unexpected, since the problem has symmetry about the $x - y$ plane. These two points will have exactly the same response if the antennas were isotropic, however we can assume that directional antennas are used so the solution of the problem for $z < 0$ can be ignored [55].

The intersections of the wavefronts represent points of unique illumination, however even completely uncorrelated transmit signals will display some amount of correlation at the image plane, depending on the number of transmitters used in the configuration. This is because every point at the intersection contains information from all the transmitters, which is constant across the wavefronts; hence for a two-element transmitter as in Fig. 3.3, the information everywhere along the orange wavefront from TX1 is also present at the intersection. The signal at the intersection is therefore correlated with the information at every point along the wavefront by $\frac{1}{2}$, because the contributions from one out of the two transmitters will be identical for all these points. Drawing an image plane extending vertically across the scene, there will thus be one other point in the plane that will be correlated by 50% with the signal at the intersection. The direct extension of this concept suggests that by using N trasmitters, any two points in the image plane will have at most $\frac{100}{N}\%$ correlation. There is a decrease in the partial coherence, because now every point is a combination from the N transmitters' response, but in the image plane up to only one circular wavefront can be common at two points. A useful metric to quantify the similarity of the electric field E at two points 1 and 2 is the complex degree of coherence [45, 46], which we briefly visited in chapter 2 and can be found through the following formula

$$\Gamma_{12}(\tau) = \lim_{T\to\infty} \frac{1}{2T} \int_{-T}^{T} E_1(t) E_2^*(t - \tau)\, dt \tag{3.6}$$

where T is the observation time. Most of the times when measuring spatial coherence between two different spatial points we refer to their fields at exactly the same time, so we can set $\tau = 0$. Temporal coherence is also critical for interferometric imaging and radar systems in general [56, 57] and will be examined later in this chapter. The integration process in (3.6) can be written for a set of N points, after discretization, as the mutual coherence matrix γ [40, 58], whose entries γ_{ij} are the dot product of the point responses ϵ_i and ϵ_j,

$$\gamma_{ij} = \frac{|\epsilon_i \epsilon_j^H|}{||\epsilon_i||||\epsilon_j||} \tag{3.7}$$

where $1 \leq i, j \leq N$. If γ_{ij} is close to 1, this indicates high spatial coherence, while γ_{ij} close to 0 indicates low coherence (incoherence); intermediate values $0 < \gamma_{ij} < 1$ correspond to partial coherence. In the example of Fig. 3.3 two points in the same circle arc will have $\gamma_{ij} = 1/2$, and for N transmitters $\gamma_{ij} = 1/N$.

3.3 Modeling Coherence from Multiple Sources

In a two-dimensional space (x, y) the electric field from N noise sources at a carrier frequency f_c with bandwidth Δf can be found as a function of time as

$$E(x, y, t) = \sum_{i=1}^{N} \int_{f_c - \frac{\Delta f}{2}}^{f_c + \frac{\Delta f}{2}} a_i(f) exp(j2\pi f t + \phi_i(t)) * \frac{\delta(t - R_i/c)}{R_i} \, df \tag{3.8}$$

where $\alpha_i(f)$ is the random amplitude of the signal emitted by the ith transmitter antenna, $\phi_i(t)$ is the random signal phase, and $R_i = \sqrt{(x - x_i)^2 + (y - y_i)^2}$ is the distance of each point (x, y) from the transmitters locations (x_i, y_i). The spatial coherence was evaluated and simulated in MATLAB for a set of three 37 GHz incoherent sources TX1, TX2, and TX3 placed in a rectangular grid (x,y) at locations (-0.1,0), (0.1,0), and (0.15,0) meters, respectively. The image segment where mutual coherence was measured was set to be the line connecting the points (-1,2.61) and (1,2.61). The simulated mutual coherence is shown in Fig. 3.4 where γ is plotted for all three transmitters in Fig. 3.4(a) and for TX1 and TX2 in Fig. 3.4(b). The matrices are symmetric, as we are interested in the normalized magnitude of degree of coherence, and its diagonal elements are unity because each spatial point is self-coherent. Most of the terms γ_{ij} where $i \neq j$, representing the points outside

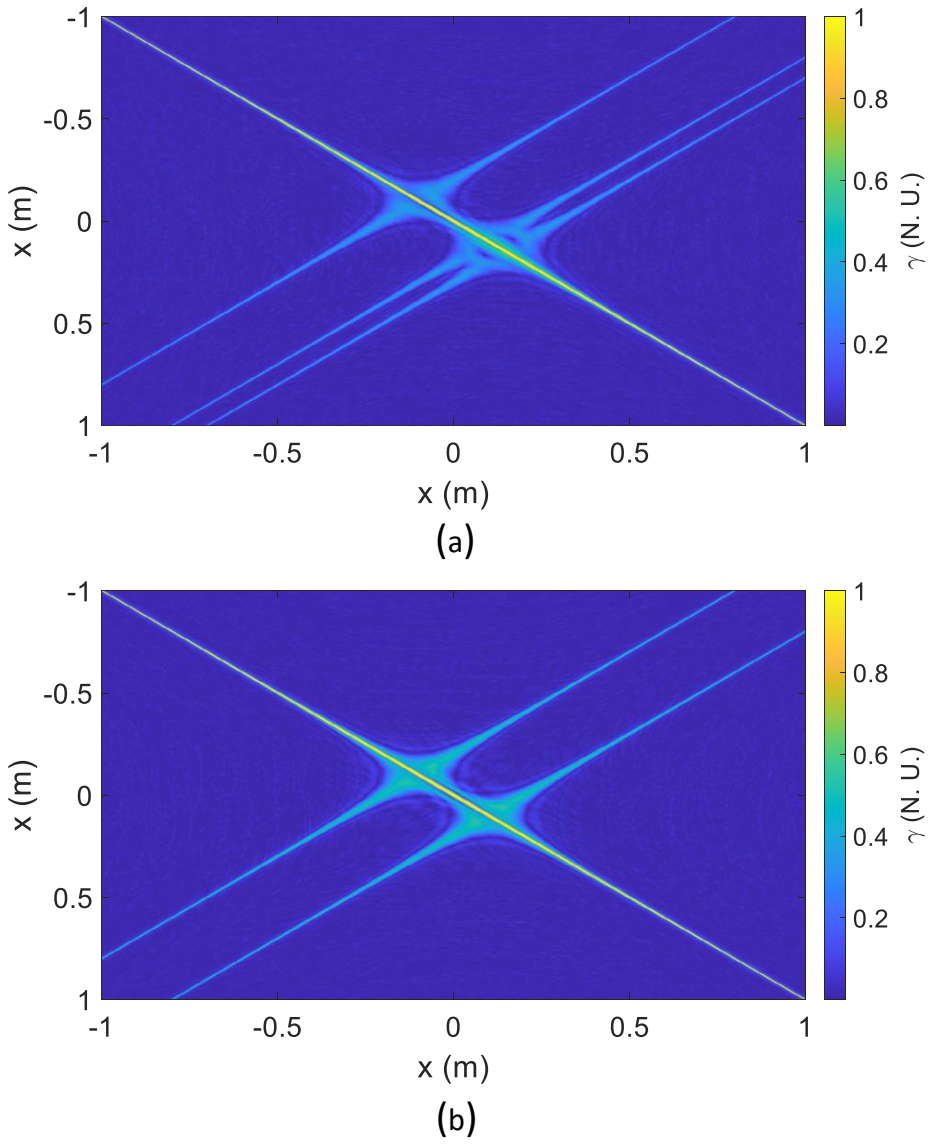

Figure 3.4: Simulations of the mutual coherence matrices γ at a one-dimensional image plane in the cross-range dimension for (a) three incoherent sources and (b) two incoherent sources. The unity diagonal elements represent the self-coherence of every point. As expected, every spatial point should be coherent with itself. The additional lines represent partial coherence from the emitter wavefronts, with coherence of $\frac{1}{3}$ for $N = 3$ and $\frac{1}{2}$ for $N = 2$. N incoherent transmitters yield N partial coherence lines with amplitude $\frac{1}{N}$. Image [6] © 2021 IEEE.

of the wavefront arc, are negligible because of the spatial incoherence, however in Fig. 3.4(a) three partial coherence lines appear with amplitude $\frac{1}{3}$, and in Fig. 3.4(b) two partial coherence lines show up with amplitude $\frac{1}{2}$. These lines are due to the intersection of the circular wavefronts

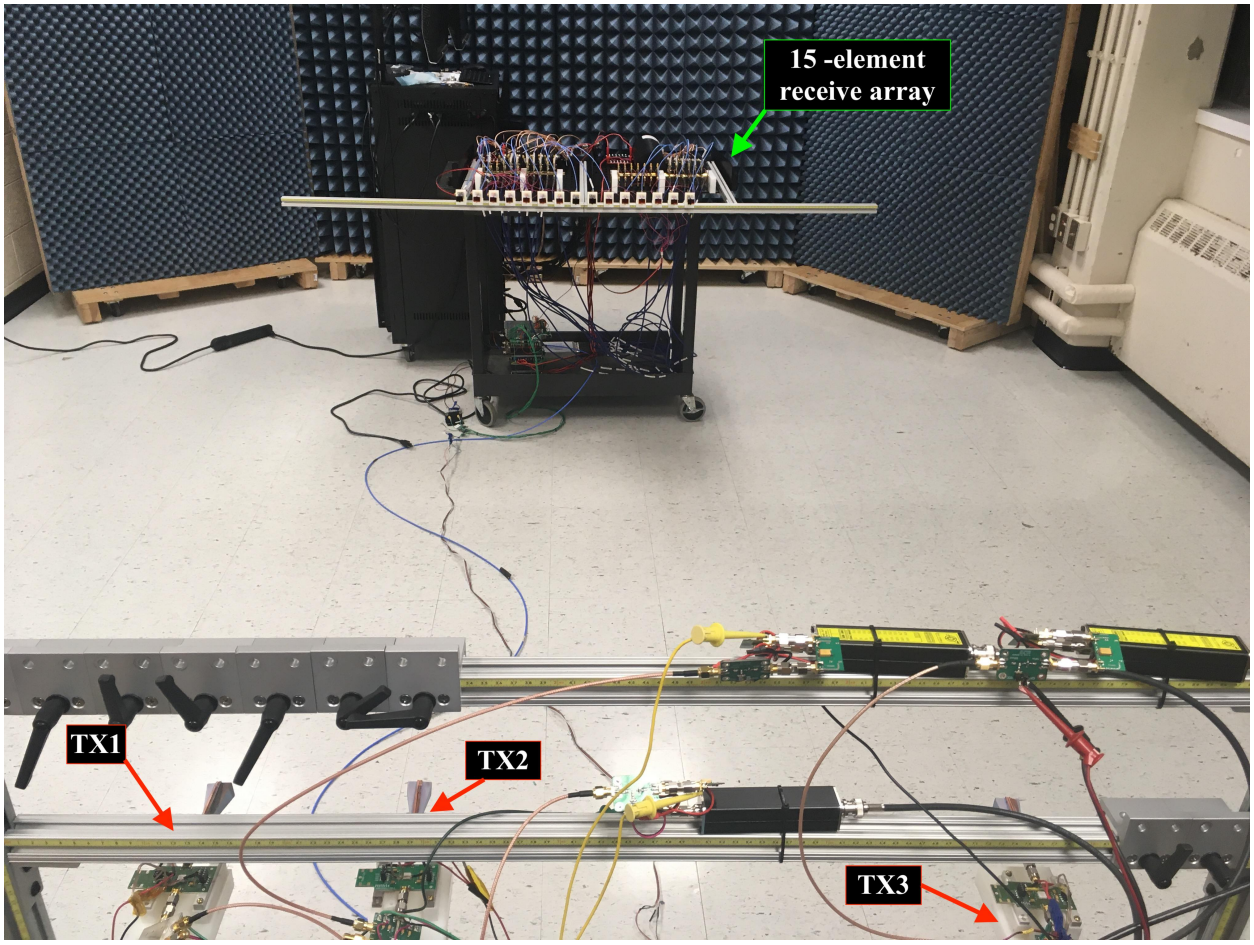

Figure 3.5: Experimental setup for measuring the mutual coherence on a line segment using 15 receivers and three transmitters. Image [6] © 2021 IEEE.

coming from the three sources with the line segment, and do not indicate the antenna locations.

Using N incoherent transmitters will result in N partial coherence lines in the image plane with $\gamma_{ij} = \frac{1}{N}$. As the number of elements increases, more partial coherence lines will appear but with lower amplitude. Thus, by adding more transmit sources, spatial coherence is significantly reduced at the image plane. The next section presents experimental measurements to verify our analysis for the image plane coherence. A simple script that can be used to simulate evaluation of coherence in the spatial domain can be found in Appendix B.

3.4 Experimental Measurements of Partial Coherence from Incoherent Sources

Experimental measurements were conducted inside a semi-anechoic environment at a carrier frequency of 37 GHz in order to verify the spatial transmitter coherence analysis. 15 dBi 3D-printed horn antennas were used for both transmitters and receivers. For the receivers each antenna was followed by a 20 dB gain Analog Devices (ADI) HMC1040LP3CE low-noise amplifier (LNA) before being downconverted to baseband using a 37-44 GHz quadrature downconverter (ADI HMC6789BLC5A). Their outputs were captured using two ATS9416 14 bit, 100 MS/s, AlazarTech waveform digitizers installed on a computer in master-slave mode. The three transmitters consisted of three calibrated 15 dB Excess Noise Ratio (ENR) noise sources which were amplified at baseband, and then upconverted to 37 GHz using ADI HMC6787ALC5A 37-40 GHz upconverters. Three power amplifiers ADI HMC7229LS6 were used to amplify the 37 GHz signal to a maximum transmit power of -8 dBm. The total signal power over a bandwidth of 50 MHz was approximately 2 dBm for every transmitter.

The experimental configuration can be seen in Fig. 3.5. The receive array consisted of 15 antennas spaced uniformly in 5 cm increments as seen at the top of Fig. 3.5. Receive elements are numbered from 1 to 15 with the receiver 1 being the receiver at the top right side of the picture, while receiver 15 is the one at the top left side of the picture. The sampling rate was 100 MSamples/s and the integration time 1.6 ms. The receivers were calibrated using redundant spacings [11, 59]. The distance between transmitters and receivers was 2.62 m. TX1 and TX2 were spaced 0.2 m apart, while TX2 and TX3 were spaced 0.51 m apart. The locations here are sparse compared to the discretized grid in the simulations of the previous section, however they are a useful indicator for how the partial coherence in the image plane behaves as a function of number of transmitters and transmit element spacings. The results can be seen in Fig. 3.6 for (a) all three noise sources, (b) TX1 and TX3, and (c) only TX1 transmitting. The matrix is normalized columnwise and due to residual calibration errors is not perfectly symmetric. It can be seen that the three noise sources in Fig. 3.6(a) produce significantly more incoherent radiation than the two

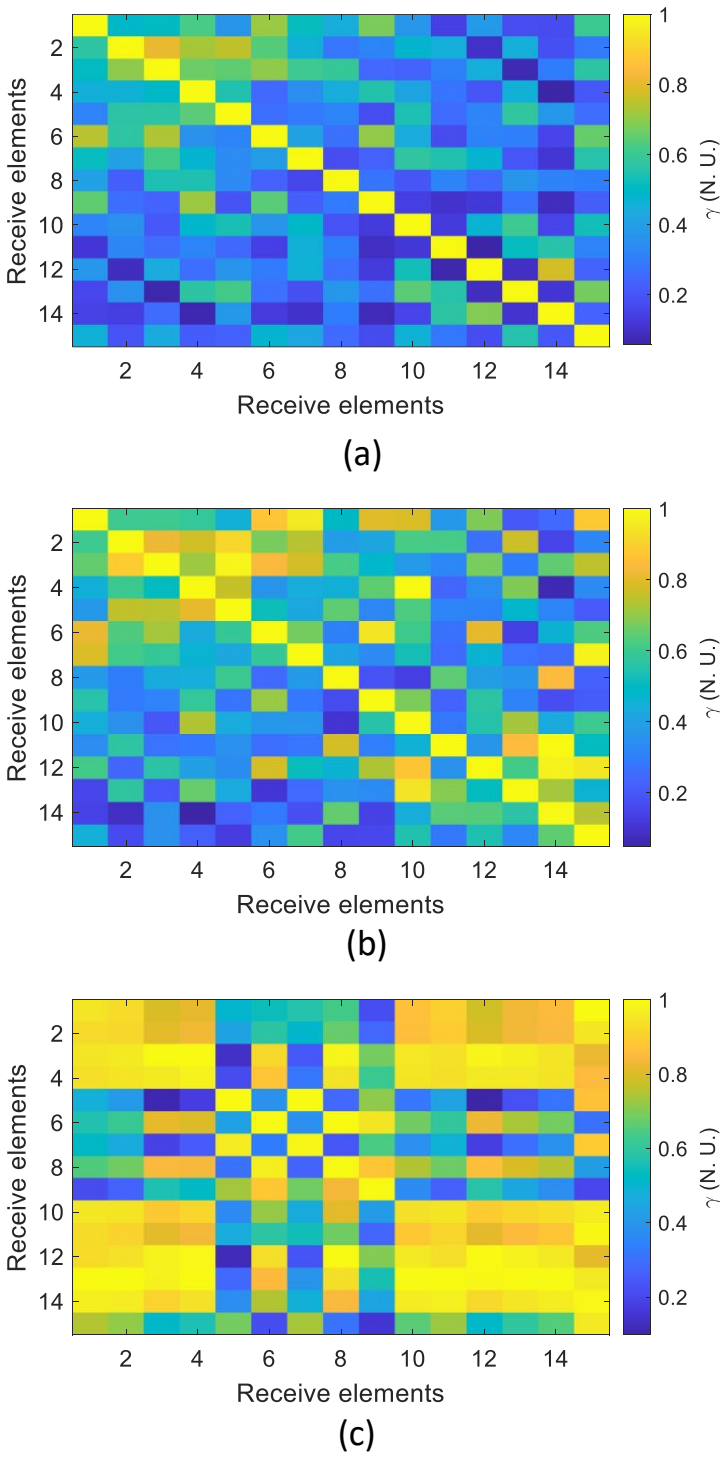

Figure 3.6: Experimentally measured coherence matrices γ using (a) three incoherent transmitters, (b) two incoherent transmitters, and (c) one incoherent transmitter, showing lower mutual coherence (higher incoherence) as the number of emitters increases. Image [6] © 2021 IEEE.

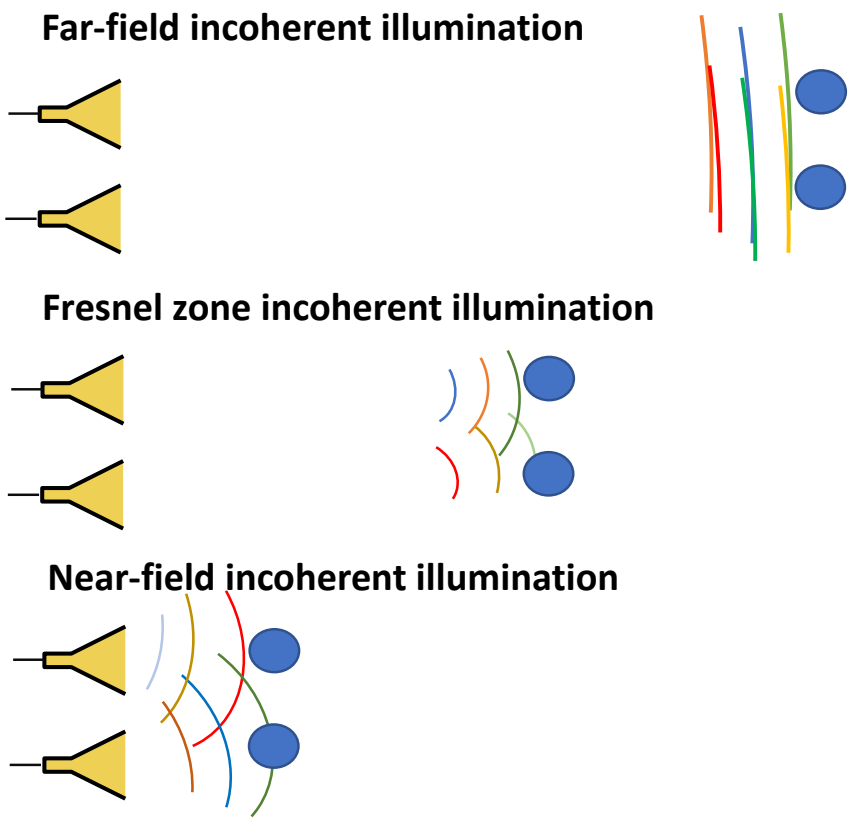

Figure 3.7: A comparison between far-field (top), Fresnel zone (middle), and near-field (bottom) incoherent illuminations. Far-field radiation gives very similar contributions at the two targets and this can be seen from the superposition of the planar wavefronts. Fresnel zone illumination gives more diverse contributions and the two targets on the bottom receive the most diverse contribution from the two transmitters in the near-field. Image [7] © 2021 IEEE.

noise sources in Fig. 3.6(b), where the partial coherence lines that are significantly higher than the image noise floor, which is due to hardware imperfections and variations between the transmitter power levels, start to appear. Fig. 3.6(c) shows that a single noise transmitter produces significant correlation in the scene, thus active interferometric imaging requires multiple incoherent transmitters when imaging in even one dimension. While the measurement was not optimized to mitigate multipath or other environmental reflections, there is nonetheless significant agreement between simulation and measurement.

3.5 Coherence in the Cross-Range Dimension in Different Radiation Zones

In order to investigate the effect of distance from the transmitter array on the spatial coherence in the cross-range dimension, one can consider two millimeter-wave incoherent noise transmitters residing on the x-y plane, where the ith transmitter resides at $(x_i, 0)$. For the interferometric processing to succeed, each spatial point response needs to be sufficiently different from the other spatial points in the scene. When multiple independent transmitters illuminate the scene with incoherent noise signals, their superposition may not be completely spatially incoherent. As seen in Fig. 3.7, the signals impinging on the two targets manifest different contributions of the incoherent signals when illuminated from far-field radiation (top), Fresnel zone (middle), and near-field illumination (bottom). In the case of far field, the two targets observe similar contributions of the phase wavefronts, denoted with green and yellow colors. On the other hand, in the near-field case at the bottom of Fig. 3.7, the circular wavefronts yield very different contributions on the targets. The Fresnel zone illumination acts as a combination of the near and far-field radiation.

The impact of distance was evaluated via simulations of the two-dimensional fields from $N = 2$ transmitters using (3.8). The simulations were performed in MATLAB. I consider the far field of an array with maximum element spacing D to be $R > \frac{2D^2}{\lambda}$ [29]. Fresnel zone is the region that satisfies $0.62\sqrt{\frac{D^3}{\lambda}} \leq R \leq \frac{2D^2}{\lambda}$ and near-field is the region that satisfies $R < 0.62\sqrt{\frac{D^3}{\lambda}}$.

The resulting mutual coherence matrices can be seen in Fig. 3.8(a)-(c). The two noise sources were placed at locations $(D/2, 0)$ and $(-D/2, 0)$. All the computations correspond to the scene being a one-dimensional line connecting the points $(1, 5)$ m and $(-1, 5)$ m. The transmitter separation was changed to simulate the far-field, Fresnel zone, and near-field with respect to the transmit baseline. The results in Fig. 3.8(a) are from a transmit separation of D = 20 cm which corresponds to far-field and it can be seen from the main diagonal that every point is coherent with itself as expected. However, the anti-diagonal lines with amplitude close to $1/2$ show that almost every spatial point has another point that is partialy coherent with it, which is unwanted coherence. Increasing the transmitter separation to $D = 1.6$ m moves the unwanted partial coherence lines at the edges of the field of view as shown in Fig. 3.8(b) for Fresnel region radiation. This is be-

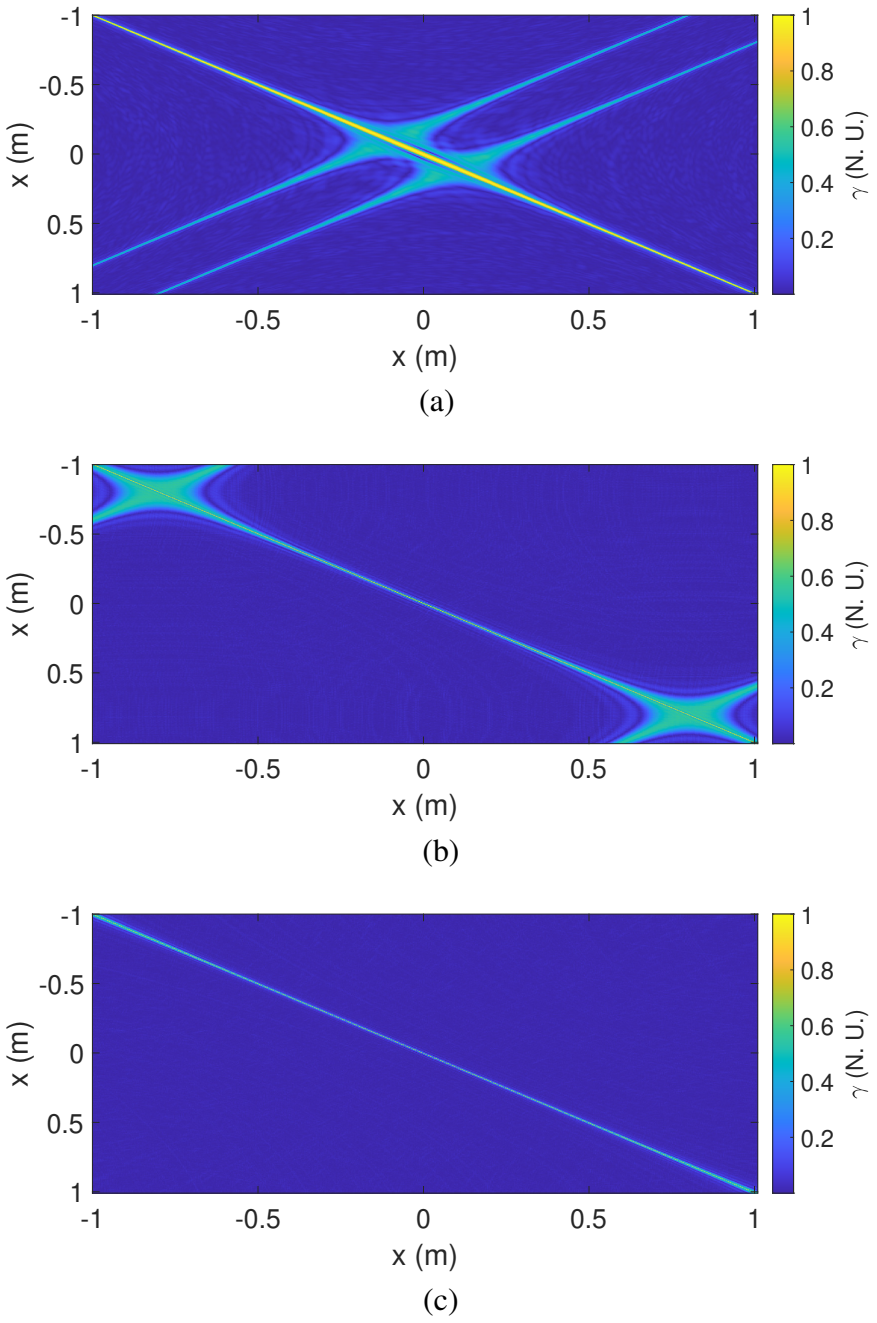

Figure 3.8: (a) Coherence matrix for far-field incoherent illumination using 2 incoherent noise transmitters which shows partial coherence lines with $\gamma = 1/2$ (b) Coherence matrix for Fresnel-zone illumination using 2 incoherent noise transmitters. The partial coherence lines have been pushed at the edges of field of view. (c) Coherence matrix for near-field illumination using 2 incoherent noise transmitters. The partial coherence lines have been pushed outside the field of view of the image reconstruction achieving perfect spatial incoherence inside the field of view. Image [7] © 2021 IEEE.

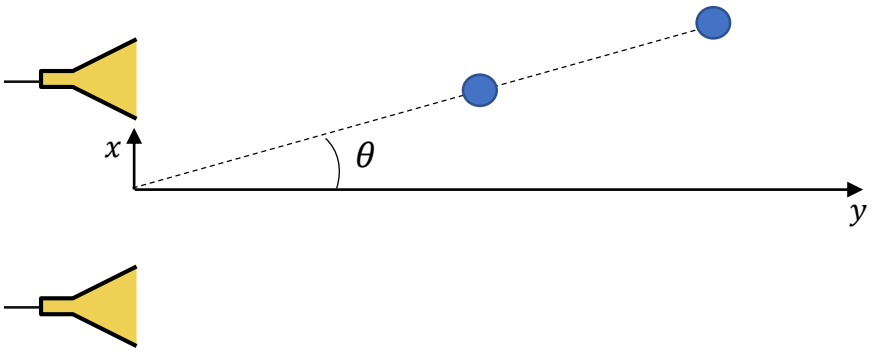

Figure 3.9: Longitudinal spatial coherence refers to the coherence between two spatial points located, indicated with the blue circles, at the same direction θ however at different distances from the origin $(0, 0)$. Image [8] © 2022 IEEE.

cause the intersections of the circular wavefront with the scene get pushed towards the edges of the field of view. Finally, increasing the transmit separation to $D = 2.8$ m completely eliminates any partial coherence line inside the field of view as shown in Fig. 3.8(c). All points inside the one-dimensional scene have unique phase responses which is the ideal scenario for an incoherent illumination leading to reduced image reconstruction errors. As a result, when the incoherent transmit array is operating in the near-field region, the necessary spatial incoherence can be obtained in the cross-range dimension for Fourier domain imaging. However, spatial coherence does not only manifest in the cross-range dimension. In the next section, a metric that describes how coherence propagates in the radial and temporal dimensions is discussed.

3.6 Longitudinal and Temporal Coherence

Longitudinal coherence has been investigated before for light sources in the far-field [60], but not that thoroughly for microwave and millimeter-wave imaging. Longitudinal coherence is concerned with the spatial coherence between two points that have different distances from an illuminating source, but are located at the same angular direction θ, as shown in Fig. 3.9. The longitudinal coherence can be obtained using a similar approach as the spatial coherence, but between every two points along a line of constant angle. While this can be computed for any angle, in this section I consider the case of $\theta = 0^\circ$ since most millimeter-wave imaging systems are usually focused

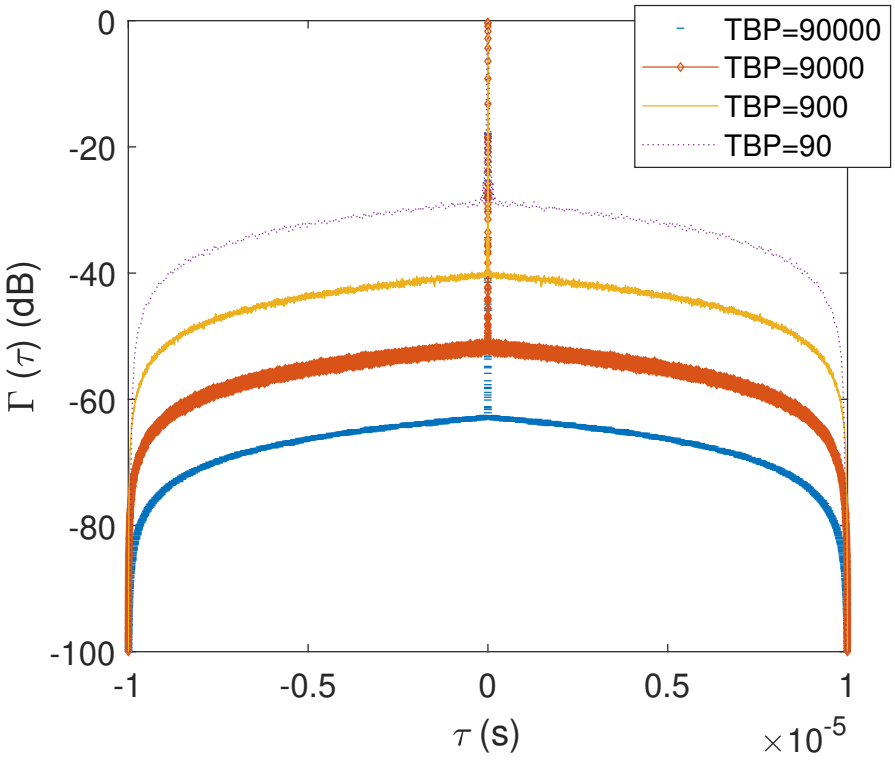

Figure 3.10: Temporal coherence $\Gamma(\tau)$ plotted as a function of time delay τ for different values of TBP. The noise signals are perfectly coherent with themselves for different TBP values when $\tau = 0$, and when $\tau \neq 0$, the temporal coherence values drop significantly. Higher TBP values correspond to lower $\Gamma(\tau)$ values. Image [8] © 2022 IEEE.

towards the broadside direction of the array. This also simplifies the calculations to the case where only one-dimensional lines are considered, which results in two-dimensional coherence functions. Before longitudinal coherence propagation is simulated in the spatial domain, temporal coherence is introduced, which refers to the coherence between two instances of the same electric field or waveform as a function of different time delays and not spatial locations. Temporal coherence can be written as

$$\Gamma(\tau) = \lim_{T\to\infty} \frac{1}{2T} \int_{-T}^{T} E(t)E^*(t-\tau)\, dt \tag{3.9}$$

where $(\cdot)^*$ denotes conjugation and T is the observation time. Eq. (3.9) is an adapted version of (3.6), where the subscripts 1 and 2 have been dropped as it refers to the same wavefront which could be the signal emitted emitted from a source or the signal reflected from a single spatial point.

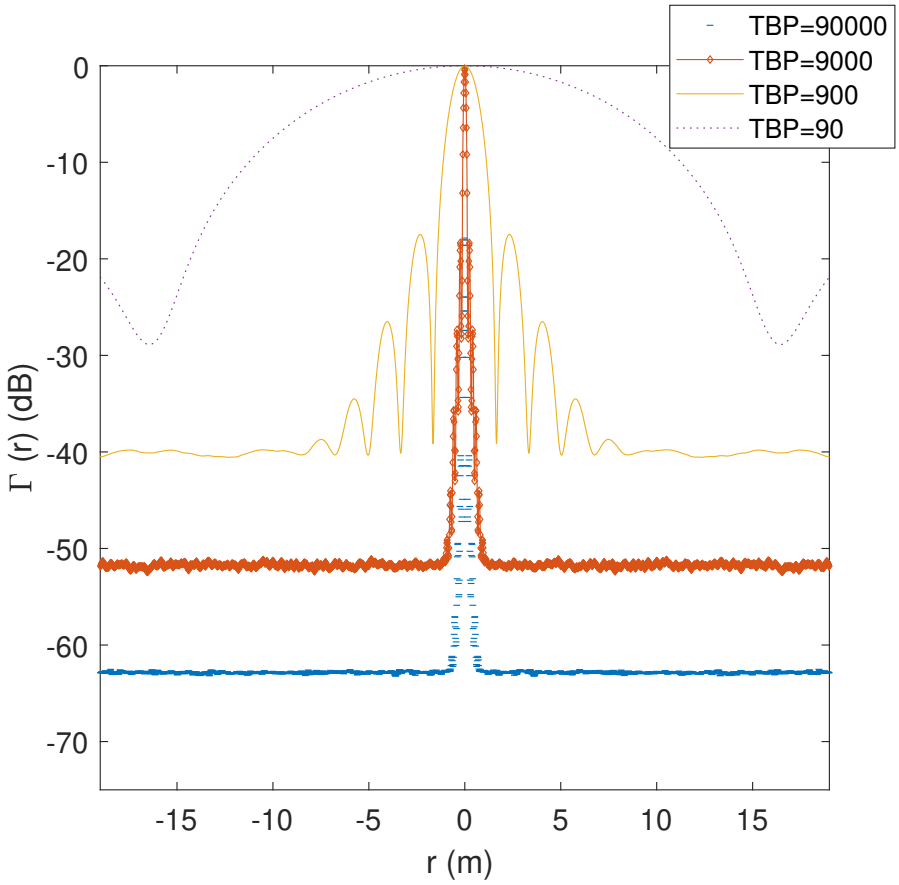

Figure 3.11: Coherence $\Gamma(r)$ as a function of distance $r = c \cdot \tau$ for different values of TBP. While all noise signals are perfectly coherent with themselves, when distance is equal with 0, they decorrelate faster as a function of distance for larger TBP values. Image [8] © 2022 IEEE.

The observation time T is never infinite in actual imaging systems. The time-bandwidth product (TBP) of a signal refers to the product between signal bandwidth B and observation time T. TBP is one of the most important waveform parameters in active sensing, especially for correlation based processing. Its importance in the context of mutual coherence can be described by considering the orthogonality relationships that are used in Fourier series. According to the orthogonality principle, two sinusoidal waveforms at different frequencies have an inner product equal with zero. Two signals with 1 Hz frequency difference will appear almost identical for a time interval in the order of μs, however their differences manifest strongly for longer time intervals, on the order of seconds. The TBP thus enables the determination of the desired bandwidth and time length of a waveform to minimize the mutual coherence. The connection between TBP and temporal coherence can be

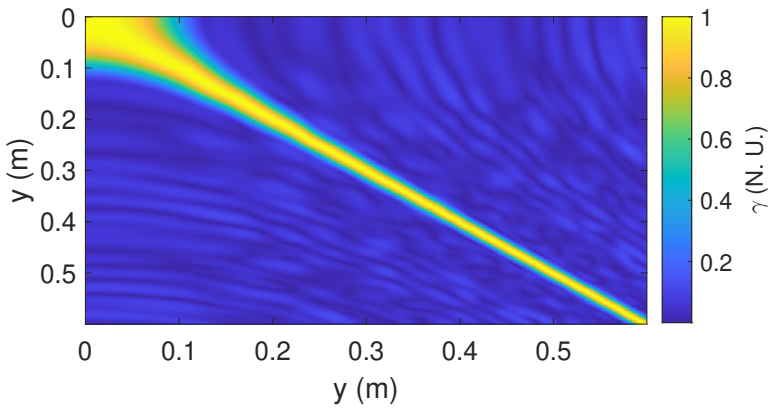

(a)

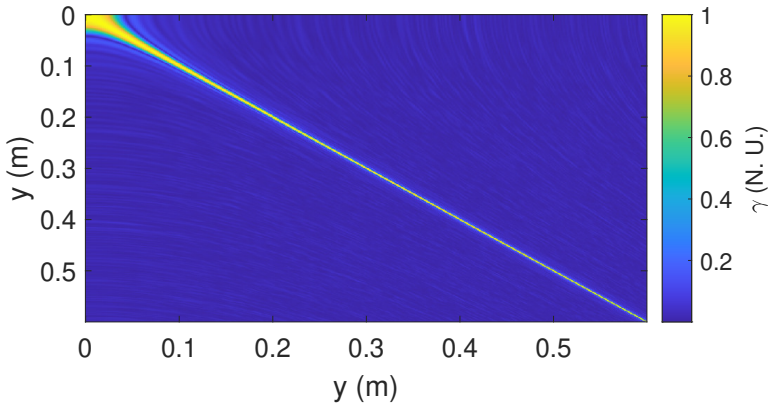

(b)

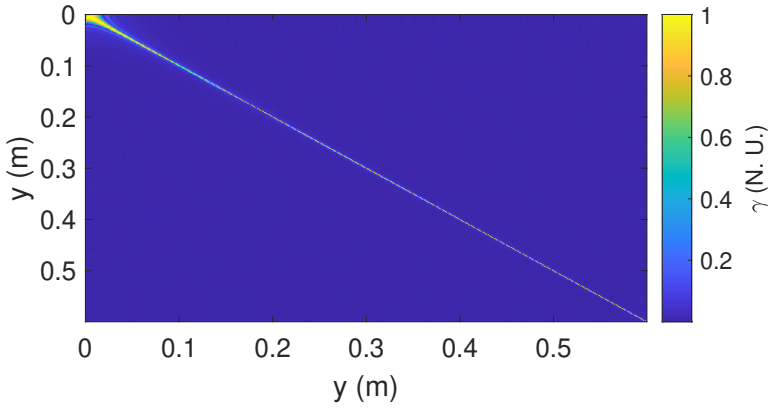

(c)

Figure 3.12: Longitudinal coherence simulations at $\theta = 0°$ for two sources located at $(-0.5, 0)$ m and $(0.5, 0)$ m for (a) TBP $= 190$, (b) TBP $= 1900$, and (c) TBP $= 9500$. Close to the origin $(0, 0)$ there is an area with high spatial coherence which becomes narrower as TBP values increase. Image [8] © 2022 IEEE.

seen by considering a baseband noise signal with duration 10 μs. Fig. 3.10 shows the temporal coherence of this signal versus time delay τ and TBP. The $\Gamma(\tau)$ values are the result of 1000 Monte Carlo simulations run in MATLAB. Although every waveform is perfectly self-coherent for zero time delay ($\Gamma(0) = 1$), all plots start to drop sharply for non-zero τ values. Additionally, the higher TBP values correspond to lower $\Gamma(\tau)$ values. A waveform with large enough TBP can maintain low coherence characteristics in the case of strong multipath reflections, as shown in Fig. 3.11, which is a magnified version of Fig. 3.10, plotted as a function of distance $r = c \cdot \tau$, where c is the wavefront propagation speed.

The longitudinal coherence was evaluated at $\theta = 0^\circ$ through a MATLAB simulation for two incoherent millimeter-wave transmitters located at $(-0.5, 0)$ m and $(0.5, 0)$ m. The simulation shows the coherence along the line segment x = 0, from $y = 0$ to 0.6 m. The carrier frequency was 38 GHz. The results can be seen in Fig. 3.12(a) for TBP $= 190$. It can be seen that the coherence is mostly focused on the main diagonal, however very close to the origin $(0, 0)$ there is an area that shows increased values of $\gamma = 1$. This is very similar to what happens in the far-field illumination. The points that lie very close to the line segment that connects the two transmitters get very similar contributions from both transmitters. There is a trade-off between the near-field spatial coherence at the cross-range, that was examined in the previous section, and the longitudinal coherence. Although being in the near-field of a transmit array shows improved spatial coherence in the cross-range, this is not the case for the longitudinal coherence. This is not problematic in active incoherent millimeter-wave systems that employ a transmit array collocated with a receive interferometric array since this would mean that the targets need to be exactly next to the receive array. However, issues of unwanted high spatial coherence could arise in the case of non-cooperative incoherent imaging, which is discussed in chapter 5. Two targets can be very close on the line that connects two transmitters and this would result in reflected wavefronts with high coherence. As for the case of TBP = 1900 that is shown in Fig. 3.12(b), the main diagonal line is much narrower than earlier; nevertheless, close to the origin (0,0), there is still a non-negligible area of high spatial coherence. Furthermore increasing the TBP to 9500 (Fig. 3.12(c)) makes both

the main diagonal and the area next to the origin even narrower. Shortening the transmit baseline also helps with reducing the area of high longitudinal coherence. The effects of temporal coherence will not be easily observed while simulating the spatial coherence in the cross-range dimension. In Fig. 3.8(a), decreasing the temporal coherence does not mitigate the partial coherence lines with amplitudes close to 1/2. These lines are the result of the locality of the sources and the intersections of the same phase wavefront in the one-dimensional scene will not disappear even with very large TBP values. However, the area that is present where partial coherence lines and self coherence lines intersect will shrink. A simple script that can be used to evaluate the longitudinal coherence in the spatial domain can be found in Appendix C.

3.7 Experimental Measurement at Microwave Frequencies

After investigating how coherence propagates in space, verification measurements of the active interferometric imaging method were conducted in a semi-enclosed antenna range, using metal spheres for targets. The overall measurement system is shown in Fig. 3.13, and consists of three transmit antennas and two receive antennas. The transmit signals were generated using a Keysight M8190 Arbitrary Waveform Generator (AWG). The maximum output power of the AWG was -9 dBm per frequency bin. The amplifiers each had a gain of 9 dB and a 1 dB compression point of 19 dBm. The transmit antennas were 20 dBi standard gain horn antennas and three of them were used in order to achieve spatial incoherence in the two angular directions. The antennas were placed on a 7.3 m diameter arch range.

The receive interferometric array was synthesized using two receiving elements which were placed pairwise in the array locations to generate the desired sampling function. Because the array was synthesized with a pair of sequentially-moved antennas, this means their phase and amplitude error will be constant in all visibility samples, thus removing the need to calibrate a set of antenna elements, simplifying the proof-of-concept experiments in this section. Since the signals impinging on the scene were spatio-temporally incoherent and interferometric information is acquired on a pair-wise basis, this synthesis approach is valid and has been commonly used in

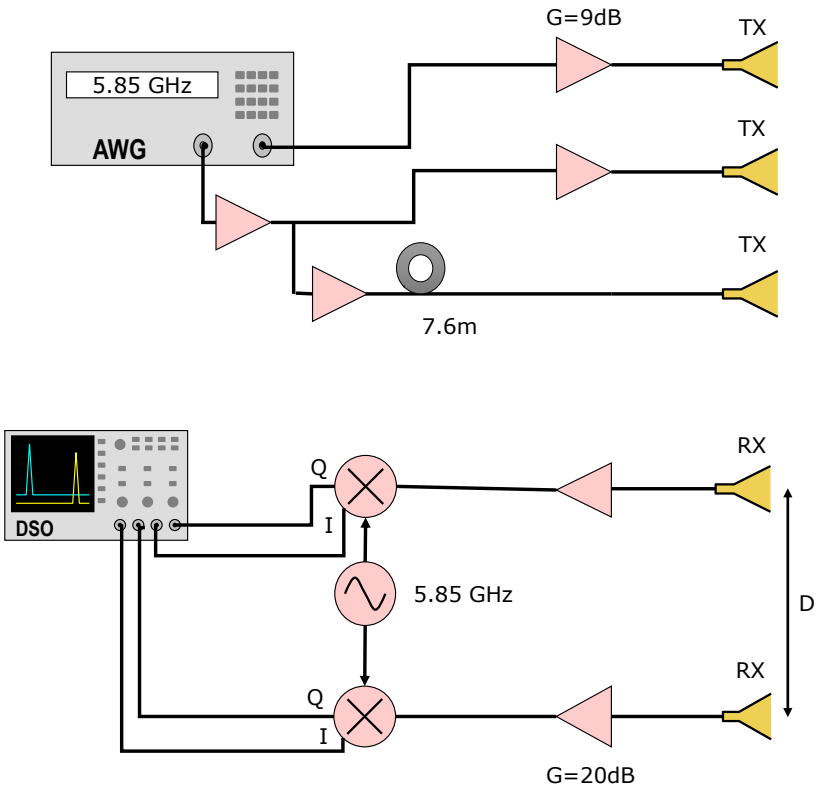

Figure 3.13: Block diagram of the experimental imaging system. The distance D was changing in order to synthesize the one or two-dimensional receiver array. Image [3] © 2018 IEEE.

the past in radio astronomical observations [61]. The receive antennas were 10 dBi broadband horn antennas mounted on the aluminum rack and were moved in the array pairwise locations. The noise reflections from the scene were captured by the received antennas and the signal was then input to a quadrature downconverting mixer ADI ADL5380. Because this system did not include microwave filters, the mixers represent the band-limiting devices in the system. The IF bandwidth of the mixers was 390 MHz, however without filters some signals outside this band were present, in particular due to leakage from the mixer introduced spurious signals. Undersampling and digital low-pass filtering were used to mitigate these spurs. The received signals were captured using a 20 GHz Keysight MSOX92004A oscilloscope at 2.5 GSamples/s in high-resolution mode. The signal and image processing took place offline using MATLAB. Each received signal was filtered to remove dc bias, and the output from each antenna location was cross-correlated with every other antenna location, apart from the redundant antenna baselines.

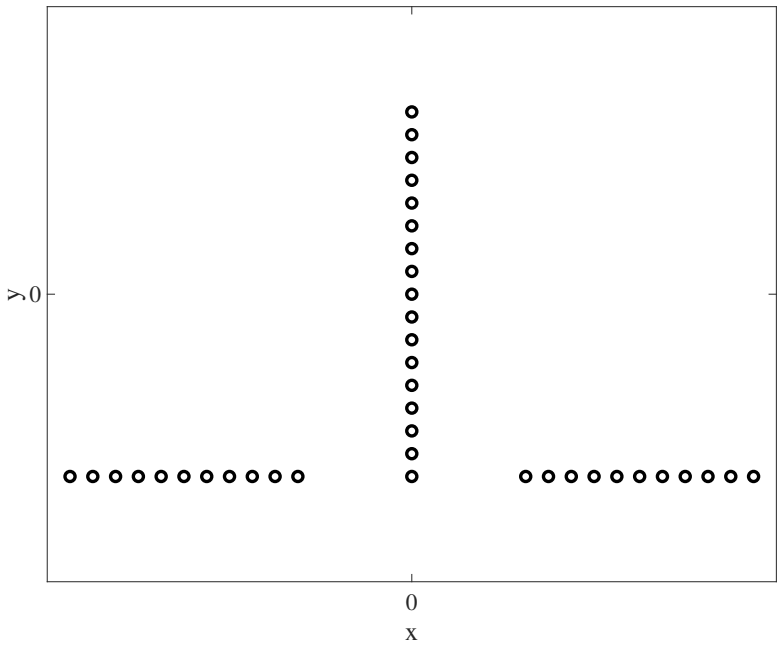

Figure 3.14: Element locations for the two-dimensional imaging setup. Two antennas were used, and moved sequentially until all antenna pairs were represented in the measurement, in $\frac{\lambda}{2}$ increments. The smallest baselines were not achievable due to the physical size of horn antennas. Image [3] © 2018 IEEE.

Coherent processing between the transmit and received signals does not take place in the traditional radar sense. While the cross-correlation processing requires the receivers to be phase locked, no explicit knowledge of the transmit waveform is necessary, other than the statistical requirement of spatial and temporal incoherence. The system architecture is therefore quite simple compared to many coherent radar and imaging architectures, and the transmitters can be completely separate from the receiving array.

The transmit incoherent noise signals were centered at a carrier frequency of 5.85 GHz. Two spheres were placed in the center of a semi-anechoic environment with 7.3 m diameter, seen in Fig. 3.15. Three incoherent noise transmitters were used in order to produce a sufficient noise-like transmit pattern in both the azimuth and elevation planes.

The Keysight M8190 AWG was used to produce the noise signals, however because only two independent outputs are available on the M8190, one of the outputs was split in two using a wide-

Figure 3.15: Two conductive spherical targets used as the two-dimensional scene. Image [3] © 2018 IEEE.

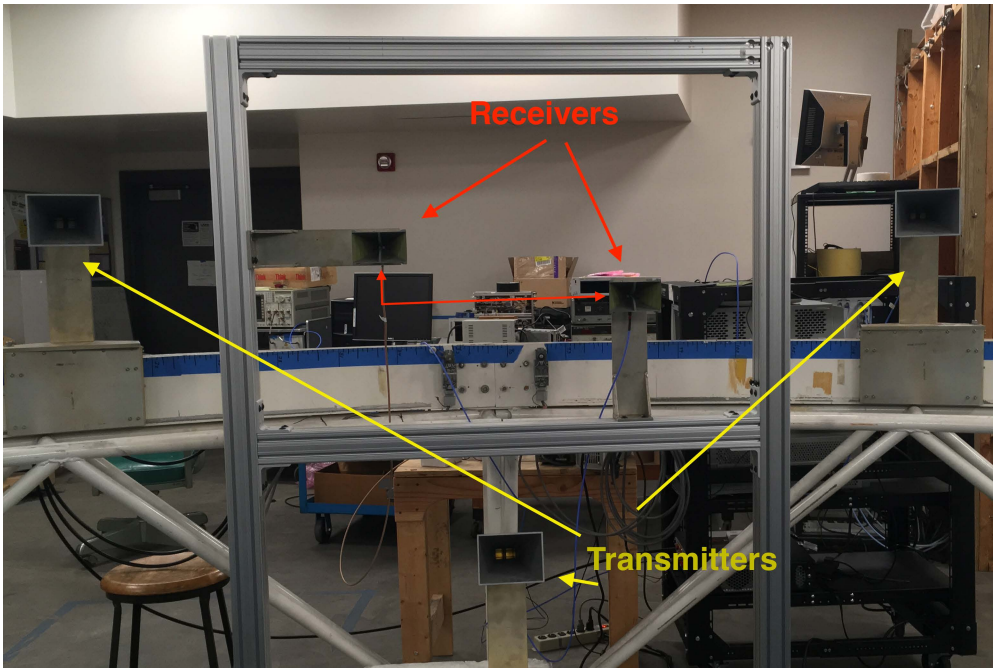

Figure 3.16: Configuration for the two-dimensional microwave experimental measurements with three noise transmitters and two receivers. The transmitter locations were not moved, while the receive antennas were sequentially moved to the locations of the inverted T-array. Image [3] © 2018 IEEE.

band power splitter to generate two noise signals. One output of the splitter was connected to one transmitter, while the other output was connected to the second transmitter through a 7.6 m cable

Table 3.1: Comparison of bandwidth and integration time between passive imaging and active incoherent microwave imaging

	[62]	[63]	[64]	[65]	[66]	[67]	**[3]**
Bandwidth	10 GHz	7 GHz	200 MHz	1 GHz per pixel	40 GHz	20 GHz	**25 MHz**
Integration time	100 ms	3 s	1 ms to 1 s	30 ms per pixel	1 ms per pixel	2.5 ms per pixel	**10 µs**

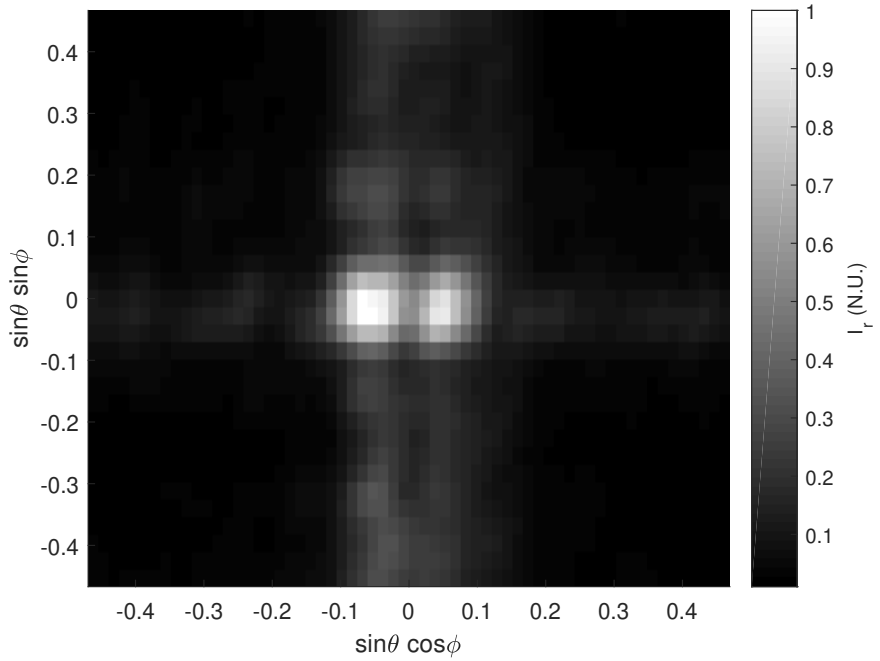

Figure 3.17: Reconstructed two-dimensional image from a T-array with 0.5 λ minimum spacing between the elements in grayscale format. The amplitude is normalized, hence the colorbar axis is in normalized units (N.U.). Image [3] © 2018 IEEE.

(see Fig. 3.13). This additional delay ensured that the transmitted signals were temporally incoherent when the signals were incident on the scene. In practice, three separate noise transmitters would be the preferred option. An additional 9 dB gain amplifier with a 1 dB compression point of 19 dBm was used to overcome the losses from the splitter and the 7.6 m cable.

The array that was synthesized was an inverse T-array, with elements placed in the locations indicated in Fig. 3.14 using the rack in Fig. 3.16 and the two wideband receive antennas. By moving the one in the horizontal and the other in the vertical direction, the T-array was synthesized

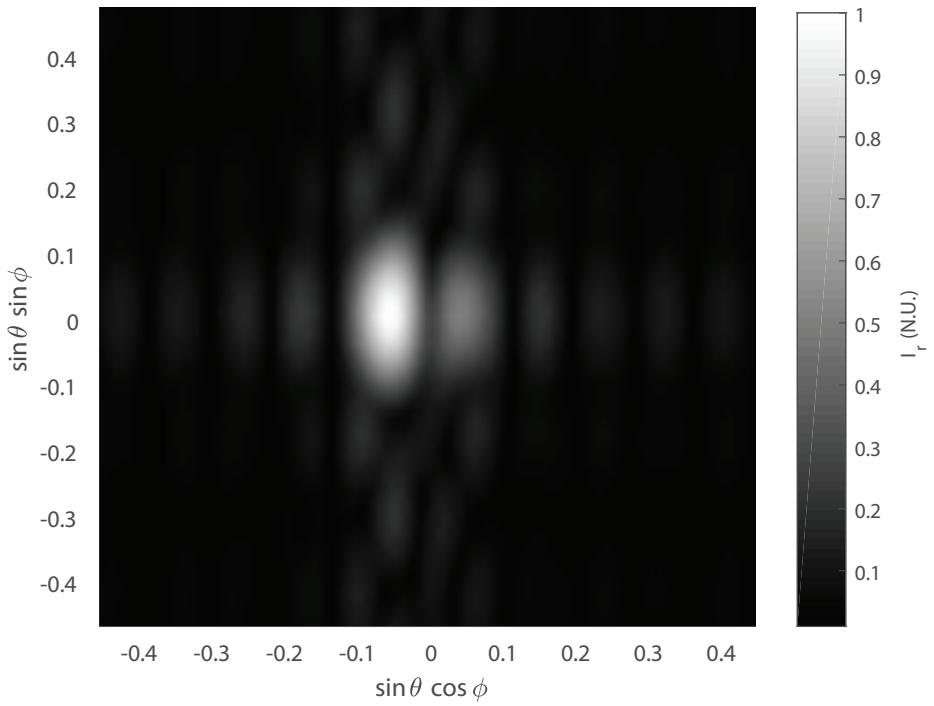

Figure 3.18: Simulated two-dimensional dual target reconstruction from a T-array. The amplitude is normalized, hence the colorbar axis is in normalized units (N.U.). Image [3] © 2018 IEEE.

with a maximum spacing of 15λ in the horizontal axis and 8λ in the vertical axis, and a minimum spacing of 0.5λ. The two received signals were amplified with 20 dB LNAs, downconverted with the quadrature mixers, and then captured using the 20 GHz MSOX92004A oscilloscope in high resolution mode. The captured files were processed offline using MATLAB, where they were low-pass filtered to a bandwidth of 25 MHz. After removing dc bias, cross-correlation was applied to each antenna pair, ignoring the redundant baselines. The integration time was 10 µs. Both bandwidth and integration time are significantly lower than what is typically used in passive microwave and millimeter-wave imagers, where wide bandwidth and long integration times are required to overcome the minimal signal-to-noise ratio resulting from the very low power thermally generated electromagnetic signals. Table 3.1 presents a comparison of these parameters for the proposed system and recent passive imagers from the literature, showing that the proposed system obtains two-dimensional images with an order of magnitude reduction in both bandwidth and integration

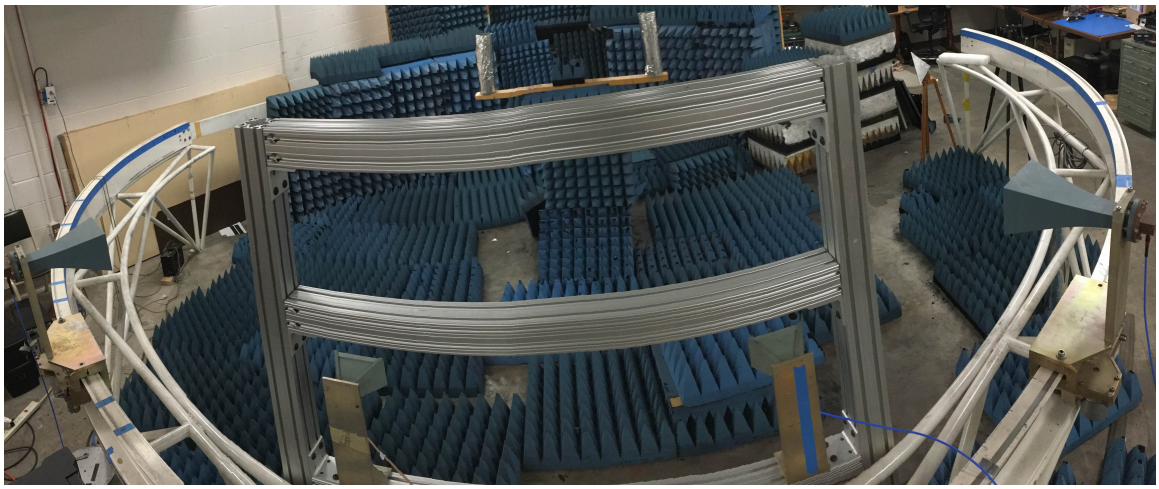

Figure 3.19: Wide-angle image of the one-dimensional imaging system. The horn antennas which were illuminating the scene with noise waveforms are on the left and right, the receive antennas are on the metal frame, along which they were moved to synthesize a filled linear array. The two cylinders are located inside the measurement range. Image [4] © 2020 IEEE.

time.

Fig. 3.17 shows the reconstructed two-dimensional image of the two reflecting spheres. The stronger response comes from the sphere shown in the left side of Fig. 3.15 which has a radius of 18 cm, while the weaker response comes from the sphere on the right with radius of 12 cm. After the inverse Fourier transform was applied to the sampled visibility, a Gaussian smoothing filter was applied. The strong match between the measured two-dimensional image compared to the simulated image of Fig. 3.18 demonstrates the feasibility of the active interferometric imaging method. The simulation, shown in Fig. 3.18, took place in MATLAB for the same array locations used in the experiment.

3.8 Analysis of Array Sparsity in Active Incoherent Imaging Arrays

One benefit of interferometric imaging systems is the use of very sparse antenna arrays, which can significantly reduce the total system cost. In this section, the array sparsity is investigated in

© 2020 IEEE. Section 3.8 is adapted with modifications, with permission, from "S. Vakalis and J. A. Nanzer, "Analysis of Array Sparsity in Active Incoherent Microwave Imaging," in IEEE Geoscience and Remote Sensing Letters, vol. 17, no. 1, pp. 57-61, Jan. 2020".

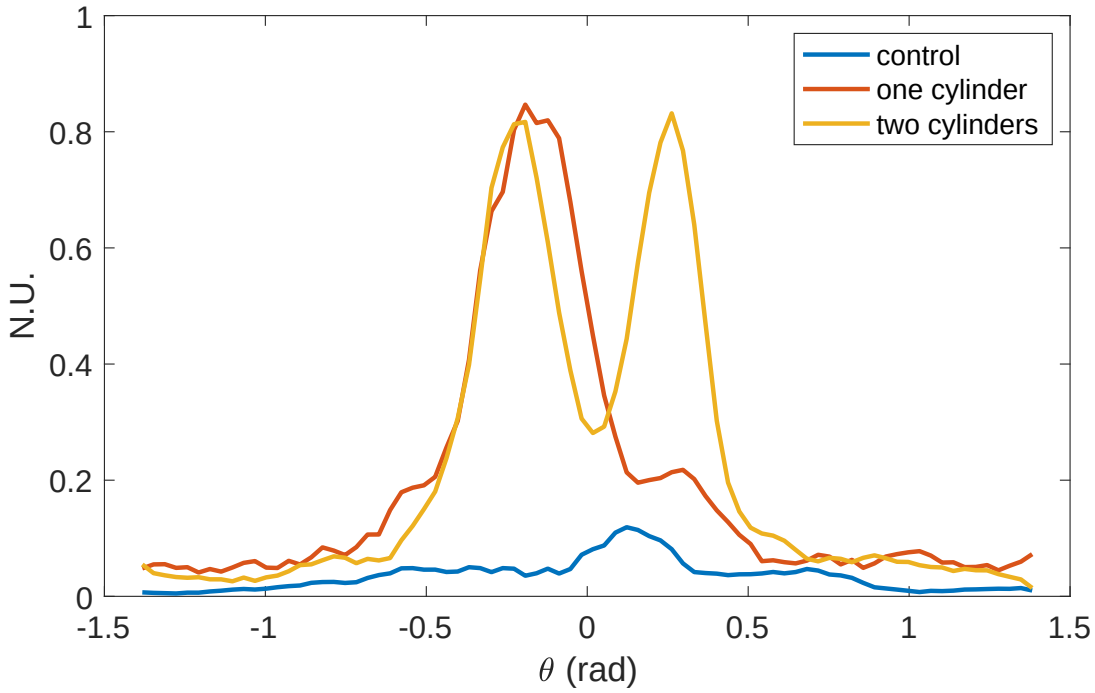

Figure 3.20: One-dimensional image reconstruction of a control scene (no targets present), one cylinder, and two cylinders, using data from a filled linear array consisting of all receiver locations. The amplitudes are normalized, hence the vertical axis is in Normalized Units (N.U.). Image [4] © 2020 IEEE.

a single dimension. Since the experimental measurements were implemented in one dimension, two transmitters were used, each emitting Gaussian noise. The transmit waveforms were generated using the same two-channel AWG used in the previous section, connected to two 15 dBi gain horn antennas. The scene consisted of two cylinders, covered in alumined tape, which were located at the center of a 7.3 m arch range, with the transmit and receive antennas located on the edge of the range (see Fig. 5.7). For the receive array, the fact that each antenna collects incoherent signals from the scene was leveraged, allowing a larger aperture to be synthesized by collecting data pairwise with only two receive antennas, and sequentially moving them to the locations of a filled linear array. This process yields image formation equivalent to capturing the signals simultaneously in a filled array. The receive array had a maximum dimension of 19.5 λ, with the transmitters located just outside this span. The received signals were captured using 10 dBi gain horn antennas, which were low-noise amplified and then downconverted to baseband using quadrature RF mixers

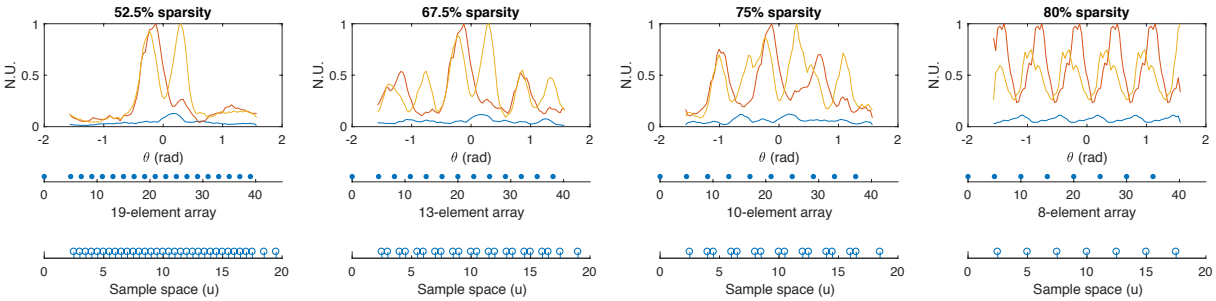

(a)

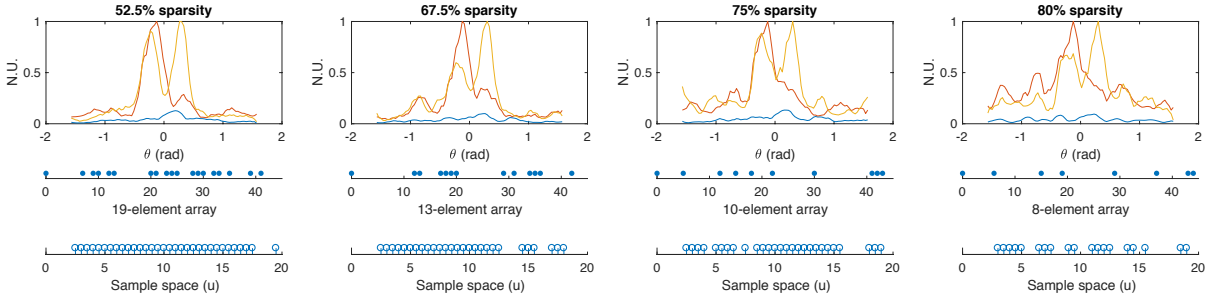

(b)

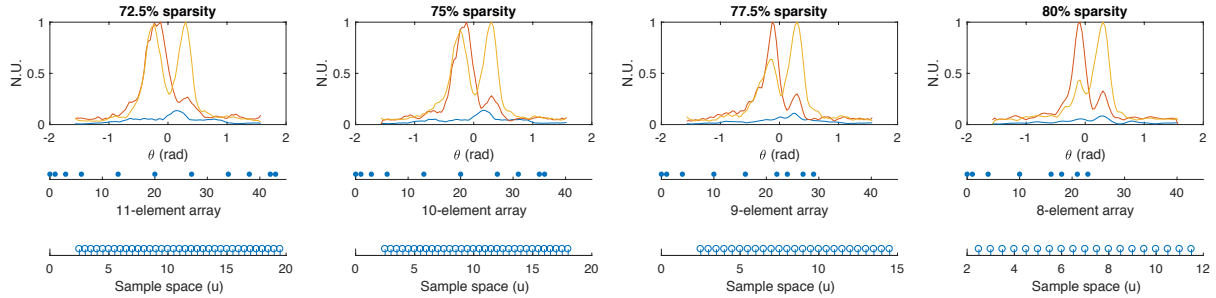

(c)

Figure 3.21: Image reconstructions of the same one-dimensional scenes as Fig. 3.20 with sparse receiver arrays. Array thinning was implemented using (a) uniform thinning, (b) random thinning, and (c) minimum-redundancy array designs. For each implementation four increasingly sparse designs were implemented. Each plot shows the reconstructed images, the array layout, and the resulting sampling function. Uniform thinning results in undersampling of the spatial frequency information, leading to aliasing. Random thinning minimizes aliasing, however the image reconstruction becomes visibly worse as the sparsity increases. Minimum redundancy arrays provide good reconstruction, but are limited in the number of array designs possible. Image [4] © 2021 IEEE.

with a bandwidth of 390 MHz. The baseband received signals were captured using the Keysight MSOX92004A Infiniium Mixed Signal oscilloscope, and were processed in MATLAB.

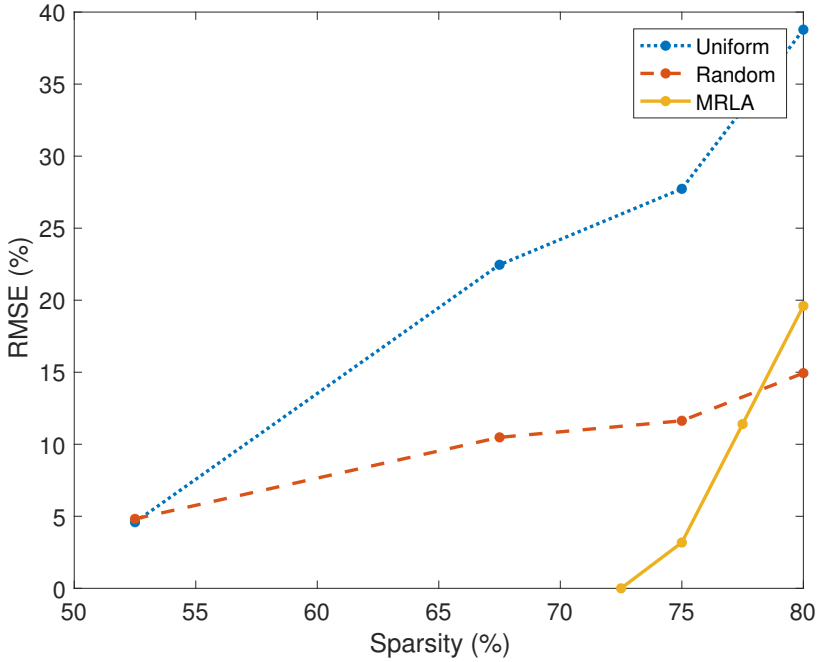

Figure 3.22: Comparison of the relative errors of the sparse image reconstructions of the two cylinders scene relative to the filled-array image reconstruction measured in RMSE. Minimum redundancy linear arrays (MRLA) yield negligible RMSE at a sparsity around 72.5%, increasing to less than 5% at 75% sparsity. Beyond this sparsity level, random arrays provide better error performance. Image [4] © 2021 IEEE.

The digital signal processing consisted of low-pass filtering the response from each element at a bandwidth of 80 MHz, then cross-correlating the responses of each antenna pair corresponding to each spatial frequency and reconstructing the visibility of the source. The sampled visibility was then zero-padded, and then the reconstructed image was obtained using the inverse Fourier transform. Fig. 3.20 shows the reconstructed images of a control scene, one cylinder, and two cylinders using the full 19.5 λ array, captured in the pairwise locations. The responses from the two cylinders can be clearly distinguished in the reconstructed image. Each response was captured for a 10 µs time interval, indicating promise for high-speed operation, which will be investigated in the following chapter.

One of the primary benefits of interferometric antenna arrays is that a filled physical array is not required. Since all data was collected at each antenna location, measured data was removed from

antenna locations in post-processing, a procedure called array thinning [68], and the deterioration of the image relative to that of the filled array was calculated. Three thinning approaches were investigated: uniform thinning, random thinning, and the use of minimum redundancy linear arrays (MRLAs) [37]. MRLAs are sparse antenna arrays that minimally replicate baselines, the layouts of which have been investigated for radio astronomy. The degradation in image formation was analyzed by calculating the RMSE between the image of the two cylinders formed using the full array, and the subsequent images formed using the various thinning methods. Fig. 3.21 shows the reconstructed images, the physical locations of the elements, and the sampling function resulting from the physical layout. Uniform thinning results in undersampling of the spatial frequency information, yielding ambiguities in the reconstructed image. Random thinning provides significantly improved results over uniform thinning, in that no ambiguities are present. Minimum redundancy linear arrays provide good reconstruction performance as well: up to an array thinning of 75% of the full array, MRLA yield image formation degradation of less than 5% RMSE, as shown in Fig. 3.22. For sparsity greater than 75%, minimum redundancy or random arrays provide roughly equivalent performance, with image degradation on the order of 15% RMSE.

The active incoherent imaging approach presented here measures information in the spatial frequency domain, thus the design of the physical aperture is open to greater flexibility than traditional active imagers, enabling conformity to a greater range of applications. Furthermore, the low-bandwidth and short duration waveforms allow the use of simpler receiver architectures, which can lead to imaging systems that are lightweight and low cost, and are easily applicable for numerous active remote sensing applications, including contraband detection, security sensing, search and rescue operations, and vehicular imaging for safety. The signal-to-noise ratio (SNR) will generally impact the image formation quality, however the use of an active transmitter gives the designer greater flexibility to enable operation in high SNR regimes by transmitting higher power when needed.

This section analyzed array sparsity in a one-dimensional imaging system, however the results can be easily extended to two dimensions. While this work showed that minimum-redundancy

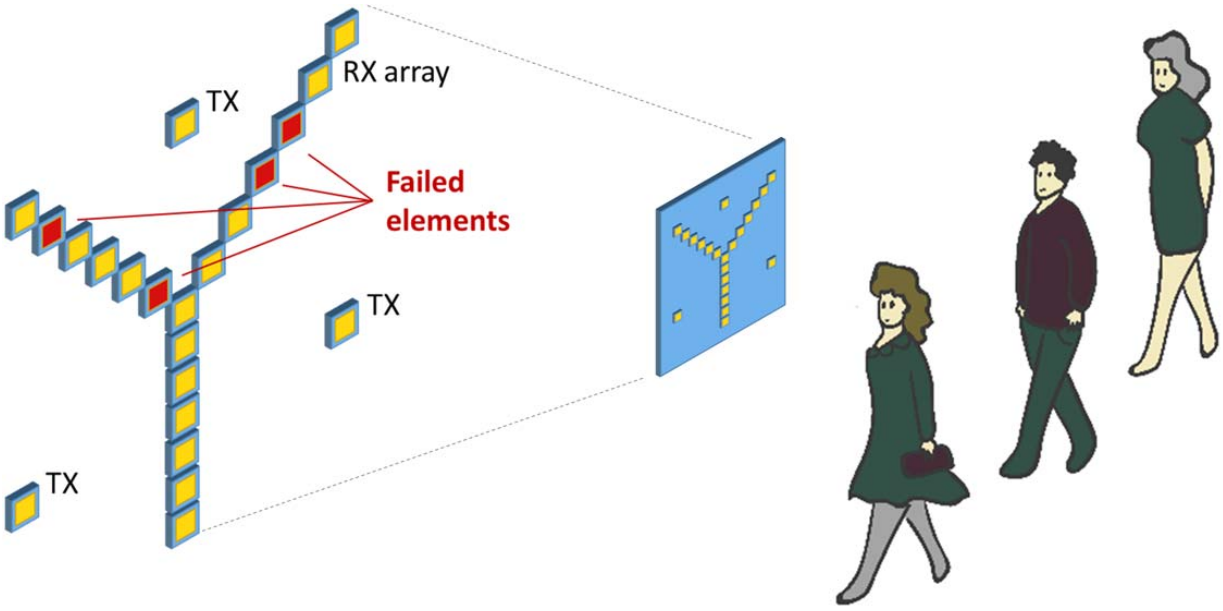

Figure 3.23: Example of a standoff screening application for the active incoherent microwave imaging array. The effect of failures in the receiver must be analyzed to ensure robust imaging operation. Image [9] © 2021 IEEE.

arrays produced the best image reconstruction in most cases, two-dimensional minimum redundancy arrays are an ongoing research area, and standard array designs are not common due to the significantly large solution space associated with such arrays. Nevertheless, the results presented here show that random thinning of the array can produce comparable results when the sparsity is high (above 75%). In two-dimensional systems such thinning is more than feasible and requires less computational design than minimum redundancy arrays.

3.9 Analysis of Element Failures in Active Incoherent Imaging Arrays

From the discussion in the previous section, it is challenging to find minimally-redundant two-dimensional array designs where baselines are not repeated [37]. Furthermore, while sparsity seems like the obvious choice [69], adding some redundancy can increase the robustness of the

© 2019 IEEE. Section 3.9 is adapted with modifications, with permission, from "S. Vakalis and J. A. Nanzer, "Analysis of Element Failures in Active Incoherent Microwave Imaging Arrays Using Noise Signals," in IEEE Microwave and Wireless Components Letters, vol. 29, no. 2, pp. 161-163, Feb. 2019".

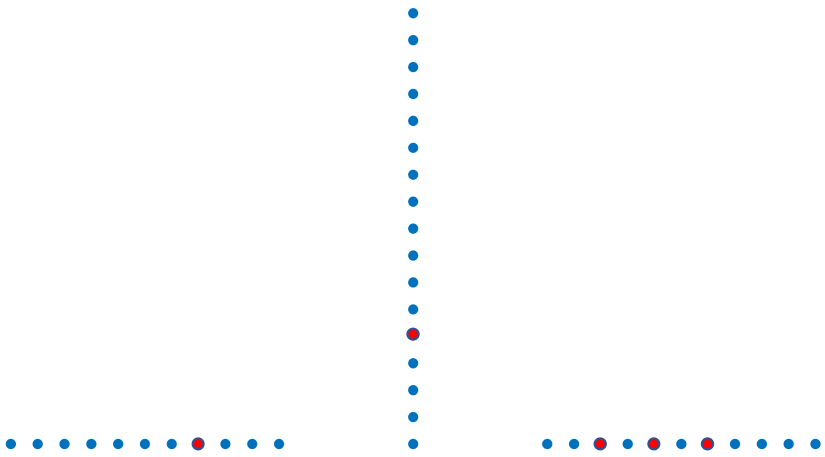

Figure 3.24: Example of a synthesized inverse T-shaped array locations with 5 failed elements (shown with red). Image [9] © 2021 IEEE.

system, in addition to making calibration easier [70]. As a result, images tend to degrade gracefully in the presence of element failures, rather than losing pixels, or, in the case of single-element mechanically-scanned imagers, failing outright. The analysis in this section is focused on failures due to the absence of elements, representing catastrophic element failures. It is noted that failures where the individual elements inject random signals or noise in addition to the received signals should result in less degradation, due to the fact that the received signals are cross-correlated pair-wise, filtering out signals uncorrelated between the receivers. The resulting image degradation therefore will be no greater than if the signals were absent. This can happen when either a cable has been torn off, an amplifier or a mixer breaks down or an antenna element was removed from its place, either intentionally or by accident. Modeled results were calculated using MATLAB, by randomly removing element locations from both simulations and experimental measurements. The metric used to evaluate imaging performance is the RMSE between the reconstructed image from the full 39-element T-array and the reconstructed image from the T-array with failed elements in section 3.7.

Measurements were conducted using the synthesized inverse T-array, at a carrier frequency of 5.85 GHz, in the same setting as section 3.7. A synthesized array with 5 failures is shown in Fig.

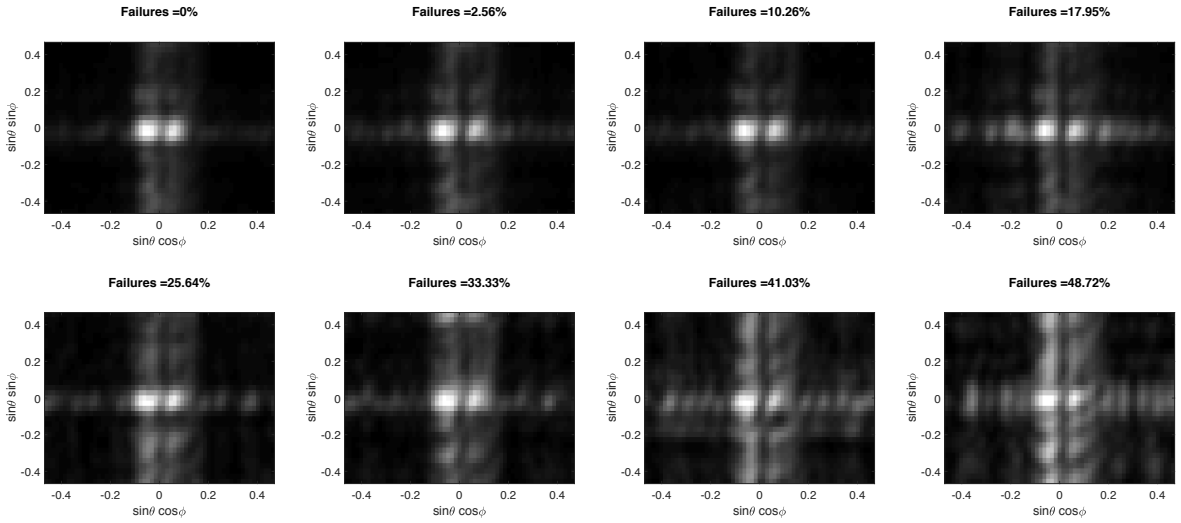

Figure 3.25: Experimental image reconstructions from the T-array corresponding to the percentage of failed elements (elements were removed at random). The horizontal and vertical axes show the direction cosines in the azimuth and elevation planes. Brighter image areas represent larger values of reconstructed intensity. Image [9] © 2021 IEEE.

3.24, where some short baselines are missing due to the horn antennas' dimensions.

The reconstructed images from the T-array were generated for various random instances of failed elements, which were obtained by randomly removing data from measurements. The two-dimensional image reconstruction, shown in Fig. 3.25, is good for failures up to 17.95%, clearly showing the larger reflecting sphere on the left side of the image and the smaller sphere on the right. As the failures increase to 25.64% and greater, the image quality becomes significantly degraded, making it difficult to determine the number of targets.

3.9.1 Prediction of Image RMSE Using Modeling

By simulating failures as missing elements in an array, it is possible to predict how the images will degrade in terms of RMSE as a function of failed elements. A first set of simulations was obtained by calculating the PSF of the array with randomly removed elements and finding the average sidelobe level of the PSF using 1000 Monte-Carlo simulations. The average sidelobe level of the PSF (in dB) is approximately a linear increasing function of the percentage of failed elements, as seen

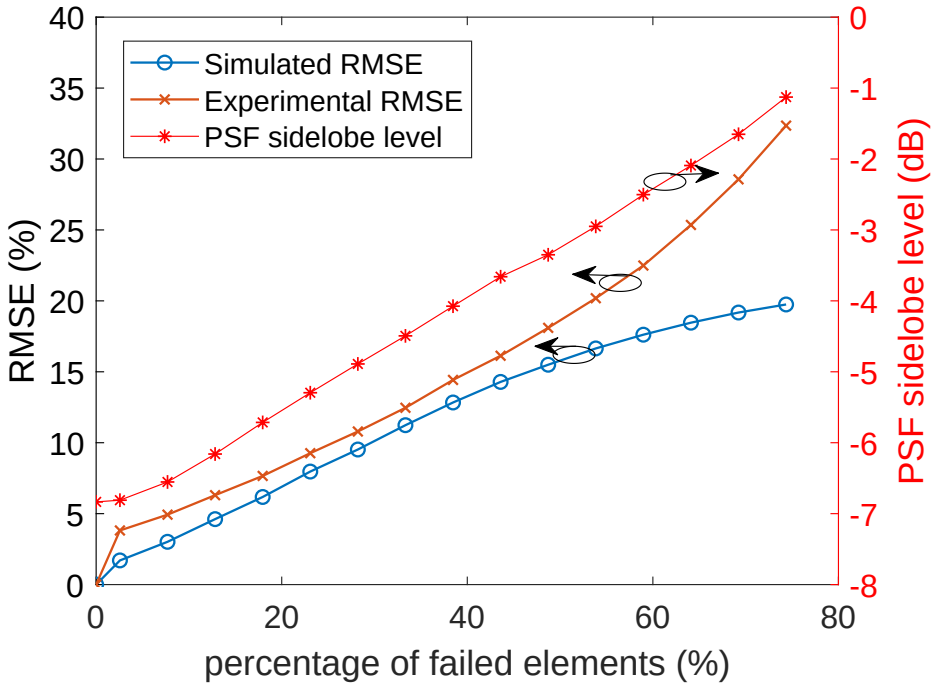

Figure 3.26: RMSE for percentage of element failures, on a 39 element array using experimental and simulated results (Left). Sidelobe level of the PSF for percentage of element failures (Right). Image [9] © 2021 IEEE.

in Fig. 3.26 (Right). A second set of simulations was obtained by calculating the Fourier transform of a two-dimensional scene consisting of two point targets corresponding to the two spheres in the measured data. To assess the degradation of the image quality, elements were randomly removed from the receiving array, and the sampling function S was calculated. The sampled visibility was obtained by multiplying the resulting degraded sampling function by the modeled scene visibility, following which the reconstructed image was generated using an inverse two-dimensional Fourier transform. The RMSE was calculated between the degraded reconstructed image and the original image formed using all elements in the array. Both simulated results were generated from an array matching the measurement system.

A scene consisting of two reflecting point targets was modeled, and Monte-Carlo simulations were conducted using 1000 repetitions for each distinct number of failures. The average values of the RMSE were then calculated and can be seen in Fig. 3.26. The RMSE increases consistently

as element failures start to increase, which is expected. To evaluate the ability to predict measured image degradation, an evaluation of the measured data obtained from the 5.85 GHz system was compared by performing a 1000-repetition Monte Carlo simulation, the average value of RMSE can be seen in Fig. 3.26 (Left). In each iteration, data from a number of elements was randomly removed from the processing. The simulated RMSE aligns well with the measured RMSE for failures rates up to 50%; in this region, the error between predicted and measured RMSE is below 3%. This small difference can be attributed to the ideal nature of the simulations, which do not capture all the noise contributions of the experimental system. Both simulated and experimental RMSE show similar behavior with the PSF sidelobe level. The RMSE of the image degrades by less than 10% for failure rates extending up to 25%.

Active incoherent microwave imaging is quite tolerant to element failures, where feasible image reconstruction is possible with significant element failures. Both experimental and simulated results show potential for medical and security applications that demand robust imaging operation. Furthermore, simple Fourier and spatial-domain modeling can serve as a good prediction method for determining image degradation, which may be used in the design of other array formations.

CHAPTER 4

HIGH-SPEED MILLIMETER-WAVE IMAGING USING ACTIVE INCOHERENT DIGITAL ANTENNA ARRAYS

4.1 Synthesized Millimeter-Wave Measurements

As it was discussed in chapter 3, interferometric imaging can be successfully combined with a noise transmitting array and microwave image reconstruction can be achieved without the high sensitivity requirements of passive interferometric imagers. What also became evident was that the systems in the microwave band had large physical dimensions and their resolution was coarse compared to what is needed for applications like contraband detection or non-destructive testing. Increasing the frequency from microwave to millimeter-wave can significantly improve the system resolution and reduce the size and weight of the system. In this chapter, I will be discussing synthesized millimeter-wave measurements of active incoherent imaging at 40 GHz and then present design considerations and system design of two active incoherent millimeter-wave imaging arrays. The first design is a 16-element 37 GHz array and the second design is a 24-element 38 GHz antenna array. Both arrays are element-level digital, which means that every antenna element response in the antenna array is digitized and can be used for digital signal processing. For the first array I discuss a way to calibrate it and then include experimental measurements. For the second design, I include experimental measurements along with high-speed millimeter-wave imagery.

The schematic of the experimental configuration can be seen in Fig. 4.1. Three transmitters were used but only one is included in the figure. Each transmitter, shown in the top, utilized a 0.2–2000 MHz low-cost noise source at baseband. These analog noise sources had a much stronger response close to dc than in the rest of the band. In order to avoid damaging and saturating components and realize a flat noise response over the band of interest, a high pass filter was utilized after each noise source. The cutoff frequency of the filter was 20 MHz. Afterwards the baseband noise signal was boosted by a low-cost baseband amplifier of 30 dB gain and subsequently it was

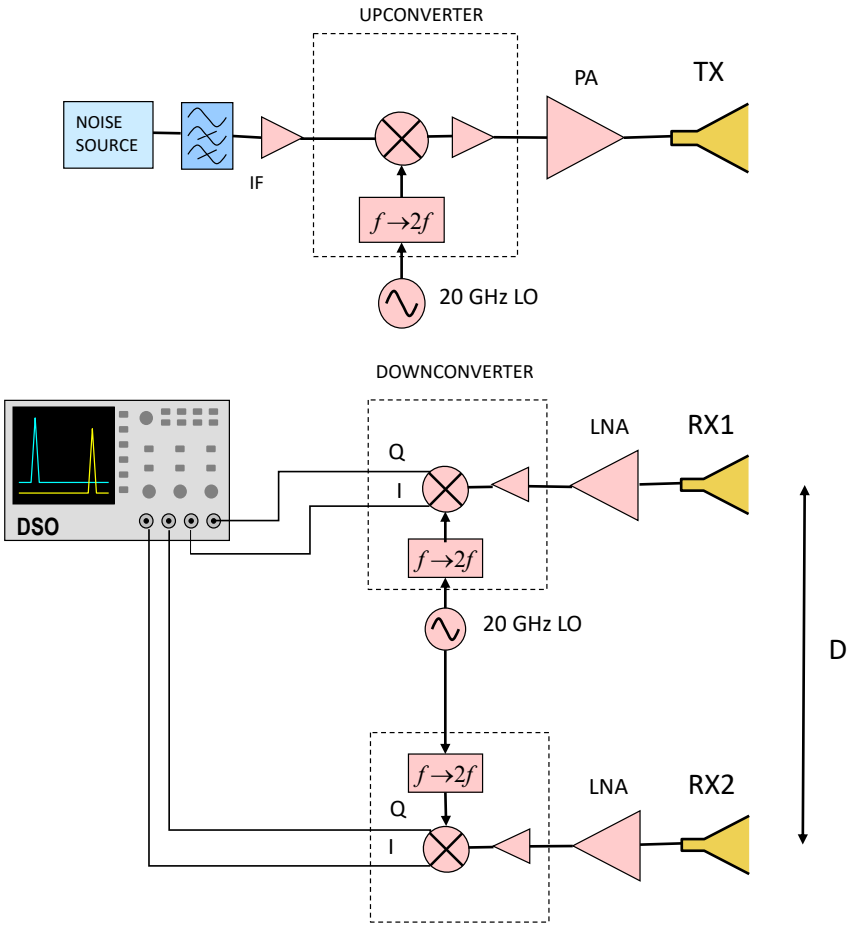

Figure 4.1: Schematic of the experimental configuration used in this work. The transmitter consisted of three noise sources upconverted to 40 GHz (only one shown in the figure), while the receiver consisted of two elements downconverted to baseband and captured using an oscilloscope. Image [10] © 2021 IEEE.

fed into the IF port of an ADI HMC6787A quadrature upconverter. The upconverters include an integrated frequency doubler for the local oscillator (LO) which was used to mix the baseband noise to 40 GHz with an LO of 20 GHz. Each 40 GHz noise signal was then amplified by an ADI HMC7229 power amplifier, achieving a maximum of -10 dBm of noise power at 40 GHz and approximately 6 dBm of noise power in total when integrated over the whole band. Each transmitter was connected to a 10-dBi Ka-band (26.5–40 GHz) standard gain horn antenna.

For the receivers, the reflected noise from the scene is captured by two 15-dBi Ka-band standard gain horn antennas and was amplified with 20 dB gain ADI HMC1040 low-noise amplifiers

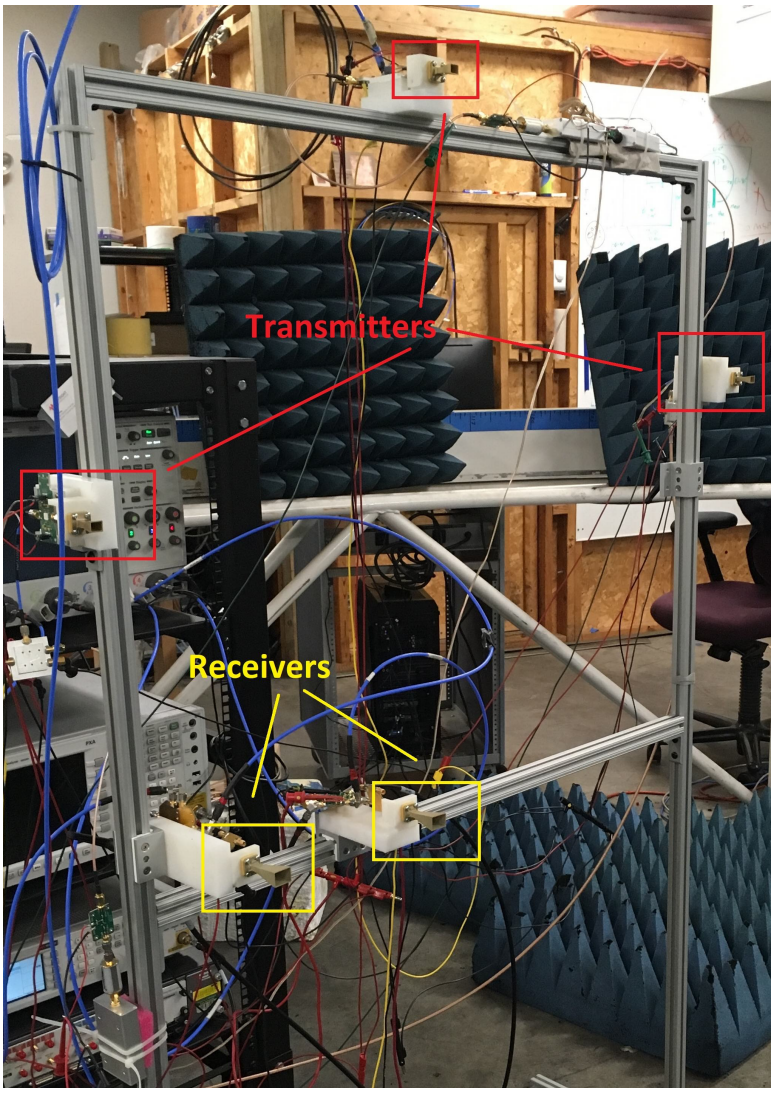

Figure 4.2: Photograph of the 40 GHz experimental measurement configuration with three noise transmitters (red) and two receivers (yellow). All components are properly biased and mounted using 3D printed brackets. The two-dimensional array locations were synthesized by moving the receivers in the vertical and horizontal directions. The transmitters were fixed. Image [10] © 2021 IEEE.

with a noise figure of approximately 2 dB. The millimeter-wave signal was then downconverted to baseband using two ADI HMC6789 quadrature downconverters and a 20 GHz LO. All the components were properly biased and mounted into an aluminum rack with 3-D printed holding structures. A photograph of the rack with all the components can be seen in Fig. 4.2. The received noise signals were captured and digitized using a 20 GHz Keysight MSOX92004A oscilloscope

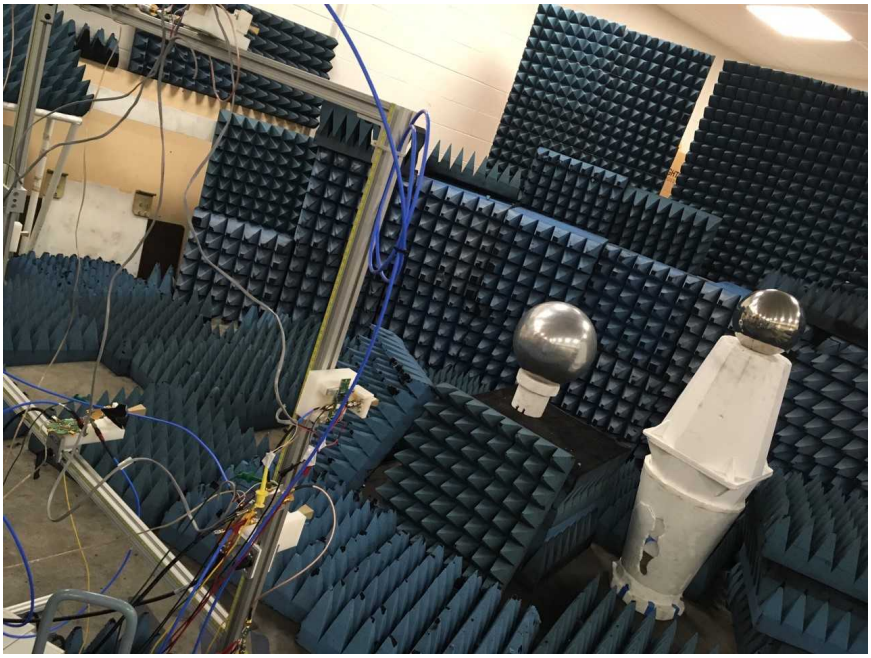

Figure 4.3: The two spherical targets that were used for the two-dimensional experimental measurements. Both the array and the targets were located inside a semi-anechoic environment. Image [10] © 2021 IEEE.

at 2.5 GSamples/s in high-resolution mode. The waveforms were saved and processed offline in MATLAB.

Two spherical targets were used as the two-dimensional scene, which are shown in Fig. 4.3. The targets were placed inside a semi-anechoic range and were located at a distance of 2.5 m from the array. The horizontal and vertical separation between the spheres was equal with 70 cm and 50 cm, respectively. The synthesized array locations had a maximum horizontal and vertical dimension of $66\,\lambda$ and $46\,\lambda$, respectively. The synthesized array was an inverse T-array, which can be utilized easily by moving one antenna horizontally and the other vertically, and can be seen in Fig. 4.4. The spacing between each element was $2\,\lambda$. The reconstructed image from the synthesized measurements can be seen in Fig. 4.5. Both the spheres can be clearly distinguished. The smaller of the two spheres exhibits a response near the top right of the reconstructed image while the larger sphere shows a wider response on the lower left with higher intensity, which can be expected due to its larger radar cross section. Due to the antenna and mounting structure dimensions,

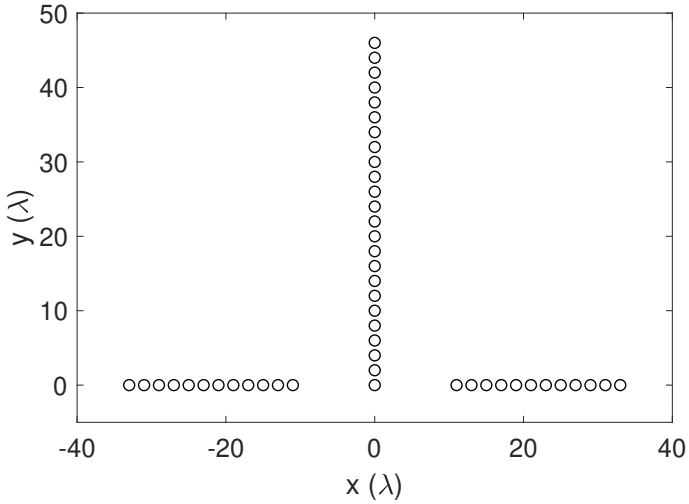

Figure 4.4: Synthesized element locations for the two-dimensional imaging setup presented in this section. Two receive antennas were used and moved sequentially until all antenna pairs were represented in the measurement, in 2 λ increments. Image [10] © 2021 IEEE.

the narrow baselines are missing from the synthesized measurements, which is manifesting in the image as sidelobe structure. The sidelobe effect can be mitigated by using antennas with smaller dimensions, different mounts and feeding structures.

The measurements in this section represent the first ever experimental demonstration of active interferometric imaging using noise transmitters at millimeter-wave frequencies. Building on them, in the next section millimeter-wave array designs and full system concerns are going to be discussed.

4.2 16-element Active Incoherent Imaging Array

The limitation with synthesized measurements is the very long data acquisition time, due to mechanically moving antennas in space to synthesize an antenna baseline pair. Interferometry can utilize the pairwise combinations in a sparse array and provide fast data acquisition, where all the

© 2020 IEEE. Sections 4.2 and 4.3 are adapted with modifications, with permission, from "S. Vakalis, L. Gong, Y. He, J. Papapolymerou and J. A. Nanzer, "Experimental Demonstration and Calibration of a 16-Element Active Incoherent Millimeter-Wave Imaging Array," in IEEE Transactions on Microwave Theory and Techniques, vol. 68, no. 9, pp. 3804-3813, Sep. 2020".

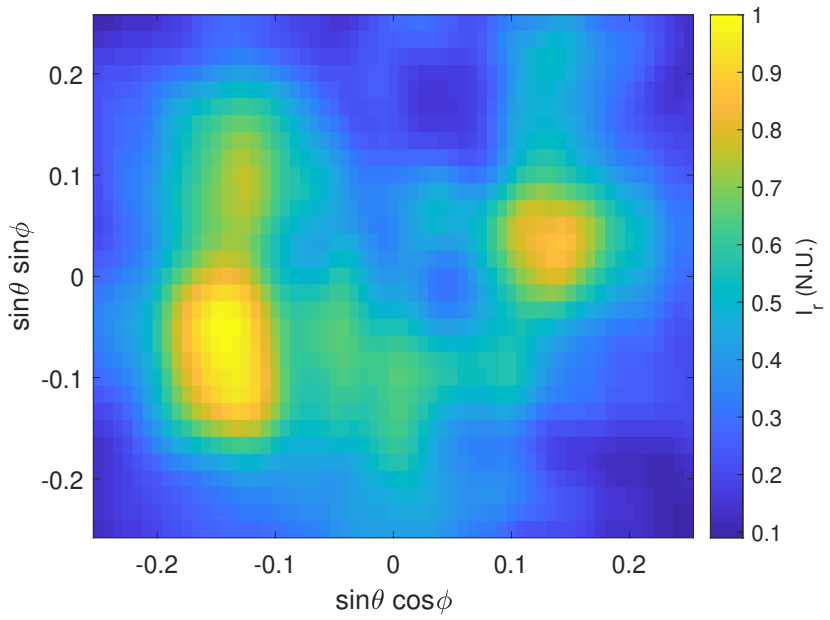

Figure 4.5: Experimental image reconstruction of the two spherical targets in Fig. 4.3. The amplitude is normalized, and hence the colorbar axis is in normalized units (N.U.). Image [10] © 2021 IEEE.

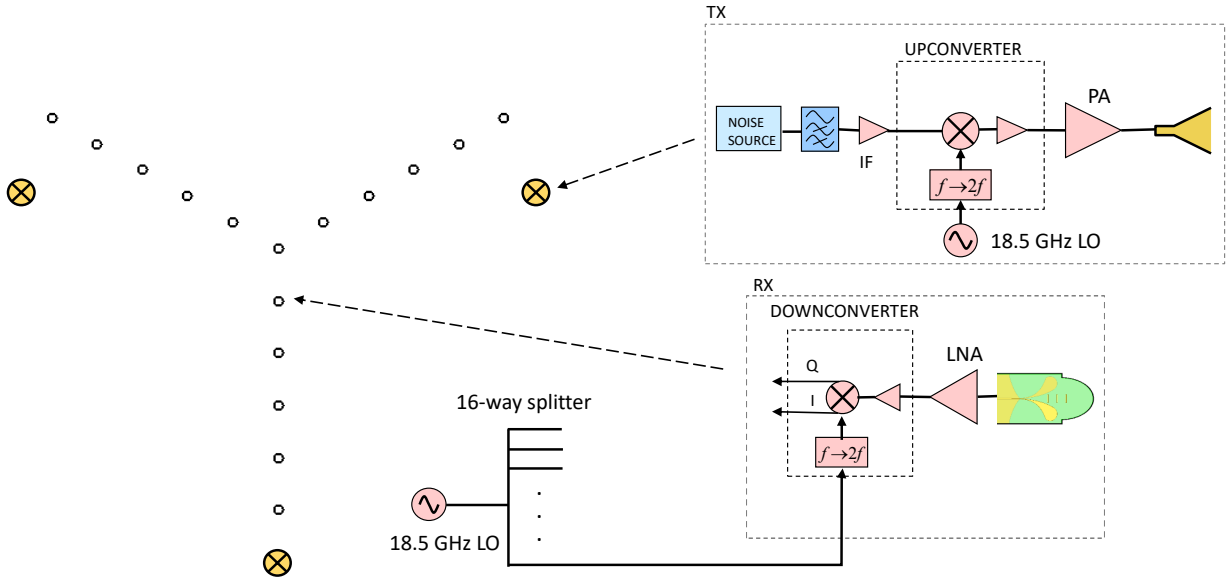

Figure 4.6: Active incoherent imaging array with 16 elements in Y-array formation. The 16 receivers are represented by white circles and the three transmitters which are used to illuminated the scene are represented by the yellow circles with the crosses. Image [11] © 2021 IEEE.

antenna elements in the array capture information associated with the whole scene at the same time. In this section, I will present the design and build of a sparse 16-element Y-shaped array. The novel contributions of this work include the use of incoherent noise illumination with no synchronization needed between transmit and receive and the use of low-cost components fabricated inside the university or purchased off-the-shelf.

4.2.1 16-Element Incoherent Array System Design

A block diagram of the 37 GHz array configuration can be seen in Fig. 4.6. The three transmitters are represented by the yellow circles with crosses, and the 16 receivers in Y-array formation are represented by white circles. The receive array has three arms and is designed such that the angle between every two arms of the Y-array is 120°. This particular formation was used because of its dense sampling function properties and wide field of view, due to hexagonal sampling [71]. Additionally, this particular design employs a lot of redundant baselines, which can be used for calibration, and will be discussed in the next section.

The receive array minimum spacing between neighboring antenna elements was 24 mm (2.96 λ). The three noise transmitters utilized 0.2–2000 MHz low-cost baseband noise sources which were upconverted to 37 GHz using ADI HMC6787 I/Q upconverters with integrated frequency doubler. An LO of 18.5 GHz was used for the upconversion. The incoherent millimeter-wave noise signals were then furthermore amplified by ADI HMC7229 power amplifiers, achieving approximately 0 dBm total power at 37 GHz over a bandwidth of 50 MHz.

Every one of the 16 receivers utilized a 9 dBi printed Vivaldi antenna. Measurements of the 16 antennas' S_{11} in a Vector Network Analyzer gave an average S_{11} of -15 dB at 37 GHz. The signal after the antenna was then amplified by a 20 dB gain ADI HMC1040 LNA before being downconverted to baseband using an ADI HMC6789 MMIC I/Q downconverter. The LNAs were connected directly to the end-launch male connectors of the antennas in order to keep the SNR as high as possible. The LNA outputs were afterwards fed to the downconverters using 45.7 cm long cables. The downconverted signals were captured using two 16-channel ATS9416 14-bit,

100 MSamples/s, AlazarTech waveform digitizers installed on a computer in master-slave mode. The sampling rate used by the waveform digitizers was 100 MSamples/s and the total capture time was 20 μs. The received signal bandwidth can be estimated to be equal with 50 MHz, which is the first Nyquist zone for 100 MSamples/s sampling rate, although there are noise components that are subsampled from highest Nyquist zones. This is not an issue for the active incoherent imaging approach, as perfect knowledge of the transmit illumination is not required. Both signal processing and image reconstruction took place in MATLAB.

A photograph of the incoherent imaging array is shown in Fig. 4.7. The Vivaldi antennas were fabricated on a 2 mil Liquid Crystal Polymer (LCP) substrate [72]. Vivaldi antennas were chosen for this array design due to their lower cost compared to waveguide antennas such as horn antennas, and their compact and planar profile, which can help to minimize intra-element distance in the interferometric array design which can allow for larger field of view. At the same time Vivaldi antennas offer high directivity, which can supress reflections outside the unambiguous field of view, and at the same time increase the receive SNR. LCP substrate is a good choice for millimeter-wave antenna due to its its low-loss and flexibility [73].

The LO signal was splitted 16-ways using two 8-way Mini-Circuits ZN8PD-02183-S+ power splitters for downconverting the signals from the 16 receivers. A 3D-printed mount was used to support and hold the receive array elements in the correct locations. The Y-shaped 3D printed structure extends by 26 cm and 21 cm, in the horizontal and vertical dimensions, respectively. The three transmitters were separated at a slightly larger separation than the largest antenna baseline in order ensure that we are operating at a sufficiently spatially incoherent zone, compared to the receive array resolution, as it was shown in chapter 3. No particular knowledge of the transmit radiation is needed in general for active incoherent millimeter-wave imaging systems, and therefore there is significant freedom in the transmitter design and placement.

A calculation of the ideal PSF of the Y-array is shown in Fig. 4.8, which exhibits sidelobes in the edges of the field of view due to intra-element spacings greater than $\frac{\lambda}{2}$. The sidelobes can be mitigated by performing multiplication of the reconstructed intensity with a circular window mask

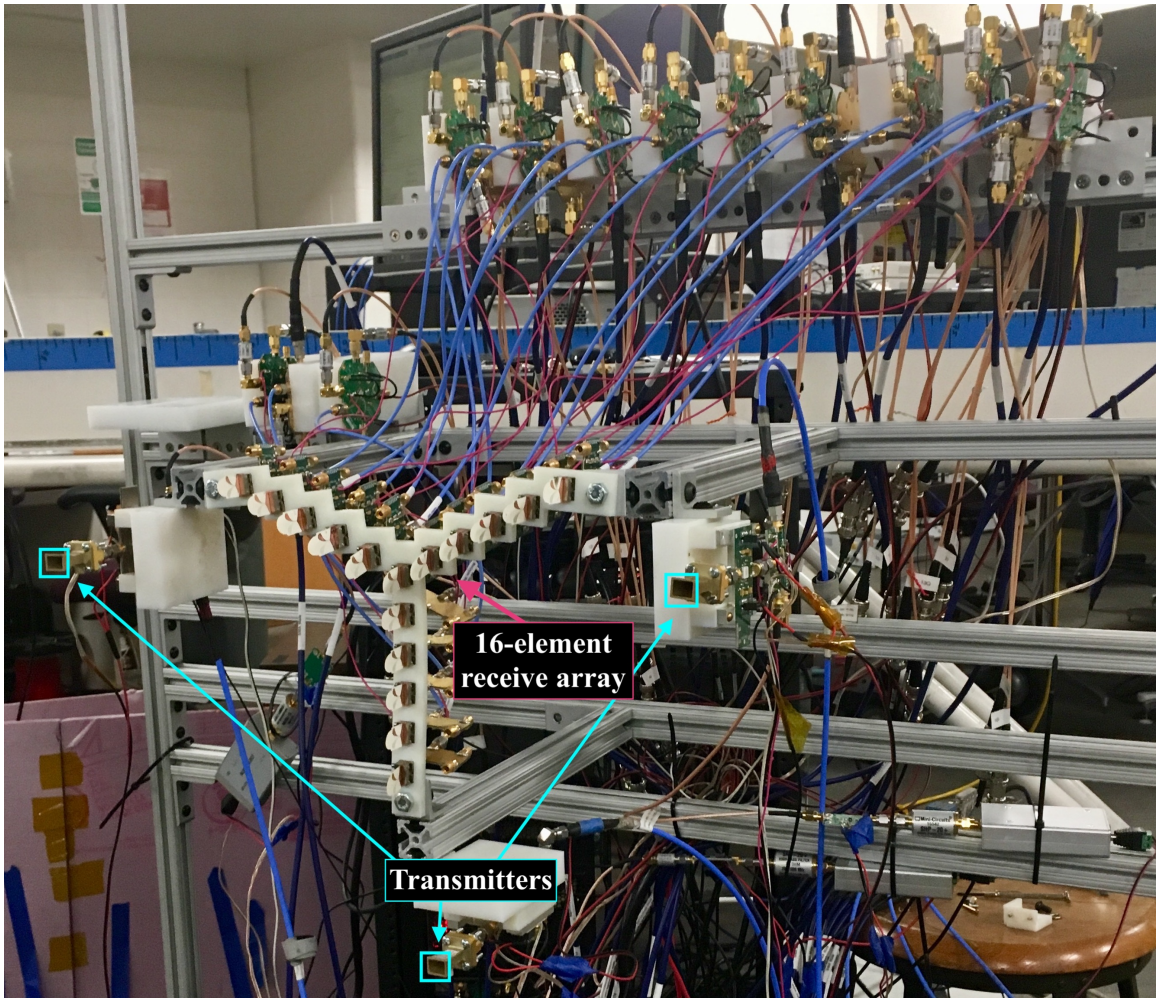

Figure 4.7: Photograph of the 16-element active incoherent imager. The three incoherent noise transmitters are shown with blue, and the 16-element receive array is shown with pink. The transmitters are separated at a larger spacing than the receive array. Image [11] © 2021 IEEE.

to filter out the unwanted responses on the edges of the image [71,74]. Furthermore, using directive antenna elements, which are focusing near broadside, can help suppress the unwanted interference from outside the unambiguous field of view. And while individual antenna performance and radiation can affect the shape of the PSF and image reconstruction, using directive antennas can in generally help with approximating the antenna radiation pattern to be uniform across the narrower field of view for the bandwidth used for image reconstruction. Each antenna imperfection will be modelled as an amplitude and phase for the narrow field of view and narrow receiver bandwidth and I will discuss a way to calibrate the array in section 4.3. The 3-dB resolution of the imager can

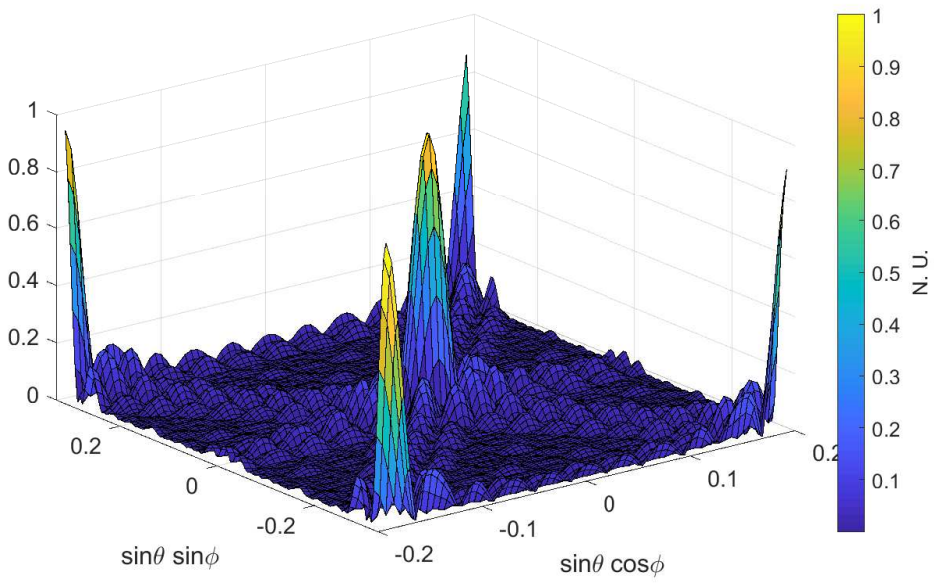

Figure 4.8: Ideal PSF calculation for the 16-element Y-array. There are sidelobes present at the edges of the field of view, which is expected from a Y-array and this can be countered by means of spatial windowing and antenna focusing. Image [11] © 2021 IEEE.

be found to be 1.78° and 2.22° in the azimuth and elevation planes respectively. The unambiguous field of view due to the intra-element array spacings was 22° and 38° in the azimuth and elevation planes, respectively.

4.3 Calibration Using Redundant Baselines

Using in-house fabricated and off-the-shelf components can significantly reduce the system cost compared to using expensive waveguide components or accurately calibrated customized parts. Nevertheless, this increases the susceptibility of the system to uncertainties and disparities in hardware performance. Interferometric processing is phase-based so it is resistant to small amplitude differences between antenna elements and receiver noise. However, interferometry can be sensitive to phase variations between antenna elements and phase variations between the quadrature receive channels of the same antenna. At millimeter-wave frequencies, variations in the length of components can be a significant fraction of the wavelength, and result in a non-negligible phase error. The in-house fabricated antennas had variation in their performance, along with the off-the-shelf

components. Also, the 18.5 GHz LO was split using two commercial 8-way power splitters, which were afterwards followed by 16 flexible cables. The cable bending before feeding the LO signal in the downconverters significantly affected performance.

For the transmitters, the calibration requirements are significantly more relaxed, which is one of the benefits of active incoherent millimeter-wave imaging. The transmitters do not need to be phase locked or phase calibrated, because they need to be incoherent and transmit independent signals in order to support interferometric image formation as discussed in chapter 3. Large power disparities on the transmitters can cause issues because this could effectively mean that only one or two transmitters would dominate the illuminating signal, impacting the spatial incoherence of the radiation. The noise sources used in this array had significant power variations, therefore coaxial attenuators were used to balance their output at 37 GHz. After the attenuation, all transmitters were transmitting approximately the same power with variations smaller than 0.5 dB.

There are a plethora of techniques for calibration of interferometric antenna arrays in radio astronomy and remote sensing in the literature [75]. Many of these techniques rely on some partial knowledge or an accurate model of the scene that needs to be reconstructed. In order to achieve calibration of the array without any prior information or model of the scene, a calibration technique was implemented using the redundant baseline spacings in the Y-array. This particular calibration method has been investigated before in radio astronomy arrays, however it was found to be performing inadequately in low SNR values, which can result in significant estimation biases [70]. This might be a limitation for passive interferometric arrays that observe the thermally generated electromagnetic signals from the stars and other galactic objects, or for a passive millimeter-wave imager when capturing the thermal signals from a human. The array presented in this section is an active system with signal transmission, which means that a high SNR can be easily realized by controlling the transmit power which can make the calibration biases minimal.

For an interferometric array with total number of elements equal with N, the redundant baseline calibration can be described with the following [59]: consider the lth antenna element of the array,

where

$$1 \leq l \leq N, \tag{4.1}$$

as shown in the bottom right of Fig. 4.6, to be represented by a complex gain G_l. The cross-correlation between the measured responses of the lth and mth elements is corresponding to the visibility sample V_{lm}^{meas} which can be written as

$$V_{lm}^{meas} = V_{lm}^{true} G_l G_m^* + c_{lm} \tag{4.2}$$

where $(\cdot)^*$ represents the complex conjugate, V_{lm}^{true} is the true visibility information the interferometric baseline should theoretically capture, and c_{lm} is an additive term that can be used to summarize the effects of undesired noise, errors, and other biases in the measurement. In general for passive systems that capture thermal signals, it is not always feasible to neglect the c_{lm} quantity, but for an active system with high enough SNR it can be assumed that

$$V_{lm}^{true} G_l G_m^* \gg c_{lm}. \tag{4.3}$$

As a result, (4.2) can be approximated as

$$V_{lm}^{meas} = V_{lm}^{true} G_l G_m^*. \tag{4.4}$$

In (4.4), V_{lm}^{meas} represents the only known quantities, and the true visibility samples V_{lm}^{true} and the complex gains of each receiver G_l, G_m are the unknowns. The procedure that will be decribed next solves for both the true visibility samples and complex gains of the receivers, however for this work only the complex gains are needed for the system calibration, while the true visibility samples are needed for image reconstruction and estimation. After the calibration takes place, each antenna element will be matched to a complex gain, and calibration can take place at the same time with the image reconstruction with no delay.

By writing the visibility and gains in complex form $V^{meas} = e^{(v+j\psi)}$ and $G = e^{(g+j\phi)}$, and taking the natural logarithm of (4.4), the gains and the phases can be decoupled and give us two separate system of quations as follows:

$$v_{lm}^{meas} = v_{lm}^{true} + g_l + g_m \tag{4.5}$$

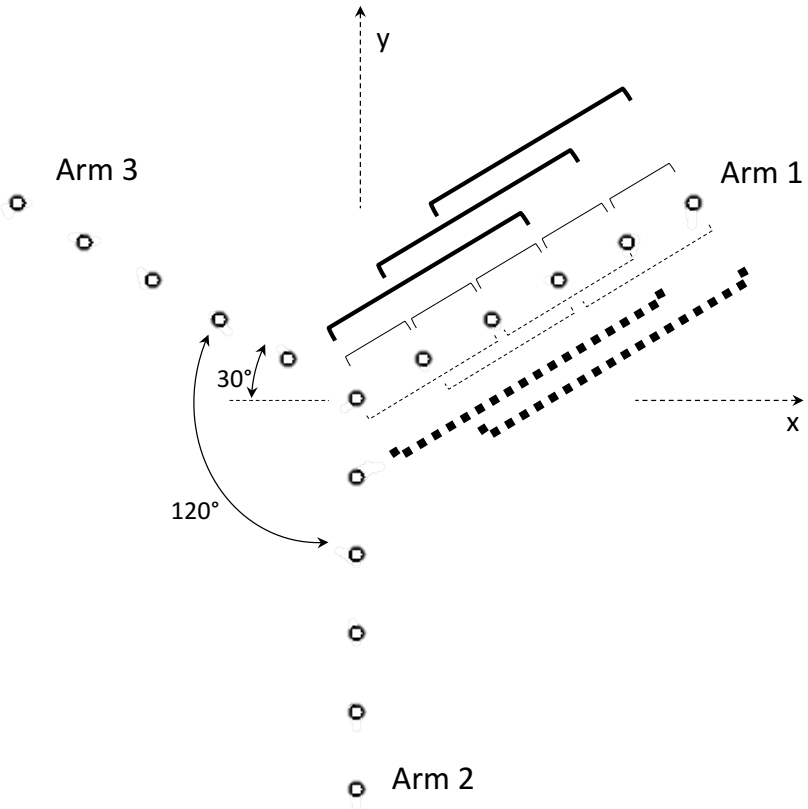

Figure 4.9: Y-shaped array locations and redundant baselines on it. Same style line represents redundant baseline pairs of the same spacing. Image [11] © 2021 IEEE.

$$\psi_{lm}^{meas} = \psi_{lm}^{true} + \phi_l - \phi_m \tag{4.6}$$

Phase unwrapping must take place in (4.6) in order to achieve the correct result. The following constraints must be added in order to avoid the systems of (4.5) and (4.6) becoming ill-posed:

$$\sum_l g_l = 0 \tag{4.7}$$

$$\sum_l \phi_l = 0 \tag{4.8}$$

One more constraint for the phases is needed in order to take into account the array geometry, which is given by

$$\sum_l r_{x,l}\phi_l = 0 \tag{4.9}$$

$$\sum_l r_{y,l}\phi_l = 0 \tag{4.10}$$

where $\mathbf{r}_l = (r_{x,l}, r_{y,l})$ is the actual location of the lth antenna element. Afterwards, the redundant baselines of the array need to be identified. In order for two antenna baselines to capture the same visibility samples, they need to have the same vertical and horizontal spacing.

Examples of redundant baselines can be seen in Fig. 4.9, where the redundant baseline pairs are represented with the same line style and should capture the same visibility sample. Using this information, the measurements from the matching redundant baselines can be utilized to calculate the complex gains of each receiver. Although Fig. 4.9 shows only the redundant baselines in arm 1 of the Y-shaped array, the same redundancy can be found in arms 2 and 3 of the array, and therefore all receive antenna elements can be calibrated based on the redundant baselines in each arm. Using indexes from 1 to 6 to number the antennas in arm 1, and starting from the top right of the figure, it can be deduced that

$$V_{12}^{true} = V_{23}^{true} = V_{34}^{true} = V_{45}^{true} = V_{56}^{true} = V_{1}^{true} \tag{4.11}$$

$$V_{13}^{true} = V_{24}^{true} = V_{35}^{true} = V_{46}^{true} = V_{2}^{true}, ... \tag{4.12}$$

until all redundant baseline spacings are taken into account, where the single subscript notes the difference in the relative positions of the antennas. The phase equations from (4.6) can thus be written as

$$\begin{pmatrix} 1 & -1 & 0 & 0 & 0 & 0 & 1 & 0 & 0 & 0 & 0 \\ 1 & 0 & -1 & 0 & 0 & 0 & 0 & 1 & 0 & 0 & 0 \\ 1 & 0 & 0 & -1 & 0 & 0 & 0 & 0 & 1 & 0 & 0 \\ 1 & 0 & 0 & 0 & -1 & 0 & 0 & 0 & 0 & 1 & 0 \\ 1 & 0 & 0 & 0 & 0 & -1 & 0 & 0 & 0 & 0 & 1 \\ 0 & 1 & -1 & 0 & 0 & 0 & 1 & 0 & 0 & 0 & 0 \\ 0 & 1 & 0 & -1 & 0 & 0 & 0 & 1 & 0 & 0 & 0 \\ 0 & 1 & 0 & 0 & -1 & 0 & 0 & 0 & 1 & 0 & 0 \\ 0 & 1 & 0 & 0 & 0 & -1 & 0 & 0 & 0 & 1 & 0 \\ 0 & 0 & 1 & -1 & 0 & 0 & 1 & 0 & 0 & 0 & 0 \\ 0 & 0 & 1 & 0 & -1 & 0 & 0 & 1 & 0 & 0 & 0 \\ 0 & 0 & 1 & 0 & 0 & -1 & 0 & 0 & 1 & 0 & 0 \\ 0 & 0 & 0 & 1 & -1 & 0 & 1 & 0 & 0 & 0 & 0 \\ 0 & 0 & 0 & 1 & 0 & -1 & 0 & 1 & 0 & 0 & 0 \\ 0 & 0 & 0 & 0 & 1 & -1 & 1 & 0 & 0 & 0 & 0 \\ 1 & 1 & 1 & 1 & 1 & 1 & 0 & 0 & 0 & 0 & 0 \\ 5 & 4 & 3 & 2 & 1 & 0 & 0 & 0 & 0 & 0 & 0 \end{pmatrix} \begin{pmatrix} \phi_1 \\ \phi_2 \\ \phi_3 \\ \phi_4 \\ \phi_5 \\ \phi_6 \\ \psi_1 \\ \psi_2 \\ \psi_3 \\ \psi_4 \\ \psi_5 \end{pmatrix} = \begin{pmatrix} \psi_{12} \\ \psi_{13} \\ \psi_{14} \\ \psi_{15} \\ \psi_{16} \\ \psi_{23} \\ \psi_{24} \\ \psi_{25} \\ \psi_{26} \\ \psi_{34} \\ \psi_{35} \\ \psi_{36} \\ \psi_{45} \\ \psi_{46} \\ \psi_{56} \\ 0 \\ 0 \end{pmatrix} \tag{4.13}$$

The last two rows represent the constraints from (4.8) and from (4.9) and (4.10). Only one row is included for (4.9) and (4.10) because this particular subarray has $r_x = \cos(30^\circ)\cdot[5 \quad 4 \quad 3 \quad 2 \quad 1 \quad 0]$ and $r_y = \sin(30^\circ) \cdot [5 \quad 4 \quad 3 \quad 2 \quad 1 \quad 0]$ and the constants in the front can be simplified since the right hand side is zero.

The least-squares solution of $Ax = b$ is given by $x = (A^T A)^{-1} A^T b$. In order for all the 16 elements of the array to be calibrated, the matrix A should contain all the redundant information in the array for the three arms of the array. The element in the center is part of all three arms so it should be present in the equations for the three arms in order to act as a reference and minimize biases in phase and amplitude between the three arms. The redundant pairs between antenna elements in different arms are not taken into account because they do not provide redundant information in

this particular case, and because the least-square solution includes the true visibility samples and the problem can easily become ill-posed.

Initial simulations of the redundant baselines calibration method were run for the 16-element Y-array when observing a single point source. Each receive element was modeled with non-idealities by a complex gain $G = e^{(g+j\phi)}$. The amplitude variations g were uniformly distributed in the interval [-0.5,0.5], and the phase variations were uniformly distributed in the interval $[0, \pi]$. The uncalibrated point source reconstruction is shown in Fig. 4.10(a). The array observed the visibility of a single point source, but produced a "dirty" beam, a term which was used in radio astronomy to describe when the sidelobe level is much higher than anticipated. The responses at the edges of the image caused by the PSF grating lobes (see Fig. 4.8) were filtered by multiplying the image reconstruction with a Gaussian window. After running the calibration algorithm using the redundancy in the baselines described in this section, the beam became much "cleaner", which can be seen in Fig. 4.10b. The results indicate that in active systems where the SNR is not low, the redundant-baseline calibration approach can be applied even when the array does not have significant redundancy, such as the one presented in this work. In the next section the algorithm will be applied to experimental data to compensate for the variations on the array we discussed in section 4.2. A simple script that can be used for calibrating a linear antenna array can be found in Appendix D.

4.4 Experimental Calibration and Image Reconstruction Results

The first experimental measurements for the calibration to be applied were performed using a 30 dBsm trihedral corner reflector inside a semi-anechoic environment which manifests as a strong point response. In Fig. 4.11(a) the uncalibrated point response can be seen, while the calibrated beam response is shown in In Fig. 4.11(b). The point-like response of the single reflector is clearly reconstructed after the calibration algorithm was applied. A Gaussian window was applied to the image to remove the responses at the corners resulting from the grating lobes in the PSF. The least-squares calibration approach was implemented only once to determine the complex weights

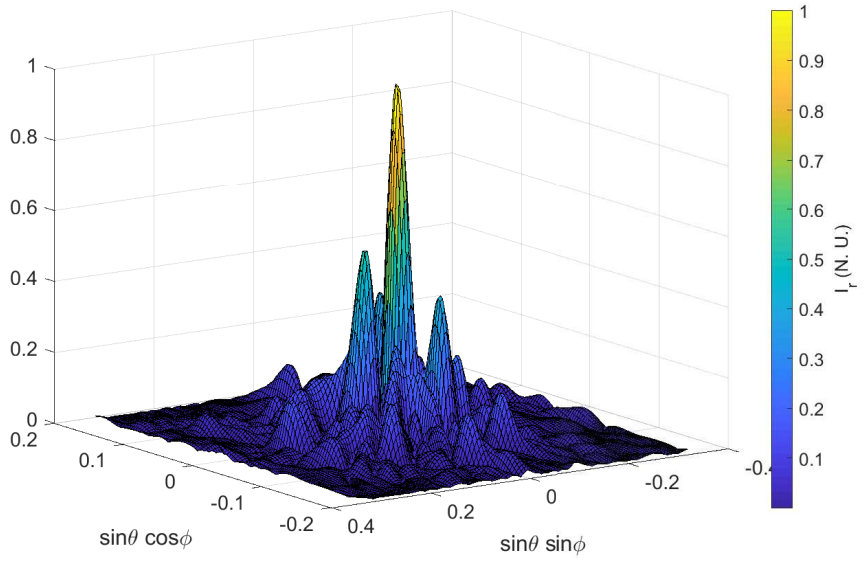

(a)

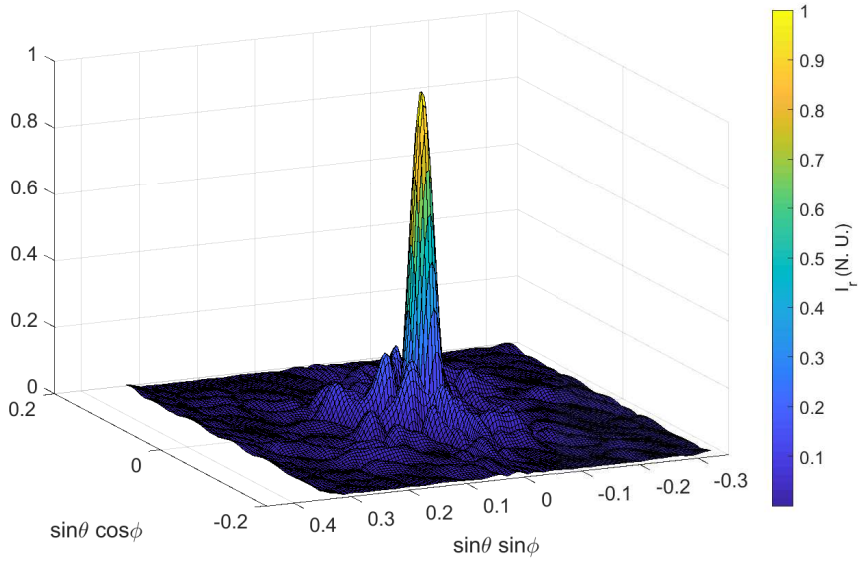

(b)

Figure 4.10: (a) Simulation of a point source reconstruction from a 16-element Y-shaped array with amplitude and phase errors. (b) Simulation of a point source reconstruction after calibrating using the redundant baselines in a 16-element Y-shaped array. Image [11] © 2021 IEEE.

of each channel, after which the image formation procedure was implemented normally.

After calibration took place, additional experimental measurements were taken inside the same semi-anechoic environment of a target made out of two copper stripes glued on a foam board,

shown in Fig. 4.12. The two stripes were made out of copper tape with dimensions of 38 cm by 10 cm, spaced vertically by 22 cm, and glued to the foam substrate. The target was located at a distance of 2.7 m away from the imaging array. This measurement took place in the near-field of the receive array, but when located near broadside of the array, the phase errors are very small relative to the far-field approximation [51, 76]. The raw image reconstruction using the 37 GHz array can be seen in Fig. 4.13(a), showing strong artifacts compared to the actual target shape. The image reconstruction after calibration in Fig. 4.13(b) shows that the spurious responses have been successfully mitigated, resulting in two horizontal responses which match the two copper stripes of the target. The imaging system is capable of differentiating the responses from the two stripes, and achieves cm-level resolution at a distance of 2.7 m. The image reconstructions were furthermore obtained with low computational complexity as they signal processing is composed of vector multiplications and Fourier transforms. Additionally, this system uses low integration time and bandwidth, each roughly an order of magnitude less than what is required passive interferometric imagers which capture thermal signals [3].

4.5 High-Speed Millimeter-Wave Using Active Incoherent Millimeter-Wave Arrays

Interferometric image reconstruction is very fast because it utilizes vector multiplications and Fourier tranforms and every spatial point in the scene emits an independent signal. This means that after the correlation-based processing, the information does not need to be decoded or demultiplexed. In many computational imaging approaches it is required for some spatial coding to take place in the scene and the image reconstruction is usually the solution of an inverse problem. Depending on the matrix dimensions this can become very computationally expensive. In interferometry although there is no need for knowledge of the illumination or coding, every point in the scene should emit or reflect a sufficiently independent signal as a function of time. Active incoherent millimeter-wave imaging utilizes incoherent noise signal transmission in order to illuminate the scene in a spatio-temporally incoherent way and support this requirement. By emitting noise

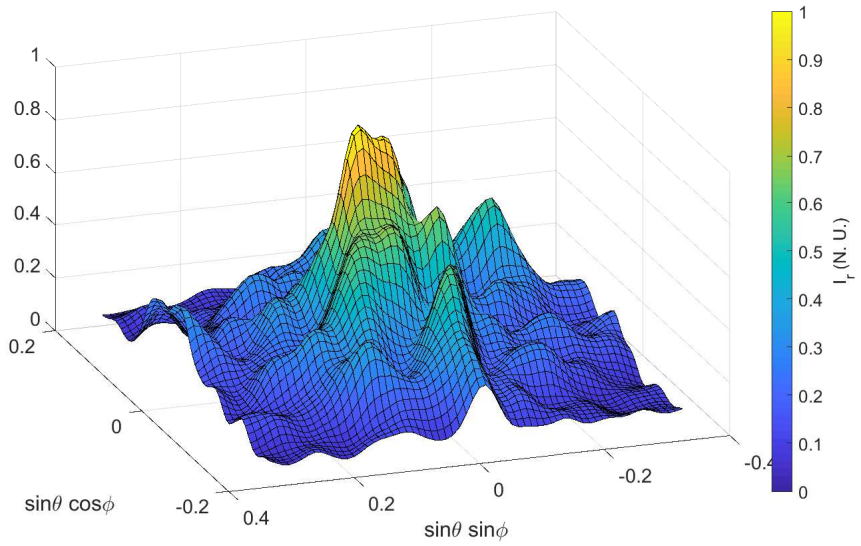

(a)

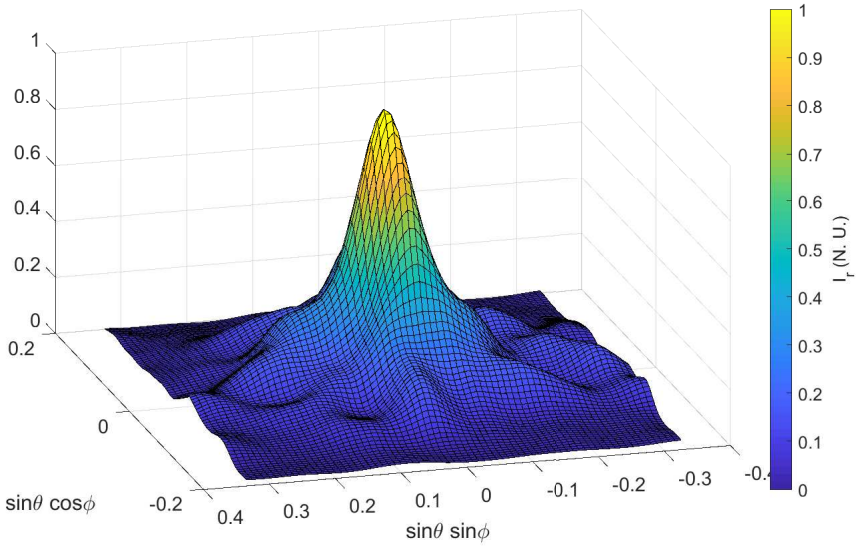

(b)

Figure 4.11: (a) Experimental raw corner reflector reconstruction prior to calibration. There is significant sidelobe level present in the image due to large amplitude and phase variations between the receive elements. (b) Experimental corner reflector reconstruction after calibration using the redundant baselines in the array. The image reconstruction now closely resembles a point source. Image [11] © 2021 IEEE.

from multiple widely separated locations, the spatial scene can be illuminated with little spatial coherence, and fast interferometric image formation based on matrix multiplications and Fourier

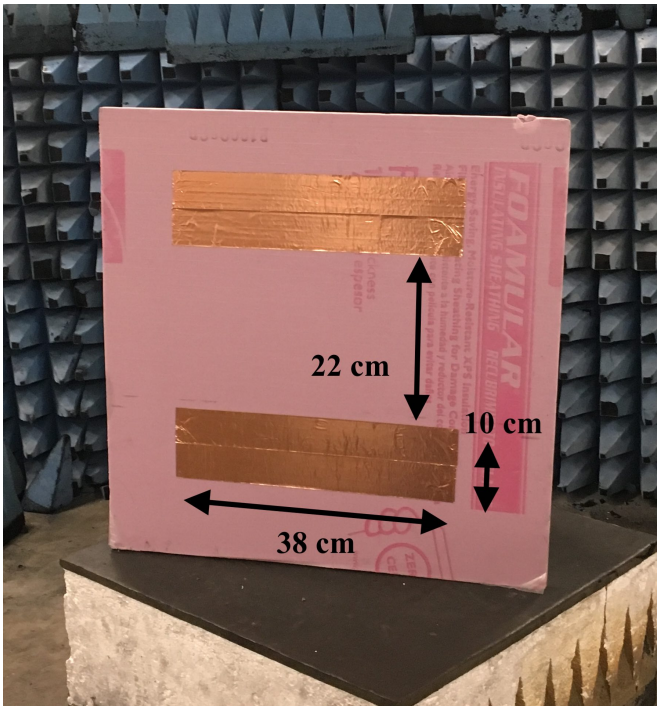

Figure 4.12: Target consisting of two reflecting stripes from copper tape inside the semi-enclosed arch range. Image [11] © 2021 IEEE.

transforms can take place.

Image formation time is closely tied to the sensitivity of an interferometric imager. The sensitivity ΔS of a radiometric receiver in Kelvin is inversely proportional to the square root of the system bandwidth B and integration time T by

$$\Delta S = C \frac{T_{\text{sys}}}{\sqrt{BT}} \tag{4.14}$$

where T_{sys} is the system noise temperature and C is a constant that depends on the receiver configuration [25, 29]. Because thermal radiation has very low power at millimeter-wave frequencies, passive systems with significantly high gain can still require observation bandwidths of hundreds of megahertz or more, and require integration times from milliseconds up to seconds [63, 77]. Another example is the high speed optical cameras which do not operate well under low light conditions because of the necessary integration time to obtain reasonable image sensitivity. In contrast, active incoherent millimeter-wave imaging significantly increases the received signal strength utilizing the noise illumination, enabling the use of very short integration times. Employing data

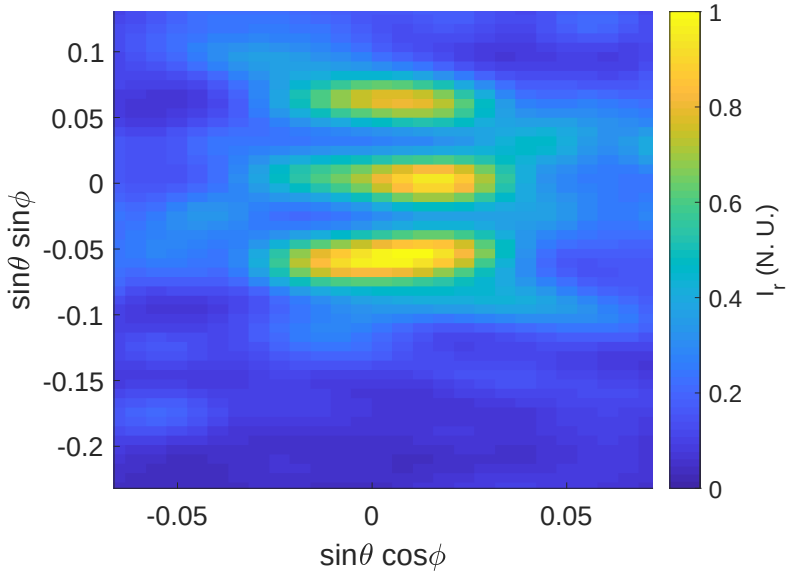

(a)

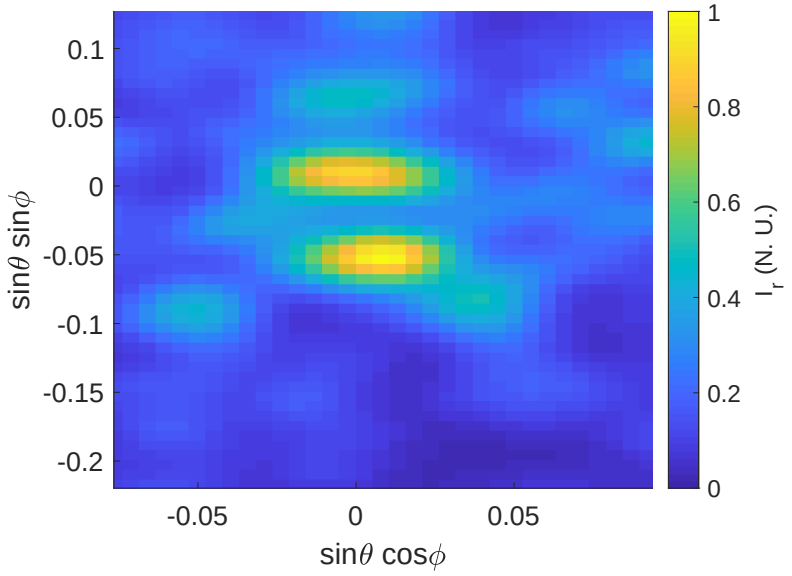

(b)

Figure 4.13: (a) Experimental raw image reconstruction of two reflecting stripes prior to system calibration. There is a third response present that does not correspond to any stripe in the scene. (b) Experimental image reconstructions of the two reflecting stripes after calibration using the redundant baselines in the array. The two responses can now be clearly resolved. Image [11] © 2021 IEEE.

acquisition hardware with sampling rates in the order of MSamples/s, receiver time-bandwidth products [78] on the order of 1000 or more can be achieved with integration times on the order

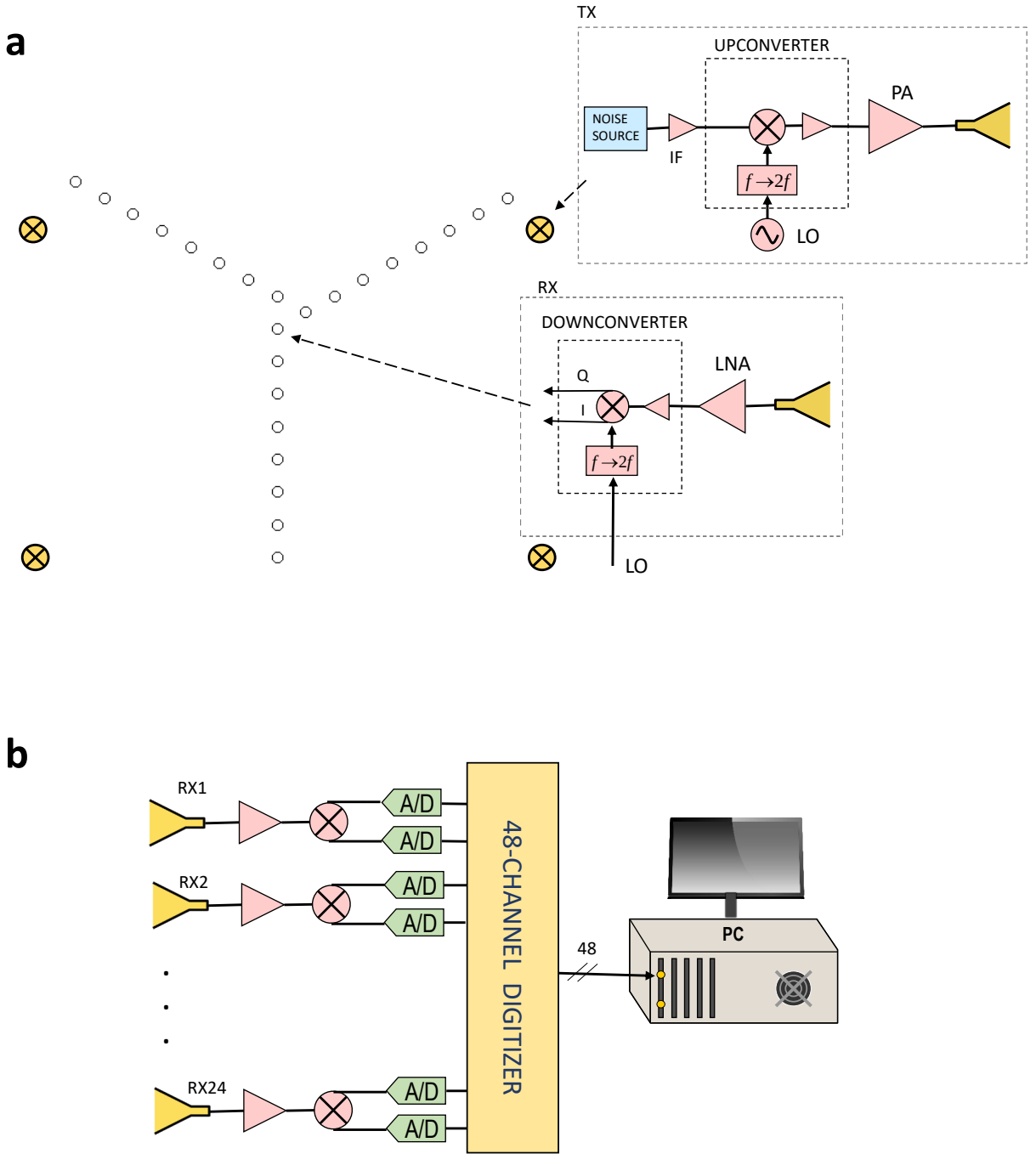

Figure 4.14: (a) High-speed interferometric imaging system architecture; 24 receivers (represented by white circles) are located in the locations of an asymmetric Y-array and 4 transmitters (represented by the yellow circles with crosses) are placed at spacing slightly greater than the receiving array. (b) Simplified digital array architecture used in this work. The receive waveforms are quadrature downconverted and then captured by three 16-channel digitizers (48 channels in total) hosted in a computer. Image [1] © 2021 IEEE.

of microseconds, which are sufficient for interferometric image formation as it was seen from the analysis in Chapter 3. These integration times are orders of magnitude shorter than what passive millimeter-wave imaging systems typically use and at least one order of magnitude shorter than what most computational microwave imaging techniques employ [36].

4.6 24-Element Array Hardware and Software Architecture

Because the number of baselines in an interferometric array with N elements increase by $\mathcal{O}(N^2)$, a significant increase in the sampled information can be achieved by increasing the number of antenna elements by 50%. In this array design the number of antenna elements was increased from 16 to 24. The system diagram is shown in Fig. 4.14. The incoherent imager employs four noise transmitters placed outside the receiving array, and 24 receivers shaped in an asymmetric Y configuration, which are shown in Fig. 4.14(a). The asymmetric Y shape was chosen because of the high density of its spatial sampling function and the good redundancy properties that were discussed in the previous system [79]. The 24-element receive array is element-level digital, as was the case for the 16-element one, meaning that all processing of the signals received at each element occurs in the digital domain; this is not the case for traditional phased arrays, where analog signal combination before sampling is typical. A block diagram of the digital array is shown in Fig. 4.14(b). The use of active noise significantly shrinks the integration time compared to passive millimeter-wave systems, therefore image formation algorithms can quickly take place using multi-channel digitizers and a consumer-grade computer in time-domain. This aleviates the need for wide bandwidth radio receivers and for dedicated processing hardware like field programmable gate arrays (FPGAs) [80]. Additionally, interferometric image formation does not require the solution of an inverse problem computationally expensive iterative algorithms found in computational imaging techniques. A photograph of the complete imaging system can be seen in Fig. 4.15.

The 38 GHz digital array millimeter-wave imager consisted of 24 receiving elements and 4

© 2021 IEEE. Sections 4.6 and 4.7 are adapted with modifications, with permission, from "S. Vakalis, D. Chen and J. A. Nanzer, "Millimeter-Wave Imaging at 652 Frames per Second," in IEEE Journal of Microwaves, vol. 1, no. 3, pp. 738-746, July 2021".

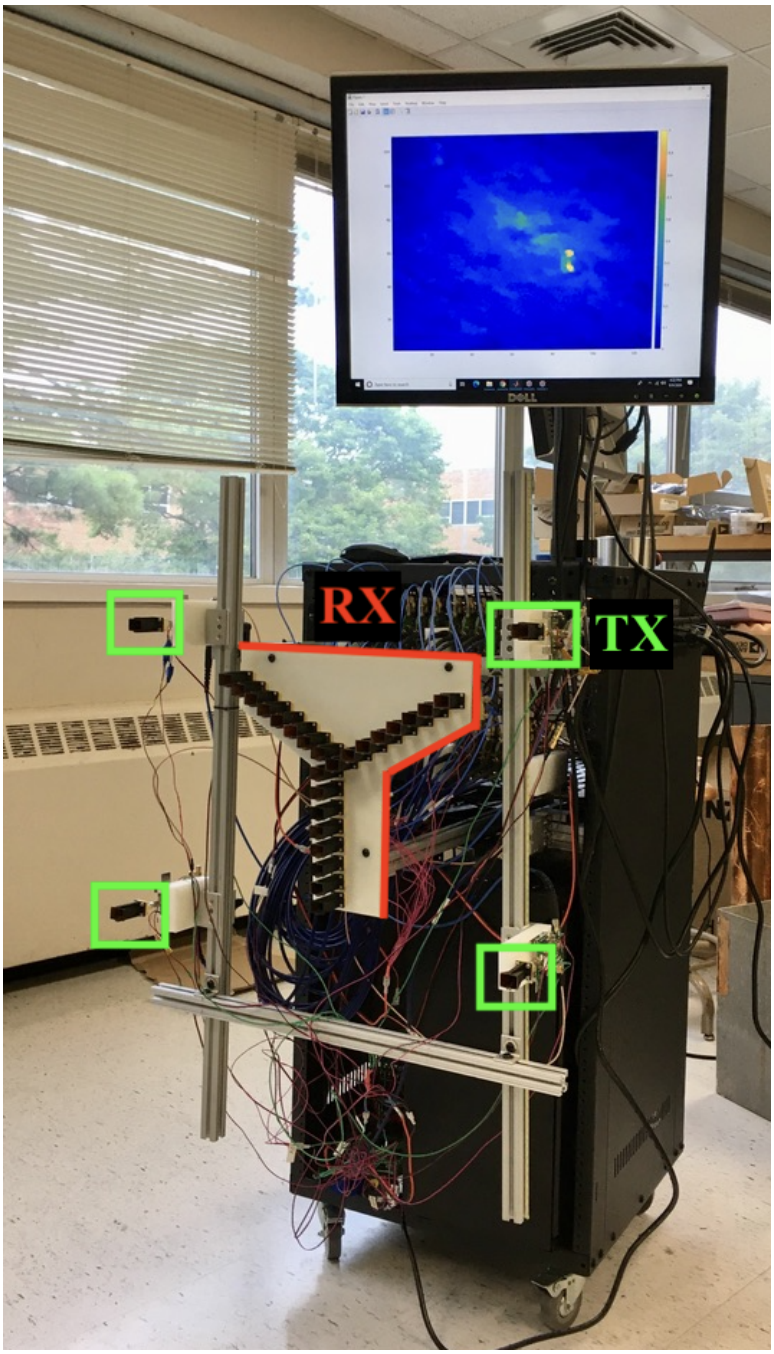

Figure 4.15: Photograph of the complete millimeter-wave imaging system. The incoherent noise transmitters are outlined in the green boxes, while the 24 receivers in asymmetric Y-array formation is outlined with red color. The millimeter-wave hardware, power supplies, digital hardware, and computer are all hosted inside the rack. The signal and image processing takes place inside the host computer.

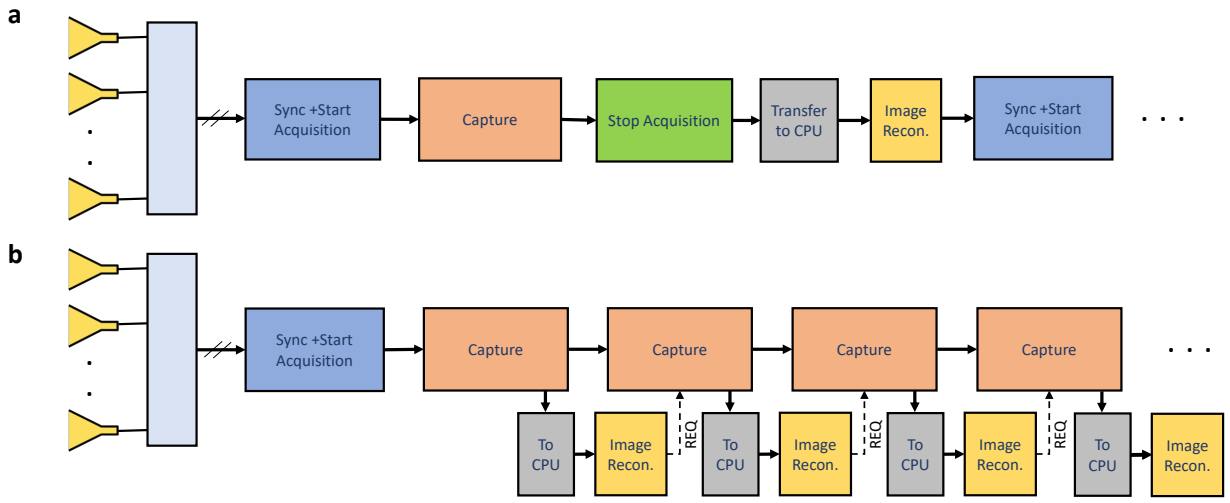

Figure 4.16: Overview and comparison of a serial-based data acquisition and image formation approach and the proposed parallel acquisition and image formation approach presented in this work. (a) Serial data acquisition and image formation. The Synchronize (Sync) + Start Acquisition and Stop Acquisition steps are taking place in every data capture, leading to long latencies in the image formation. (b) Parallel data acquisition and image formation. The Sync + Start Acquisition process only needs to be implemented once, after which, data captures are obtained continuously. In parallel, the data is transferred to a central processor unit (CPU) for image reconstruction when there is a request (REQ). The Stop Acquisition command is implemented only once when the acquisition is halted. In this way, the capture time period (integration time of the noise signals) represents the theoretically limiting factor; a 1 ms integration time thus has a theoretical limit of 1000 fps. In the system presented in this section, transferring data to the processor and the image formation process consume more time than the capture, yielding 652 fps with a 64 μs integration time/capture window length. Therefore reducing the transfer latency and image processing time will serve to further increase the frame rate of the system. (The block sizes in this image are not commensurate with time durations.) Image [1] © 2021 IEEE.

transmitting elements. The 24 receivers (RX) were placed in a Y-array formation [79], and the spacings between neighboring receive antenna elements was 24 mm (3.04 λ). The unambiguous field of view of the imager is 22° and 38° in the azimuth and elevation planes, respectively. The maximum separation of the antennas in the horizontal and vertical axes of the array was D_x = 31.2 cm and D_y = 27.6 cm. The imager has a spatial resolution of 1.3° and 1.44° in the azimuth and elevation planes, respectively. This is a slight improvement compared to the array resolution presented in the previous section.

The 3D printed receiving antenna holding structure had horizontal and vertical dimensions of 34 cm and 34 cm, respectively. The 4 transmitters (TX) were separated at horizontal and verti-

cal spacings of 56 cm and 49 cm, respectively. The low cost noise sources were replaced with 0.1–2 GHz calibrated noise sources with 15 dB excess noise ratio (ENR), that were upconverted to 38 GHz using ADI HMC6787A upconverters for the transmitters. At 38 GHz the noise signals were amplified using ADI HMC7229 power amplifiers, feeding approximately 0 dBm total power power into every transmit antenna. Both transmitters and receivers utilized 15 dBi 3D-printed horn antennas that were fabricated at Michigan State University. As a result, the effective isotropic radiated power (EIRP) of every transmitter can be approximated to be 15 dBm over the total bandwidth. Because all four transmitters were incoherent with each other, the total EIRP of the imaging system was approximated as 15 dBm + 6 dB = 21 dBm. For the receivers, each standard gain horn antenna was followed by a 20 dB gain ADI HMC1040 LNA before being downconverted to baseband using an ADI HMC6789 I/Q downconverter. The same 19 GHz local oscillator (LO) was used for all the downconverters after being split into 24 ways.

The downconverted signals were captured using this time three 16-channel ATS9416 14-bit, 100 MSamples/s, AlazarTech waveform digitizers installed on the computer. The three digitizers clocks were frequency locked and triggering in time-domain took place using a common 1 kHz signal that was generated from an Arduino UNO in order to make sure that there was no frequency difference or timing jitter between the 48 baseband channels (24 complex signals). The host computer processor was an Intel i9-9820x and the computer had a total of 64 GB of RAM. All parts of the system were mounted on the computer rack. The digitizers were placed inside the computer which was located at the bottom of the rack. The transmit and receive millimeter-wave and digital hardware and power supplies were located on different shelves of the rack. The signal processing and image reconstruction algorithm was implemented in MATLAB. The received signal captures were processed in parallel with the data acquisition so that delays due to arming and stopping an acquisition can be minimized.

In traditional millimeter-wave imaging systems, the image reconstruction algorithm is utilizing a serial data acquisition and image formation approach, as shown in Fig. 4.16(a) [80]. Using this approach, data captures are initialized and terminated with each data buffer associated with

a reconstruction frame. The information can then be transferred to a processing unit where the image reconstruction takes place. Serial data acquisition and image formation is one of the simplest approaches to implement, however this can have significant latencies because of starting and stopping the data acquisition and can significantly increase the total time of data acquisition and image reconstruction, therefore slowing down the frame rate.

In the millimeter-wave imaging architecture of this section, data acquisition and image formation take place in paraller and this minimizes the most significant latencies involved with the traditional serial approaches. Additionally, this can open the road for future improvement of frame rates. In the parallel acquisition and image formation approach, shown in Fig. 4.16(b), data acquisition synchronization and initialization takes place only once at the beginning of the millimeter-wave video capture. The received waveforms are captured continuously, and even when the image reconstruction is taking place, they still get captured in parallel. Once a millimeter-wave video frame is reconstructed, the processor submits a request for the next available buffer to utilize for the reconstruction of the next frame. Stopping the acquisition is implemented only once at the end of the whole process. This approach minimizes time delays and therefore increases the image reconstruction frame rate by effectively eliminating delays associated with data capture initialization and termination, as they only take place at the beginning and end of the entire video process, rather than in every data capture. In theory, the limiting latency factor is the integration time, which is proportionate to the time duration of the capture. If transferring the data and reconstructing the image takes considerably less time than the observation time, the theoretical maximum frame rate can be approached. In theory, using an integration time of 100 μs a frame rate of 10000 fps could be achieved.

The image reconstruction algorithm, which is indicated in the yellow box in Fig. 4.16, is summarized in Fig. 4.17. The reflections of the incoherent noise signals from the scene are captured at the 24 antenna element locations of the receive asymmetric Y-shape array. The complex voltage signals $V_i(t)$, which contain the in-phase (I) and quadrature (Q) component of the ith antenna element, are captured with 48 synchronized digitizers in parallel. In order for the pairwise cor-

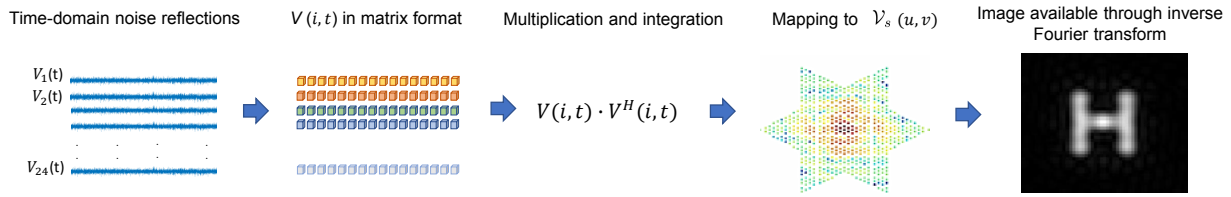

Figure 4.17: Signal processing and image reconstruction algorithm overview. The received noise signals which are reflected from the imaging scene are captured in time domain using the digitizers. The received signals are then used to create the voltage matrix $V(i,t)$. In order to get all the different antenna pair combinations, the voltage matrix is then multiplied with its conjugate transpose $V^H(i,t)$, which is a very computationally efficient operation. Next, the pairwise correlation are mapped to visibility samples $\mathcal{V}_s$, that correspond to the element locations, and finally the image is reconstructed through an inverse Fourier transform. Image [1] © 2021 IEEE.

relations to take place between all the antenna elements in the array. The matrix $V(i,t)$, which contains the complex response of the ith element as a function of time, is multiplied with its conjugate transpose. In this way each row of the matrix $V(i,t)$ is multiplied with each column of $V^H(j,t)$, which is the conjugate response of the jth element, and then summed (integrated). This can also be interpreted as the dot product between every two receive antenna elements. Next, the cross-correlations are mapped to visibility samples $\mathcal{V}_s$ based on the antenna pairs generating the samples, and the image is reconstructed through an inverse Fourier transform. On the right of Fig. 4.17, the simulated reconstruction of an "H"-shaped target is shown.

The observation time used in this section was 64 μs, however the latencies associated with the data transfer and image formation were not eliminated which limits the frame rate to 652 fps. The total latencies can be estimated to be equal with $\frac{1}{652}$ s - 64 μs = 1.469 ms. This means that there is still significant room for improvement and the image reconstruction frame rate can increase even more by using a higher-speed data bus for transferring data and an application-specific integrated circuit (ASIC) for the image formation and data acqusition.

4.7 Experimental High Speed Image Reconstructions

Proof-of-concept experiments took place in a semi-anechoic environment. The first target consisted of five spheres in a step formation, shown in Fig. 4.18. Each sphere had a diameter of 10 cm and the distance between neighboring spheres was 15 cm in both horizontal and vertical dimensions.

Figure 4.18: Target comprised of five reflecting spheres in a step formation. The diameter of every sphere was 10 cm and the distance between neighboring spheres was 15 cm. Image [12] © 2022 IEEE.

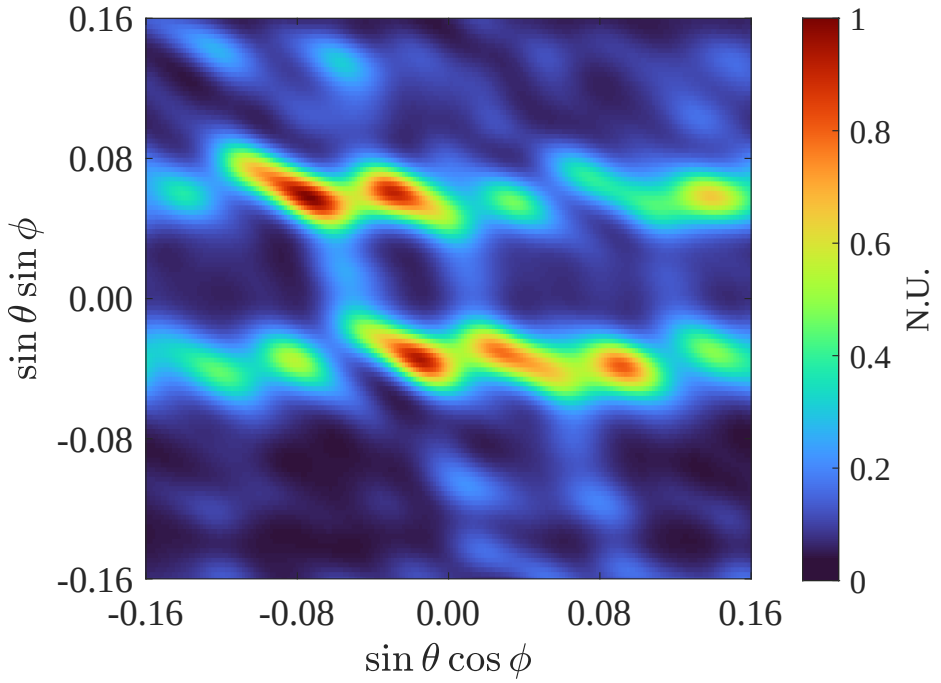

Figure 4.19: Active incoherent millimeter-wave image reconstruction of the target comprised of five spheres. Image [12] © 2022 IEEE.

Fig. 4.19 shows the output of the imaging system. Although there is blurring and artifacts present in the system, all responses from the five targets were captured even though they were spaced at increments close to the array resolution. Additionally, a pendulum was created by fixing a 50 cm transparent fishing line on a mount on the ceiling. A foam sphere covered with aluminum tape

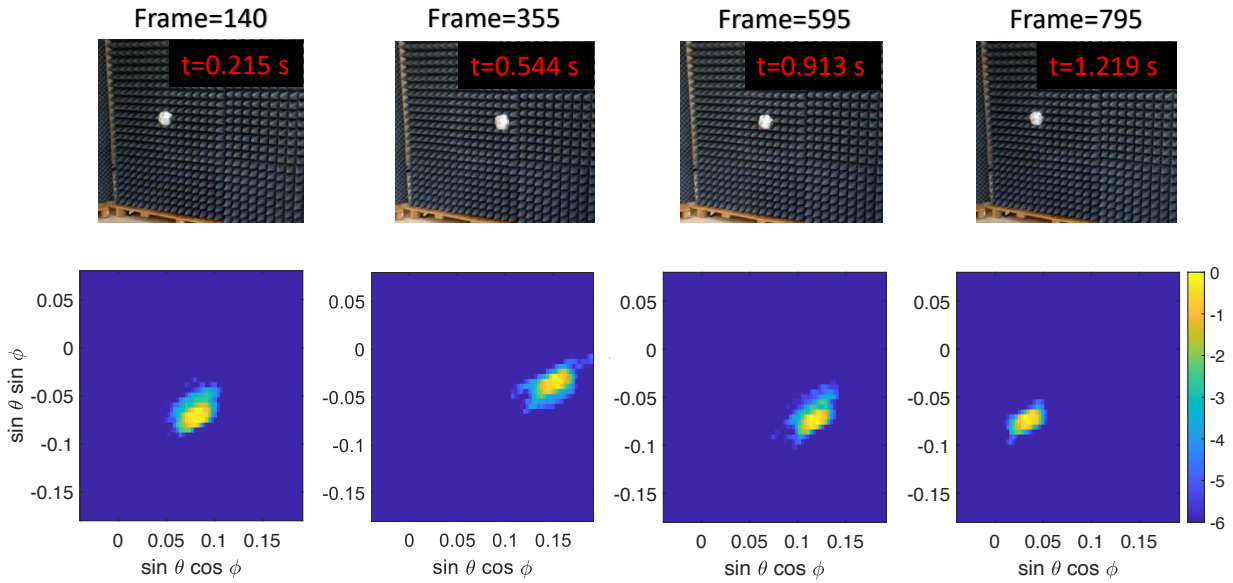

Figure 4.20: High-speed imaging results. Four different frames of the optical video of the pendulum (top) and millimeter-wave image reconstruction (bottom). The colorbar values correspond to the reconstructed image intensity I_r and are in dB. A slow motion video can be found in the supplemental material of [1]. Image [1] © 2021 IEEE.

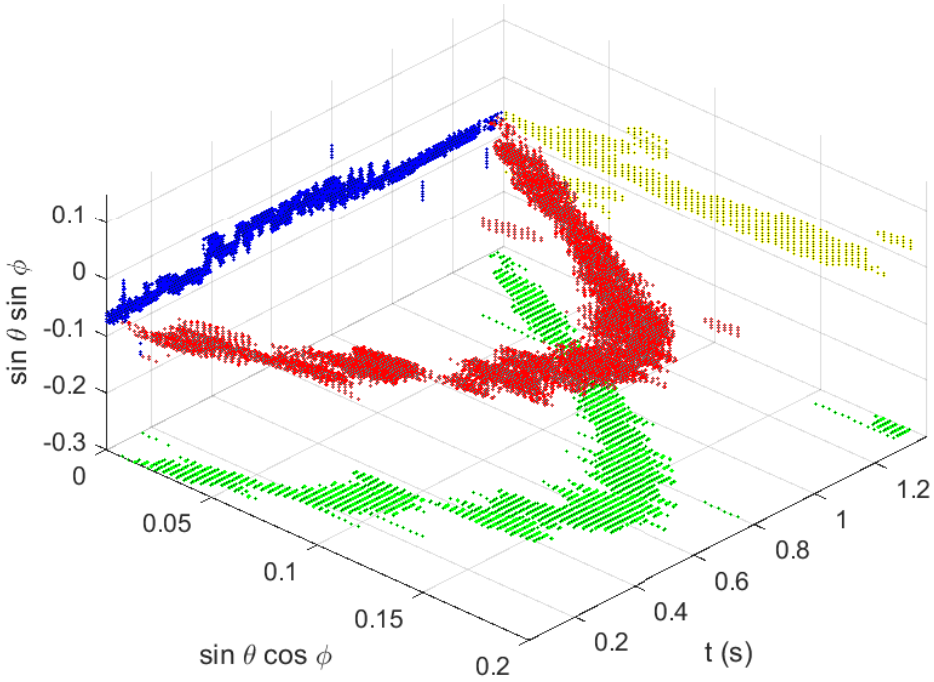

Figure 4.21: Three dimensional plot showing the pendulum movement as a function of the two direction cosines $\sin\theta\cos\phi$ and $\sin\theta\sin\phi$ and time. Image [1] © 2021 IEEE.

with a 7.6 cm diameter was attached at the end of the line in order to create a highly reflecting and lightweight structure. The sphere was swinging in a pendulum motion across the field of view of the imaging array and was located at a distance of 1.12 m away from the array, yielding a received power of -68 dBm at the output of each receive antenna at 38 GHz and a total power of -58 dBm if all the IF bandwidth is utilized. While a comparison to passive systems is not directly feasible since passive systems detect thermally generated signals and not reflected signals, a sphere with perfect emissivity of the same size at room temperature emits a thermal power of $P_t = kTB$, where $k = 1.38 \times 10^{-23}$ is the Boltzmann constant, $T = 290\ K$ can be used as the room temperature, and $B = 50$ MHz is the receiver bandwidth. The received power can be found via the Friis transmission equation to be equal to -111 dBm at the output of each receiver antenna. This represents an ideal case, as it assumes perfect emissivity and full use of the receiver bandwidth, but is nonetheless significantly lower than that for the active system and would require much higher gain for equivalent sensitivity. Note that this is even without consideration of the total integration time; the sensitivity of passive imagers is inversely proportional to the square root of the integration time; thus shorter integration times yield larger (worse) sensitivity.

Four screenshots of the millimeter-wave image reconstructions of the sphere moving in the pendulum motion and the corresponding optical frames can be seen in Fig. 4.20 in a time-lapse fashion. A slow-motion millimeter-wave video capture of the moving pendulum sphere can be found in the supplemental material of [1] along with the slow-motion optical video that was captured using an iPhone SE at 240 fps. The slight blurring and skewness of the target response is the result of the imperfections of the shape of the sphere: the aluminum tape covering the sphere was not smooth with roughness in the order of a wavelength, thus reflections from the sphere do not appear as an ideal point source. Denoising using a total variation constraint was used on the millimeter-wave images [81]. The millimeter-wave video snapshots was not plotted in real-time as the computer display did not have the required refresh rate. The imaging frame rate of the experimental configuration was calculated by using the slow-motion optical video with time stamps as ground truth. These calculations were also cross-validated with the pendulum oscillation period

$T = 2\pi\sqrt{\frac{L}{g}}$, where L was the line length and g is the gravity acceleration constant. A three-dimensional plot of the sphere motion is shown as a function of azimuth, elevation, and time in Fig. 4.21. The red color shows the oscillatory motion of the sphere as a function of time. Blue, yellow, and green represent the projection in the different planes.

4.8 Chapter Conclusion

Leveraging active incoherent signal illumination, interferometric imaging, and element-level digital processing, millimeter-wave imaging with speeds more than 26 times faster than current millimeter-wave imaging approaches has been achieved [50]. While the results in this chapter were demonstrated in a controlled environment with simple calibration targets, this work represents a significant leap in the current state of the art, where rapid millimeter-wave imaging can be applied in a wide range of industrial, medical, scientific, and commercial applications.

CHAPTER 5

PASSIVE NON-COOPERATIVE MILLIMETER-WAVE IMAGING USING SIGNALS OF OPPORTUNITY

5.1 Joint Wireless Sensing and Communications

Coexistence of wireless sensing and communications has been evolving to an increasingly important aspect of wireless networks [82]. Beamforming with multi-element phased arrays and transmit power adaptation will need accurate localization capabilities. Sensing can enable tracking of wireless signal blockage, wireless health monitoring for detecting elderly fall and other problems [83], Internet of things [84], human-computer interaction [85], and security sensing, among other applications. The ability to identify hidden contraband in airports and other sensitive locations, because of the good penetration characteristics of millimeter-wave radiation, can significantly prevent acts of terrorism and crime. Sensing can also prove crucial in emergency situations like earthquakes or fires, where life detection can rescue human lives.

Wireless networks are expected to become significantly more dense, especially as 5G communications technologies continue to be developed, making the coexistence of sensing and communications an increasingly important challenge. Many research works have investigated interference mitigation, and others have worked in combining sensing and communications into a joint waveform or system [86]. While the interference mitigation approach is challenged by filter technology and channel bandwidth limitations, and capacity degradation through time or frequency duplexing, the joint waveform approach is challenged by the differences between communications and radar systems, since they are designed for largely opposite functions. This leads to waveforms and transceiver hardware that are significantly different from each other. Communications signals in general occupy an instantaneously wide bandwdith in order to maximize capacity, while radar signals tend to be instantaneously narrowband in order for the phase information to be acquired. Additionally, wireless communications hardware tends to operate at power levels significantly lower

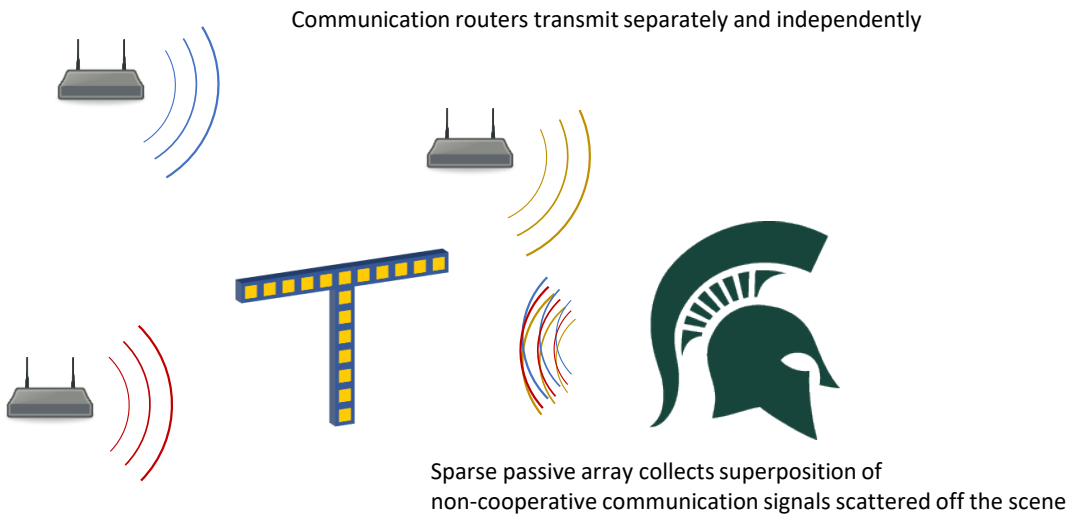

Figure 5.1: Passive non-cooperative imaging utilizes the random communication signals emitted in an environment. The receiving array captures the signals reflected off the scene. Image [5] © 2019 IEEE.

than the compression point of transmit amplifiers because of the use of amplitude modulation. Phase modulation is preferred over amplitude modulation for radar signals, so radar hardware can operate closer to the compression point of the transmit amplifiers in order to increase the SNR. Although these differences may become less distinct in future wireless millimeter-wave networks, they still present a significant challenge to joint sensing and communications.

While many works have shown localization, tracking, and activity recognition using indoor wireless network infrastructures or by transmitting and receiving signals at the existing industrial, scientific and medical (ISM) microwave bands [87–90], few works have demonstrated image reconstruction using 802.11-compliant communications signals. This has been implemented by means of mechanical scanning and coordination between transmit and receive platforms [91, 92]. Holography with WiFi has taken place, but this can require either mechanically scanning antennas in space or a fully-populated two-dimensional aperture [93]. Recent works have showed three-dimensional millimeter-wave imagery using coordination between a transmitting 5G base station

and an auxiliary receiving phased array [94–96]. The approach presented in this chapter requires no synchronization between transmit and receive, providing an opportunity for future joint sensing and communications in dense signal environments with reduced system complexity.

This chapter examines the possibility of using stray non-cooperative communications signals in order to perform passive non-cooperative interferometric imaging using the already existing signals in the environment. Active incoherent millimeter utilizes transmission of noise signals from multiple locations in order to mimic the properties of thermal radiation and satisfy the Van Cittert-Zernike theorem requirements [3, 11], however, this requires additional transmit signal emitted in an already crowded environment.

5.2 Incoherence of Multiple Communication Signals Using Mutual Coherence

Thermal sources inherently emit noise-like signals and therefore passive interferometric imaging systems are not affected by unwanted spatial coherence. However, when the signals being captured are actively transmitted, it is necessary to ensure that the radiation scattered off the scene is sufficiently uncorrelated such that the unwanted coherence cross-terms still tend to zero. Chapter 3 shows that radiation from incoherent sources, including communications transmitters, can satisfy the incoherence requirements on the near-field and that coherence in the far field is inversely proportional to the number of transmitters employed. This section revisits the coherence calculations and is concerned with how a more relaxed metric can describe the propagation of coherence.

To assess the spatial incoherence of the signals, the fields impinging on the scene, characterized in matrix form $\mathbf{E}$ with dimensions of time, azimuth plane projection, and elevation plane projection, are analyzed in terms of the coherence between the spatial dimensions of $\mathbf{E}$. The following analysis is an attempt to quantify the incoherence of the spatio-temporal transmit pattern, and verify that the dependence between the individual point responses is small. The calculation of the electric field is not needed for the image reconstruction, and no knowledge of the transmit radiation is needed.

© 2019 IEEE. Sections 5.2 and 5.3 are adapted with modifications, with permission, from "S. Vakalis, L. Gong and J. A. Nanzer, "Imaging With WiFi," in IEEE Access, vol. 7, pp. 28616-28624, 2019".

As we saw on chapter 3, the maximum degree of coherence γ of a matrix $\mathbf{E}$ with K columns and T rows is defined as the maximum absolute value of the cross-correlation between the columns of the matrix through

$$\gamma(\mathbf{E}) = \max_{1 \leq k \neq j \leq K} \frac{|\epsilon_k^H \epsilon_j|}{||\epsilon_k|| ||\epsilon_j||} \tag{5.1}$$

where ϵ_k is the k-th column of $\mathbf{E}$. In our case K is the number of spatial points of the calculated electric field.

Eq. 5.1 shows the maximum coherence between two columns of the matrix, which corresponds to two spatial points, and as a result, it is representative of the worst-case. This particular metric became very popular in the compressive sensing research [97] because, if a sensing matrix $\mathbf{E}$ has low enough mutual coherence, the reconstruction of the signal with fewer samples than dictated by the Nyquist criterion will still succeed with very high probability. This metric can thus help with comparing the performance of different sensing matrices for sparse representation or reconstruction of signals and images [98].

Low values of mutual coherence between two vectors correspond to low dependency between them, and both interferometric and compressive imaging systems require an incoherent spatio-temporal pattern for the image reconstruction process to succeed. However, the spatio-temporal pattern for compressive sensing systems needs to be completely known, in general, while for the presented imaging system with WiFi signals, the knowledge of the exact transmit pattern is not required as long as it is known to be partially incoherent. Additional spatial variation is also added from the multiple antenna locations that the reflections are measured from. Therefore a more general metric can be adopted, which is the average spatial mutual coherence [99], given by

$$\bar{\gamma}(\mathbf{E}) = \frac{1}{K(K-1)} \sum_{k \neq j} \frac{|\epsilon_k^H \epsilon_j|}{||\epsilon_k|| ||\epsilon_j||} \tag{5.2}$$

As shown in (2.21), the average spatial mutual coherence is considerably important because of the integration process that combines the radiation from multiple single points simultaneously. Lower values of average spatial mutual coherence can also be more easily achieved than low values of the maximum degree of coherence. The average value of the cross-correlations between the columns

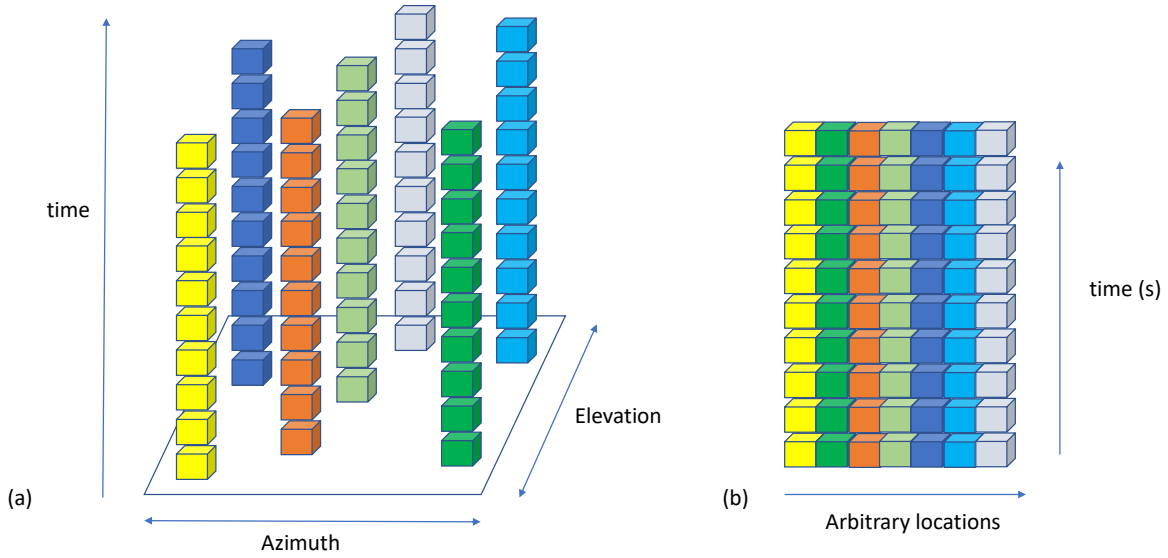

Figure 5.2: (a) The three-dimensional matrix that represents the incoherent spatio-temporal pattern, where same color represents same point. (b) The two-dimensional equivalent matrix that resulted from reshaping the three-dimensional matrix. Image [5] © 2019 IEEE.

will give a measure of the unwanted information in the image, as a result of the superposition of all points on the aperture of the antenna.

To analyze a system using the incoherent radiation from three WiFi transmitters using the average spatial mutual coherence of the spatio-temporal transmit pattern, the transmitted signals are first defined by

$$E(\alpha, \beta, t) = \sum_{l=1}^{3} \int_{f_c - \frac{1}{2}\Delta f}^{f_c + \frac{1}{2}\Delta f} S_l(t) e^{-j2\pi \frac{f}{c}(d_{xl}\alpha + d_{yl}\beta)} df \tag{5.3}$$

where $S_l(t)$ is the 16-QAM signal coming from the l-th transmitter, f_c is the carrier frequency, Δf is the equivalent receiver bandwidth, and the d_{xl}, d_{yl} terms represent the location of the l-th transmitter in the x and y directions accordingly.

The spatio-temporal transmit pattern is modeled as described earlier, as a three-dimensional

matrix **E** where the first two dimensions are selected as the two angular dimensions that the antenna array observes the scene from, and the third dimension is time. One may think of the three-dimensional matrix as a collection of vectors incident to a two-dimensional plane as shown in Fig. 5.2(a), where only a set of the columns is shown in order to simplify the figure and make it easily understandable. The two azimuth and elevation dimensions indicate the location of every single radiating point. The vertical sets of same color cubes indicate the single point responses over time. To satisfy the Van Cittert-Zernike theorem, the columns in the matrix must be statistically independent.

In order to quantify the independence or incoherence of the columns we use the average spatial mutual coherence metric for a three-dimensional matrix calculated from (5.2). The three-dimensional matrix shown in Fig. 5.2(a) can be easily reshaped to become two-dimensional by keeping time as the one dimension and combining the two angle dimensions into one as shown in Fig. 5.2(b). This three-dimensional to two-dimensional matrix reshaping is used to speed up computational time and also to keep the chapter's structure consistent to the widely used definition of degree of coherence in literature for two-dimensional matrices. We calculated the spatio-temporal transmit pattern in MATLAB for three random 16-QAM signals modulated on a carrier frequency of 5.5 GHz with 25 MHz of bandwidth. The three-dimensional spatio-temporal transmit pattern was calculated from (5.3), and it was transformed from a three-dimensional matrix into a two-dimensional matrix, as shown in Fig. 5.2. The maximum degree of coherence of the matrix, given by (5.1) was found to be equal to 1, which means that some point sources were coherent, but the average spatial mutual coherence, given by (5.2), was found to be equal to 0.32 for 10 s, and by randomizing the locations of the transmitters, this number was very consistent. This means that the normalized coherent part of the radiation coming from two different point sources will be on average less than the one third of the normalized single point response, indicating that the columns are largely independent. This analysis focuses on the transmit pattern and does not take into account the spatial variations when measuring the field in two different locations, for example when two antenna elements are separated by a certain number of wavelengths. Objects in a real scene will

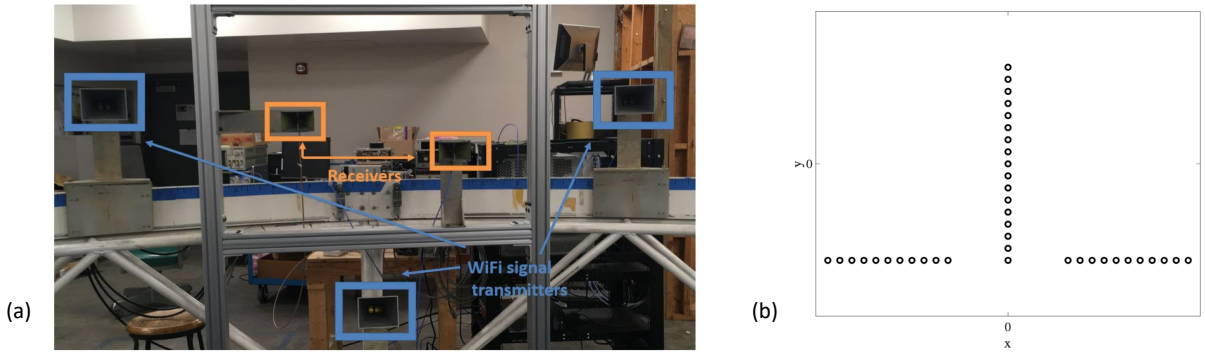

Figure 5.3: (a) Configuration for the experimental 5.5 GHz measurements with three transmitters and two receivers synthesizing a 15 λx8 λ array by moving them in the horizontal and vertical direction. (b) The locations of the synthesized array in $\lambda/2$ increments. The narrow baselines are missing due to the dimensions of the horn antennas. Image [5] © 2019 IEEE.

add additional unknown amplitude and phase changes randomly, which will further decorrelate the columns of **E**, and will serve to reduce the average degree of coherence further. Regardless, the following section demonstrates experimental measurements, showing that average spatial mutual coherence levels of around 0.32 are nonetheless sufficient for the WiFi imaging approach.

5.3 Experimental Microwave Image Reconstructions Using WiFi Signals

The non-cooperative WiFi imaging system was demonstrated by creating a two-dimensional experimental system operating at 5.5 GHz. Since this is a two-dimensional imaging setup, three transmitters were used, each emitting a pseudo-random sequence of 16-QAM signals from 15 dBi antennas. The signals were generated at the carrier frequency using a Keysight M8190A Arbitrary Waveform Generator, which has only two independent outputs. Therefore, one of the outputs was split into two signals, with one signal fed directly to an antenna and the other delayed through a 7.6 m cable before being fed to another antenna after additional amplification to compensate for the losses. This additional time delay ensured that the signals impinging on the scene were independent and uncorrelated, having the same effect as three independent WiFi transmitters. The scene consisted of two reflecting spheres placed at the center of a 7.3 m antenna range. For the receive array, because interferometric processing is pairwise processing, a larger array can be syn-

(a)

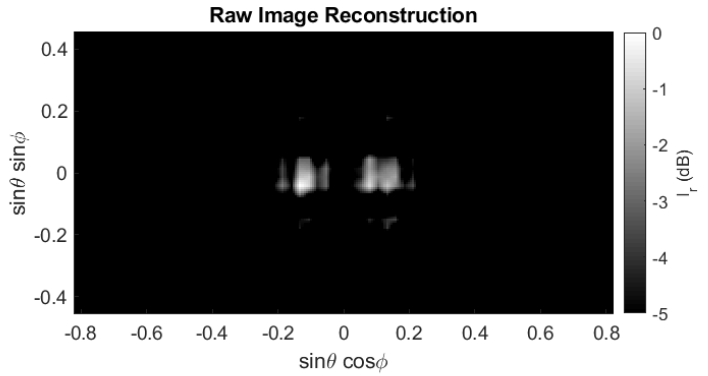

(b)

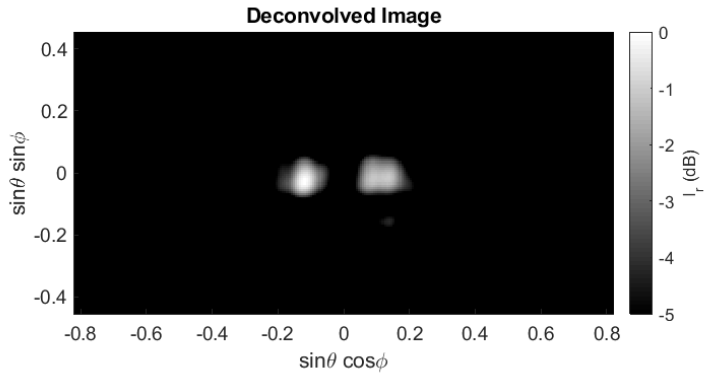

(c)

Figure 5.4: (a) The two reflecting calibration spheres used as the two-dimensional scene inside the semi-anechoic environment. (b) Raw 5.5 GHz image reconstrucion of two reflecting spheres, using stray WiFi reflections. (b) Deconvolved image using the calculated PSF, in which the two responses can be clearly distinguished. The reconstructions are normalized, therefore the colorbar units are in dB. Image [5] © 2019 IEEE.

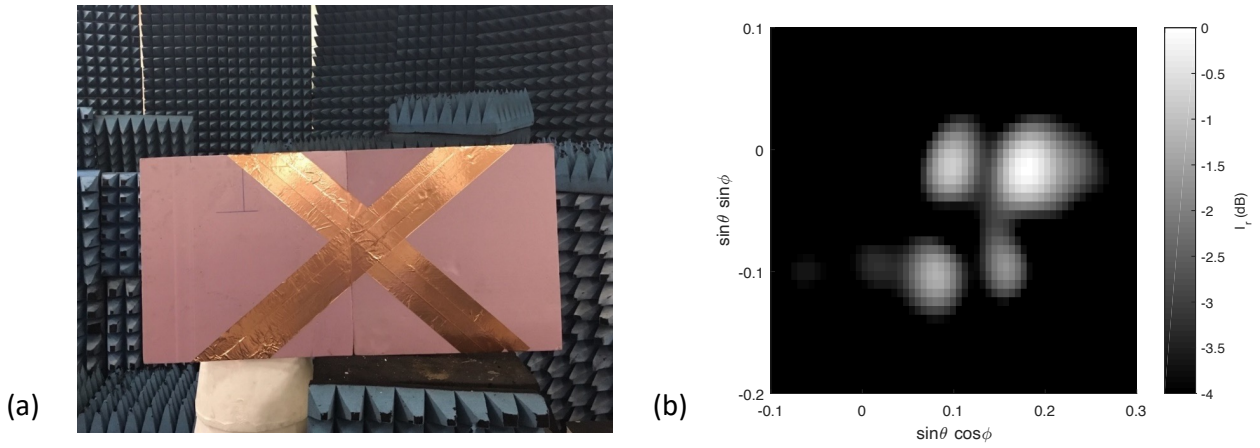

Figure 5.5: (a) The "X"-shaped target, made out of copper-tape glued on a foam board, used as a distributed scene with features smaller than the array resolution. (b) Reconstructed 5.5 GHz image of the reflecting X-shaped target, using stray WiFi reflections. Although this target is more challenging to image with the given resolution, its features can be distinguished. The reconstruction is normalized, therefore the colorbar units are in dB. Image [5] © 2021 IEEE.

thesized by collecting pairwise data with only two receive antennas, and move them sucessively to the pairwise locations found in a two-dimensional inverse T-array. This process yields image formation equivalent to capturing the signals simultaneously in a filled array, since the image information is sampled on a pairwise basis. The configuration for the experimental measurements is shown in Fig. 5.3(a). The maximum horizontal and vertical dimensions of the receive array were 15 λ and 8 λ, respectively. A plot of the synthesized array locations is shown in Fig. 5.3(b). The azimuth and elevation resolution of the array can be approximated from the 3 dB aperture beamwidth to be 3.5° and 6.4°, respectively. The 16 QAM transmitters were located just outside the span of the receiving array. The reflections from the scene were captured using 10 dBi horn antennas, and the received signals were amplified using 20 dB LNAs and then downconverted to baseband using quadrature ADL5380 mixers. The baseband signals were digitized using a mixed signal MSOX92004A oscilloscope, and were processed in MATLAB.

The processing of the received signals consisted of digitally low-pass filtering the response of every antenna element to a bandwidth of 25 MHz, then cross-correlating the responses of every an-

tenna pair corresponding to unique spatial frequencies (redundant baseline spacings were omitted) and reconstructing the scene visibility. The time duration of the captured waveforms was 10 μs, an order of magnitude shorter than that of typical passive imaging systems, which makes this imaging technique very promising for real-time operation. The image reconstruction was then obtained via a two-dimensional inverse Fourier transform. Fig. 5.4(a) shows a photograph of the two reflecting calibration spheres used for the experimental measurements. The raw reconstructed image is shown in Fig. 5.4(b), captured from the synthesized locations of the inverse T-array. Fig. 5.4(c) shows the deconvolved image using blind deconvolution [100] with the calculated PSF estimate of the array shown in Fig. 5.3(b). The responses from the two spheres are clearly distinguishable.

A more complex target is shown in Fig. 5.5(a), with the shape of "X" formed from copper tape on a foam board. The "X" has edges of 94 cm and 97 cm, however its features are smaller than the spatial resolution of the 5.5 GHz WiFi imaging array. The same array configuration used for the calibration spheres was used for imaging the "X", with the result shown in Fig. 5.5B. The overall shape of the "X" is clearly apparent, with bright spots aligning with the arms of the "X". There is some information loss between the bright responses, however the overall shape is clearly distinguished, demonstrating the feasibility of imaging complex objects using 5.5 GHz WiFi signals.

The imaging system presented in this section is the first to generate two-dimensional imagery using stray WiFi signals and no synchronization between transmitters and receivers. Using this technique, full two-dimensional imagery is possible by capturing the WiFi signals present in typical wireless environments. Image reconstructions were shown using calibration spheres and more challenging distributed targets. Due to the ability of microwave radiation to propagate through construction materials, there is promise for through-wall imaging using ambient WiFi signals.

5.4 Passive Non-Cooperative Millimeter-Wave Imaging Using 5G Signals

The system presented in the previous section was the first WiFi imaging system that could oper-

© 2022 IEEE. Section 5.4 is adapted with modifications, with permission, from "S. Vakalis, S. Mghabghab and J. A. Nanzer, "Fourier Domain Millimeter-Wave Imaging Using Non-Cooperative 5G Communications Signals," in

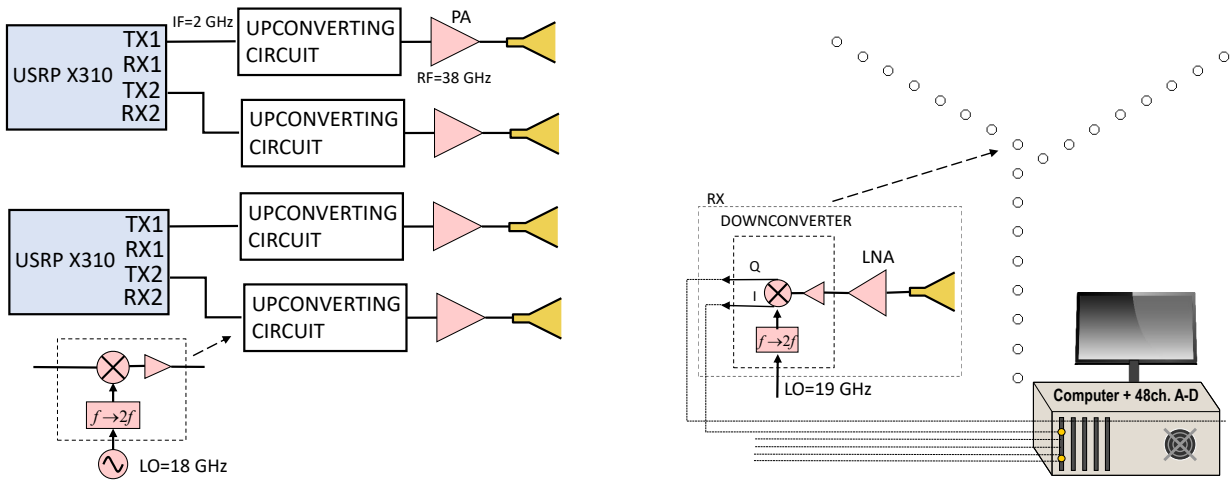

(a) (b)

Figure 5.6: (a) Schematic of the 4 38 GHz transmitting nodes employing USRP X310 SDRs emitting 256-QAM signals (only one shown in the figure). (b) Schematic of the 24-element 38 GHz receive interferometric imaging array. The receive array is the same used in Chapter 4. Image [13] © 2021 IEEE.

ate using non-cooperative communication signals in the environment. However, due to the lower microwave frequency, its spatial resolution is coarse for many applications that concern this dissertation. Examples include security screening and non-destructive testing. Higher frequencies are needed and this is what is investigated in this section. Using multiple independent 5G signals incident on a scene can satisfy the Van Cittert-Zernike theorem requirements for spatio-temporal incoherence such that Fourier domain imaging can be performed. Effectively, if enough transmitters are in a local area, the resultant signals impinging on a spatial scene can appear sufficiently similar to random noise, such that a scene image can be reconstructed if enough spatial frequency samples are collected. The temporal properties of 5G communication signals make them a very good candidate for incoherent imaging because of their instantaneous wide bandwidth, meaning that they can achieve spatial incoherence for short duration captures. The millimeter-wave frequency can also enable compact receive arrays with improved resolution. Additionally, multiple 5G transmitters lead to improved spatial incoherence with the worst case scenario represented in the far field of the transmitter array and therefore very far outside the wireless network.

IEEE Transactions on Antennas and Propagation, 2022".

The 5G transmitters configuration that was built can be seen in Fig. 5.6(a). The modulation scheme of the transmitted 5G signals was 256-QAM. The signals were generated on two dual-channel Ettus Research USRP X310 software-defined radios (SDRs) with LabVIEW. The two SDRs were not frequency locked and all four transmitters started transmitting independent information at a random time. A quadrature sampling rate (I and Q) of 20 MS/s was used with 2 samples per symbol configuration, giving a symbol rate of 10 MSymbol/s. The SDRs were generating the signals at an intermediate frequency carrier which was set to 2 GHz. The IF signals were then upconverted using an 18 GHz LO and ADI HMC6787 upconverters. The upconverter boards included an integrated frequency doubler thus the resulting RF frequency was 38 GHz, the same as the operating frequency of the imaging array. Different LOs can be used between transmit and receive in incoherent systems, which enables the passive imaging potential from third-party sources.

The block diagram of the millimeter-wave imaging array, shown in Fig. 5.6(b), consisted of 24 elements placed in an asymmetric Y-array formation. Each receiver utilized a 15-dBi 3D-printed horn antenna, an ADI HMC1040 LNA, and an ADI HMC6789 quadrature downconverter with integrated frequency doubler. Direct downconversion with a 19 GHz LO was used and both I and Q channels of every receiver (48 in total) were captured using three 16-channel ATS9416 14 bit, 100 MS/s, AlazarTech waveform digitizers. The three digitizers had frequency locked clocks and time triggering took place using a common 1 kHz signal. The integration time was 50 μs.

Experimental measurements were conducted inside a semi-anechoic environment. The passive interferometric imaging array with the 24 receivers was located next to a rack that had the four 5G transmitters mounted on it. A picture of the experimental configuration can be seen in Fig. 5.7. The target scene was two spheres, as shown in Fig. 5.8(a). The aluminum sphere was placed at a distance of 1.55 m, while the copper sphere was placed at a distance of 1.3 m from the imager. Fig. 5.8(b) shows the millimeter-wave image reconstruction, presenting an accurate reconstruction, clearly differentiating the responses of the two spheres.

Additional measurements were conducted in the same semi-anechoic environment using a tar-

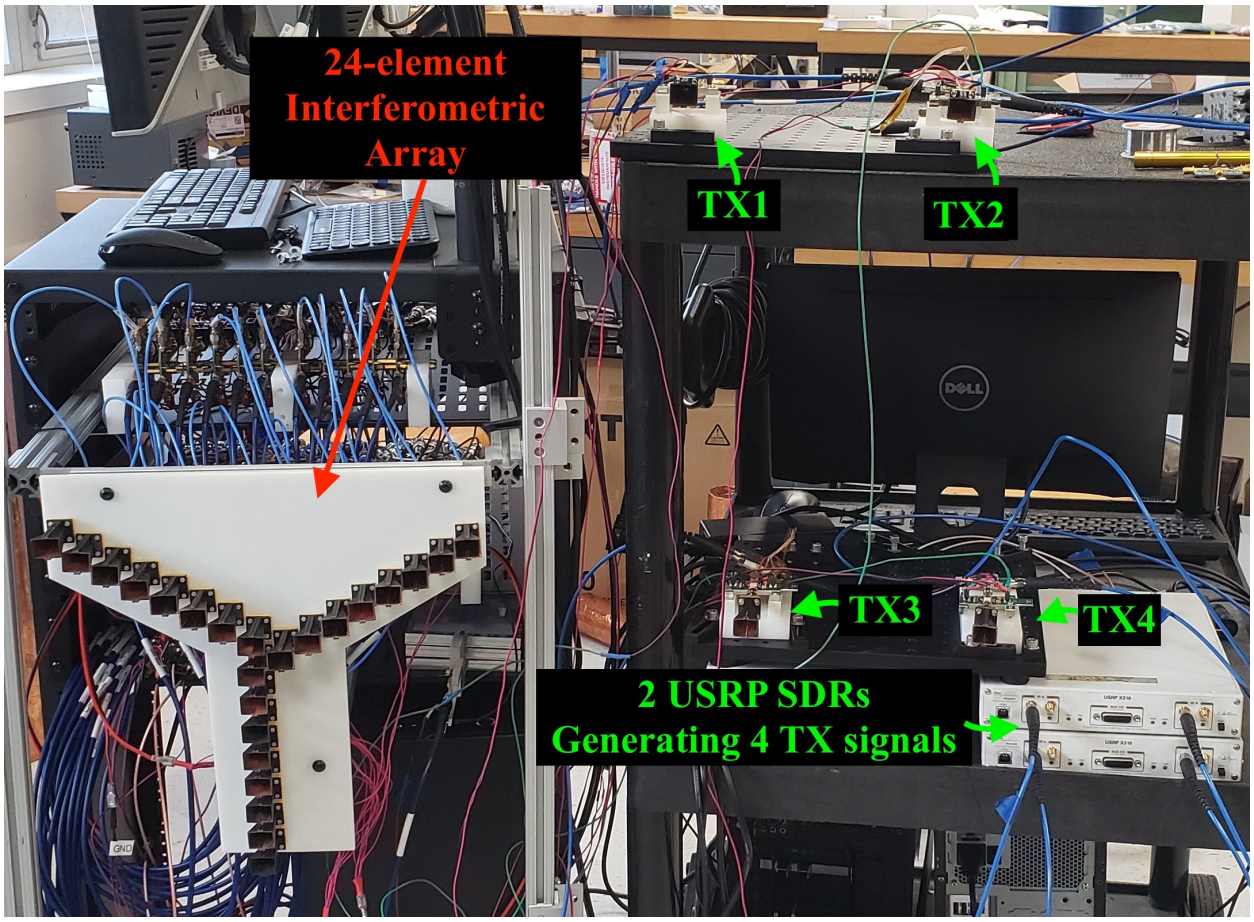

Figure 5.7: Experimental millimeter-wave imaging configuration. (left) 24-element interferometric imaging array with 3D-printed horn antennas and (right) 5G SDR-based configuration with 4 independent transmitters emitting pseudo-random 256-QAM signals. Image [13] © 2021 IEEE.

get made from two reflecting copper stripes glued on a foam board which can be seen in Fig. 5.9(a). The two stripes have dimensions of 38 cm by 10 cm, and they are separated by 22 cm. The passive millimeter-wave image reconstruction can be seen in Fig. 5.9(b). Although the two stripes have a strong specular profile, they can be easily identified.

Due to the active transmission of signals, high sensitivity is obtained at the receiver, supporting short integration times and thus fast image formation. Fig. 5.10 shows experimental results of the aluminum sphere with 12.7 cm diameter moving in a pendulum formation. The pendulum oscillation period can be found from $T = 2\pi\sqrt{\frac{L}{g}}$, where L is the line length and g is the gravity acceleration constant. The line used was 180 cm long so the period was equal to 2.69 s. In the top of Fig. 5.10, photographs of the moving sphere at different time instances can be seen. The recon-

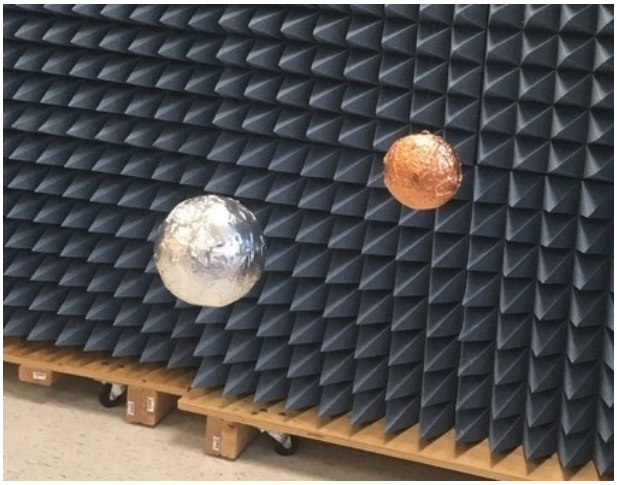

(a)

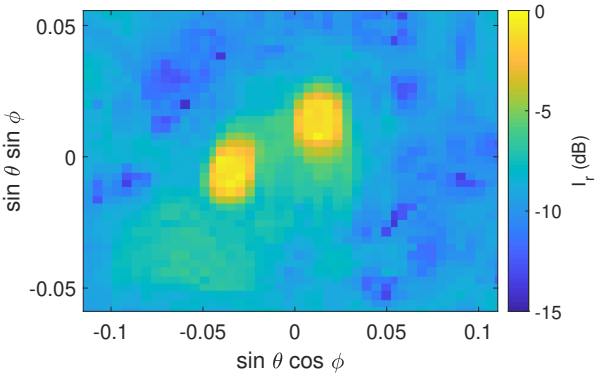

(b)

Figure 5.8: (a) Photograph of the two spheres used for the experimental measurements. (b) Passive millimeter-wave image reconstruction of the two spheres. The two responses can be clearly resolved. Image [13] © 2021 IEEE.

(a)

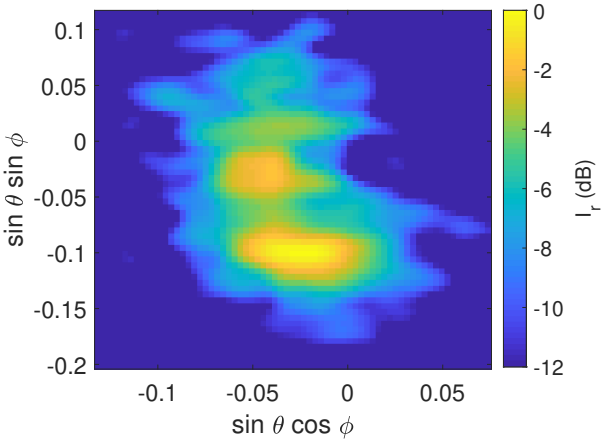

(b)

Figure 5.9: (a) Photograph of the target composed of two reflecting stripes. (b) Passive non-cooperative millimeter-wave image reconstruction of the two stripes. Image [8] © 2022 IEEE.

structed non-cooperative millimeter-wave images are shown in the bottom figures, demonstrating fast image formation of the moving sphere.

Finally, in order to examine a longer range scenario, outdoor measurements took place at the campus of Michigan State University. Two corner reflectors were used: a 41 dBsm corner reflector was placed at a distance of 5.7 m, and a 21 dBsm corner was placed at a distance of 4.6 m. A photograph of the two targets can be seen in Fig. 5.11(a) where the 41 dBsm corner reflector is

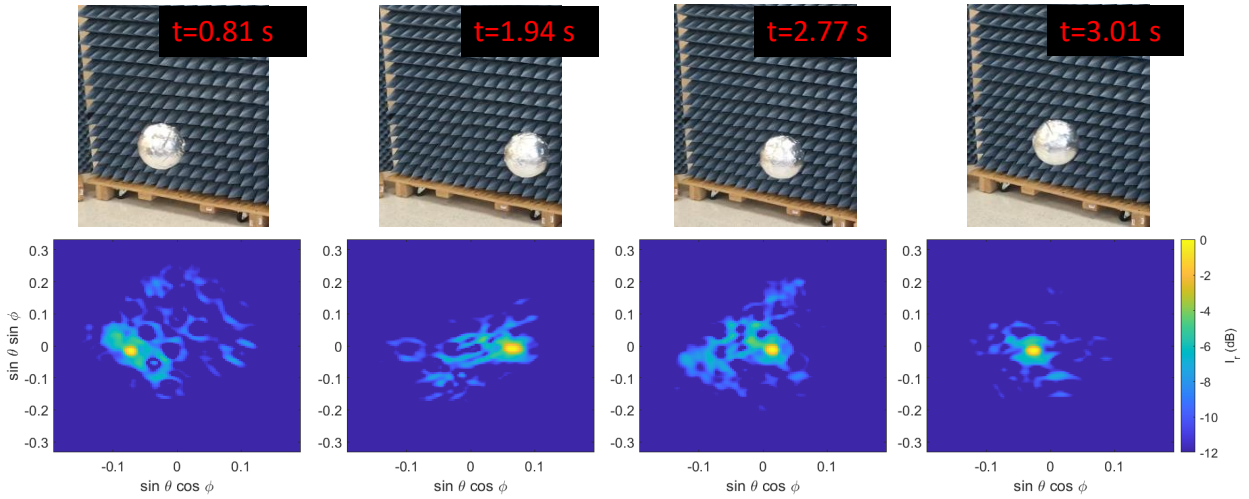

Figure 5.10: (Top) Photographs of the sphere pendulum at different time instances, from left to right, t= 0.81 s, 1.94 s, 2.77 s, 3.01 s. (Bottom) Millimeter-wave non-cooperative image reconstructions of the moving sphere. Image [8] © 2022 IEEE.

held by a person (left), and the 21 dBsm corner reflector is placed on a wooden tripod (right). The passive non-cooperative millimeter-wave image reconstructions can be seen in Fig. 5.11(b), where the two responses can be clearly distinguished. In order to examine the effect of TBP on image reconstruction, horizontal slices at $\sin\theta \sin\phi = 0.02$, are shown in Fig. 5.12 for different TBP values. The bandwidth of the transmission was 10 MHz, and the the integration time was varied to obtain different TBP values. As shown in Sections 3.5 and 3.6, the TBP indicates the correlation that will be seen from closely spaced objects. Thus, smaller values (TBP = 90) result in stronger coupling in nearby points in the scene, which is reflected in Fig. 5.12. For large values (TBP = 9000), the two responses are easily distinguishable.

5.5 Chapter Conclusion

In this chapter, a microwave and a millimeter-wave imaging system that can generate passive imagery of a scene using stray reflections from communication transmitters were demonstrated. No coordination between the receive array and any transmitting node was used, demonstrating the ability to reconstruct images using signals of opportunity. Increased needs for security, autonomous vehicles, and healthcare in an increasingly connected world, are presenting important

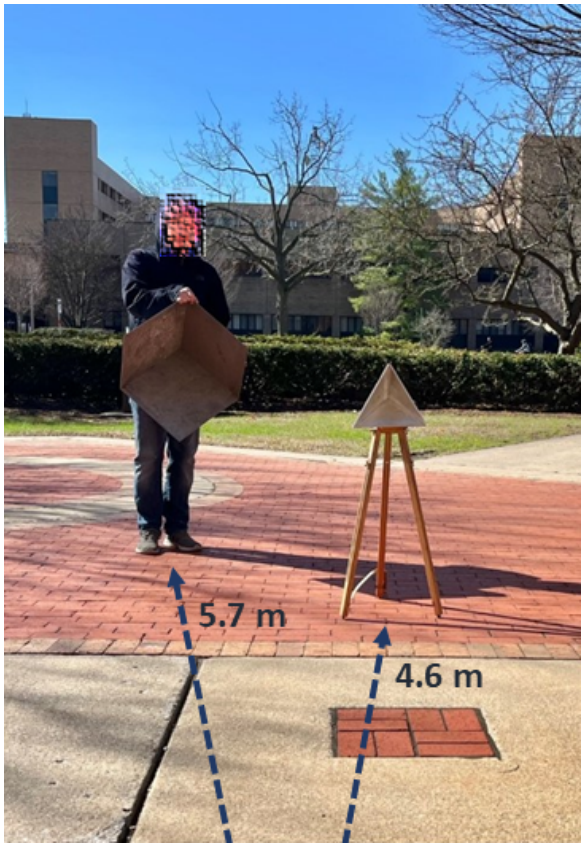

(a)

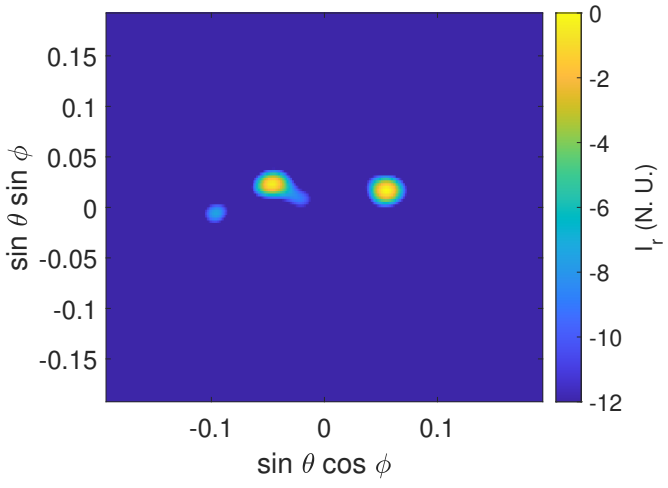

(b)

Figure 5.11: (a) Photograph of the targets used for the outdoor non-cooperative image reconstructions. A person holding a 41 dBsm corner reflector is on the left, and a 21 dBsm corner reflector on a wooden tripod can be seen on the right. (b) Passive non-cooperative millimeter-wave image reconstruction of the two corner reflectors. Image [8] © 2022 IEEE.

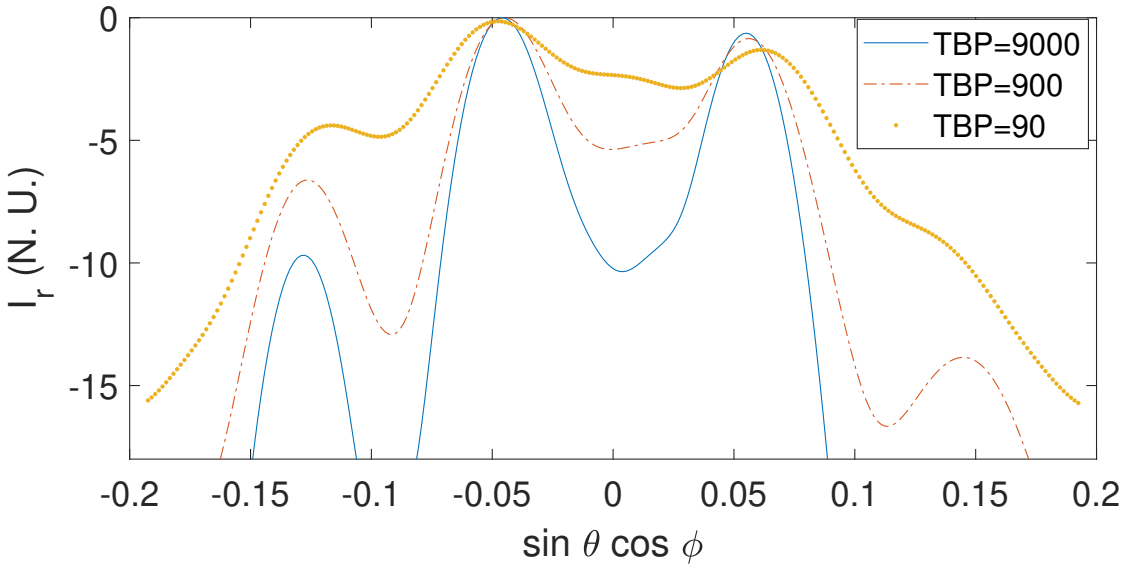

Figure 5.12: One-dimensional slices along $\sin\theta\cos\phi$ for different TBP values. Higher values result in sharper images and lower coupling between spatial reflections. Image [8] © 2022 IEEE.

challenges that need to be addressed. The challenges include limited available bandwidth, expensive hardware, and wireless coexistence. These results can provide a framework for research into future joint sensing and communications in wireless networks addressing the aforementioned challenges.

CHAPTER 6

THREE-DIMENSIONAL ACTIVE INCOHERENT MILLIMETER-WAVE IMAGING

6.1 Three-Dimensional Millimeter-Wave Imaging

In a variety of applications discussed in this dissertation, such as remote sensing [25], automotive radar [101], non-destructive testing [102], and medical imaging [103], the radial distance information is of utmost importance and cannot be acquired using the traditional far-field interferometric image reconstruction process. This is partially related to the lack of synchronization between transmit and receive. In passive interferometric systems, there is no transmitting structure and the signal is generated by the source of interest. In active incoherent millimeter-wave imaging, which is presented in this dissertation, the transmit signal is a broadband noise signal and it is not known to the receiver, so time delay based processing cannot take place. Interferometric arrays can achieve two-dimensional imaging in a planar format, however, to date, the only arrays capable of imaging in three dimensions have been volumetric arrays that are themselves three-dimensional, entailing significant space requirements or systems that operate on the near-field region [104, 105]. Volumetric arrays have significant challenges with coupling and reflections between antenna elements that are spaced in different planes, and operation on the near-field may not be available for many remote sensing and automotive cases.

Active three-dimensional millimeter-wave imaging has traditionally been implemented via mechanically [23] or electrically scanned systems [106]; however, mechanical scanning results in bulky and slow data acquisition, while electrical scanning requires a large number of active components and a large aperture area. Recently, multiple-input multiple-output (MIMO) techniques have been used, which reduce the receive antenna elements by adding an array of transmitters, synthesizing a larger virtual aperture [41, 43]. This can achieve high-resolution three-dimensional imaging but can increase power consumption and system complexity significantly. Compared to these phase-coherent approaches, incoherent millimeter-wave imaging has benefits including re-

laxed synchronization requirements between transmit and receive and that little specific knowledge of the transmit radiation is needed [11, 107].

In this chapter I extend the previously presented work and present three-dimensional active incoherent millimeter-wave (3D AIM) imaging. The concept uses a sparse interferometric planar array that captures the signals from multiple incoherent noise transmitters. The transmit signals are customized in order to obtain three-dimensional incoherent millimeter-wave imaging using a novel noise pulse modulation approach that generates a PSF that is narrow in two dimensions of angle as well as the range dimension. Incoherent imaging requires the received signals to be incoherent in time and space according to the Van Cittert-Zernike theorem [46]. These requirements can be satisfied by collecting multiple noise pulses. The use of noise pulses generally requires sufficient bandwidth in order to achieve a low enough range resolution, which translates to high sampling rate requirements for digital array processing. However, with the approach presented in this chapter, a large number of pulses achieves spatial incoherence even with received pulses that are only a single temporal sample in duration.

6.2 Three-Dimensional Point Spread Function Analysis

Interferometric imagers, both passive and active, do not inherently provide for a mechanism to obtain range information. For automotive applications, down-range measurements should generally be combined with cross-range measurements for accurate environmental sensing. The problem with incoherent planar apertures is that there is not sufficient differentiation of the point spread function along the longitudinal dimension in order to perform three-dimensional far-field imaging. Three-dimensional passive millimeter-wave imaging has been demonstrated before using non-planar passive antenna arrays. Non-planar antenna arrays are in general not very practical due to the large volume that they need to occupy and the concerns for antenna coupling between elements in different planes. The PSF of an interferometric imaging system on the near-field can have some differentiation along the longitudinal dimension, but this is not the case for the far-field. Traditional coherent processing techniques, such as matched filtering between the transmit and

receive signal, are not possible in passive interferometry since no transmit signal is used. In AIM imaging, the specifics of the transmit signals are in generally not known to simplify the hardware requirements; simple noise emitters can be used as long as their statistics are known, precluding matched filtering.

A randomized 77 GHz 24-element antenna array with 1.5 λ minimum spacing in both the x and y dimension is shown in Fig. 6.1(a). The sampling function $S(u, v)$ of the array is shown in 6.1(b). The PSF can be seen in Fig. 6.1(c). The array maximum vertical dimension is shorter than the horizontal dimension, and therefore the 3 dB beamwidth has become larger in the elevation angle Θ and equal to 10.2 degrees, however the 3 dB resolution has improved in the azimuth angle Φ to 1.47 degrees, which is of greater importance in many remote sensing applications. This example shows how apertures with wider horizontal coverage or more antenna elements could easily be designed to further improve the resolution in the spatial dimension of interest.

The approach of pulse modulating the transmitted noise signals to obtain down-range information is discussed. By controlling the timing of the transmitted signal envelopes, which can be done with relatively simple coordination and does not impose spatial coherence, thereby preserving the cross-range incoherence. This process effectively generates two-dimensional interferometric images sequentially in time, each time segment representing a different range bin. The PSF of the system using a Gaussian pulse on the transmitted noise signals is analyzed next. The frequency-domain signal on each transmitter can be written as

$$S_i(f) = e^{\frac{-(f-f_c)^2}{4\delta f^2}} N_i(f) \tag{6.1}$$

where $N_i(f)$ is the spectrum of the ith wideband Gaussian noise signal, f_c is the carrier frequency and δf is the pulse bandwidth. The range resolution Δz along the z dimension can be approximated by the full width at half maximum of a squared Gaussian pulse as

$$\Delta z \approx \frac{2.3548\, c}{2\pi \delta f}. \tag{6.2}$$

By applying this pulse modulation in the PSF of the system in Fig. 6.2 for a bandwidth δf equal to 200 MHz three-dimensional imaging with resolution $\Delta z \approx 56$ cm can be achieved. A

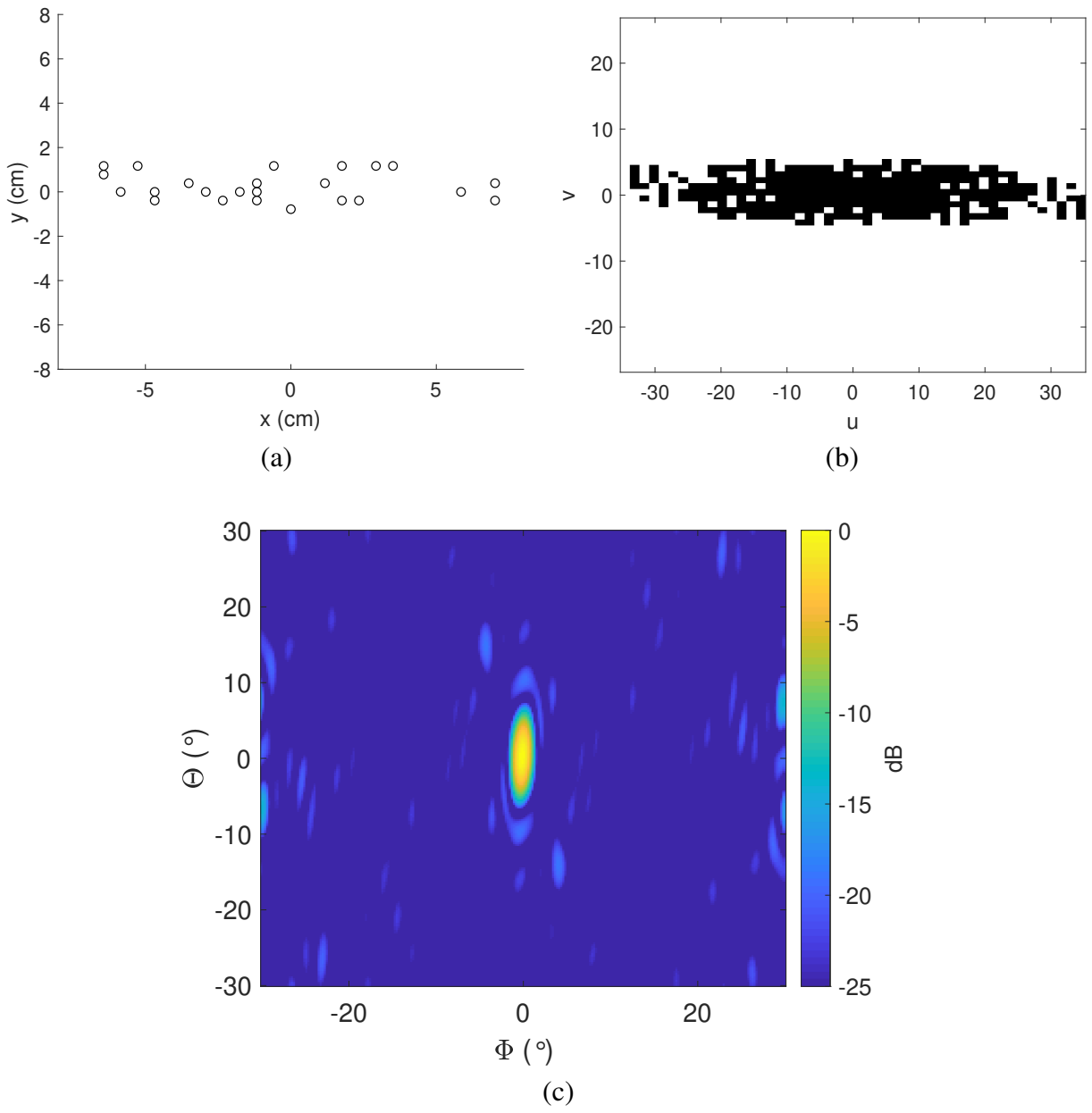

Figure 6.1: (a) Random interferometric antenna array composed of 24 elements. The minimum spacing in both the horizontal and vertical dimension is 1.5 λ. (b) Sampling function of the random 24-element aperture. The sampling function is significantly wider in the u dimension. This is because many applications that require depth information, such as automotive radar, require finer resolution in the azimuth plane than in the elevation.(c) Calculated point spread function of the randomized aperture as a function of the azimuth and elevation angles Φ and Θ. The beamwidth is significantly larger in the elevation plane than in the azimuth plane. Image [14] © 2021 IEEE.

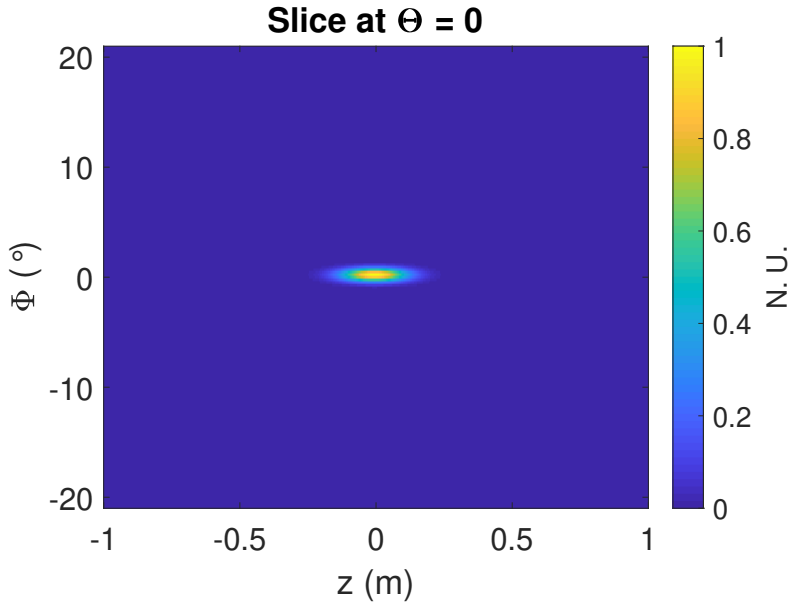

Figure 6.2: Two-dimensional $\Phi - z$ slice of the $\mathrm{PSF}(\Phi, \Theta, z)$ from the randomized aperture in Fig. 6.1(a). The bandwidth of the pulse is 200 MHz. Image [14] © 2021 IEEE.

slice $\Phi - z$ of the point spread function $\mathrm{PSF}(\Phi, \Theta, z)$ for the random array is shown in Fig. 6.2, demonstrating the down-range and cross-range resolution capabilities.

6.3 Interferometric Processing of Noise Pulses

Correlation of the received signals at different antenna elements is the fundamental processing step in interferometric imaging and is usually implemented digitally by means of multiplication and integration. The limitation when digitally sampling noise signals is the need for a sufficiently high TBP to ensure enough temporal samples are obtained to support incoherence in time. This can interpreted as the necessity of a sufficient number of samples within a pulse interval in order to reconstruct the imaging frames. If a low sample rate is used, a long-duration waveform will needed to capture enough samples within the duration of the pulse, and since range resolution is dependent on pulse length, this can correspond to a poor range resolution. The analysis of the PSF in the previous section shows the theoretical differentiation that can be achieved for a certain antenna array, but assumes that the correlation process has already happened for every range bin. This is not that straightforward though, and the theoretical PSF does not define an imaging algorithm

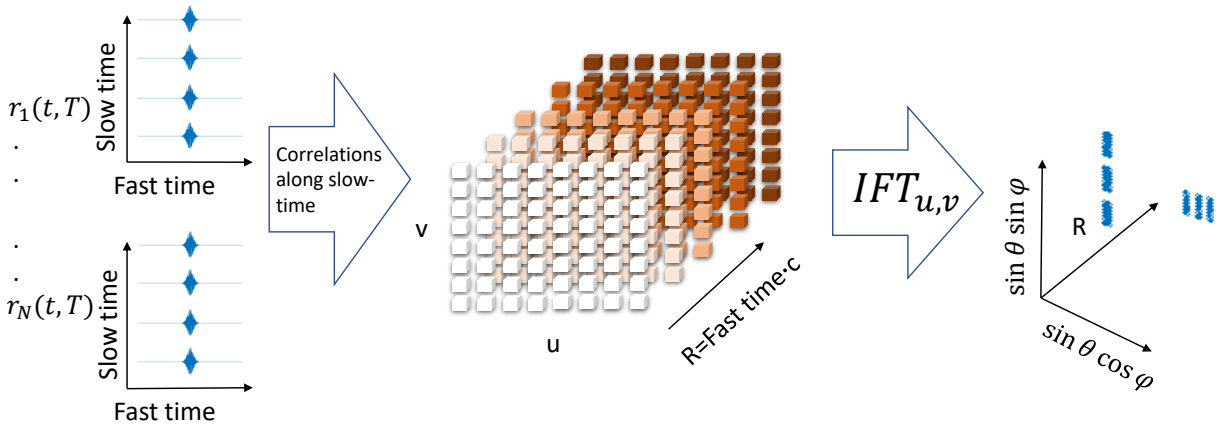

Figure 6.3: Overview of the three-dimensional image reconstruction algorithm. The noise pulses are captured from every receive antenna. The incoherent pulses are chopped and reshaped by using knowledge of the pulse repetition frequency (PRF) and for the ith antenna we have the two-dimensional response $r_i(t,T)$ where t stands for the slow time and T for the fast time. Correlations are taking place along the slow time between every antenna element and then the two-dimensional image slices can be reconstructed at every range bin. Image [15] © 2021 IEEE.

that utilizes actual observations. In order to sample and perform cross-correlation between two Gaussian noise pulses, we need to have a significantly higher sampling rate, so that enough noise samples are captured within the duration of a pulse. To overcome this problem, a train of short-duration noise pulses is used, which over time provide sufficient temporal incoherence, but can still be implemented with short time duration to obtain good range resolution. Because each pulse is incoherent, temporal incoherence is maintained even in the pulses that are only one time sample in duration. The algorithm is summarized in Fig. 6.3. Using knowledge of the pulse repetition frequency (PRF), the train of pulses can be split in intervals of $\frac{1}{PRF}$ and create a two-dimensional matrix where the horizontal dimension refers to range (fast-time) and the vertical dimension refers to the reflections coming from a specific range (slow-time). Cross-correlations along slow-time can then be performed, referring to the same range bin, yielding incoherence in space and time with short duration waveforms. The reflected signal along the slow-time will not be constant even for

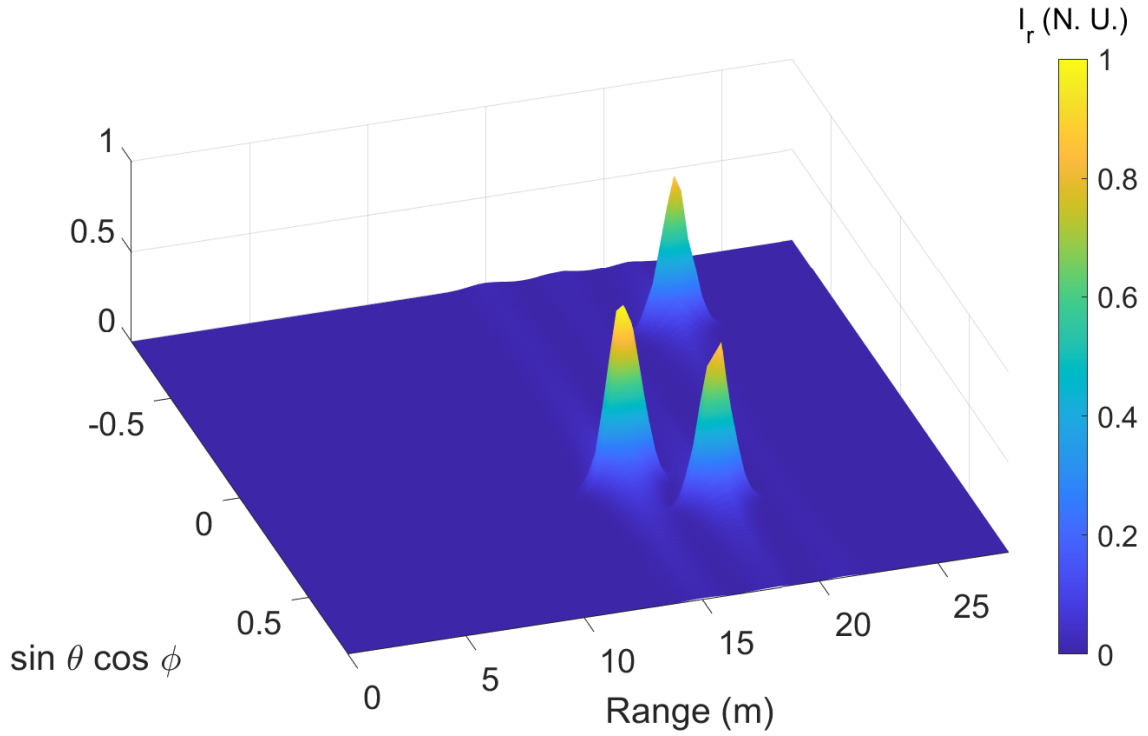

Figure 6.4: Simulation of the reconstruction performed by a linear 30-element antenna array. Using the noise pulse integration algorithm , the down-range information can be retrieved. The carrier frequency was 38 GHz and δf was equal to 50 MHz.

stationary targets because the transmit signal is incoherent noise. The result is a three-dimensional image and can be written as

$$I_r(\alpha, \beta, r = R) = \sum_{n}^{N} \sum_{m}^{M} \mathcal{V}_s(u_n, v_m, r = R) e^{-j2\pi(u_n\alpha + v_m\beta)} \tag{6.3}$$

where $\mathcal{V}_s(u_n, v_m, r = R)$ represents the visibility samples that were obtained from correlation along slow-time at the range bin $r = R$.

Simulations of this algorithm took place in MATLAB using a linear antenna array with 100 elements in $\lambda/2$ spacings. The array carrier frequency was 38 GHz and δf was equal to 50 MHz. Three targets were located at distances of 15, 18, and 21 m from the array and their residing angle was 16.6, 27.5, and -34.3 degrees away from broadside, respectively. The targets were reflecting the noise pulses from the transmitters and no synchronization took place between transmit and receive. Their image reconstruction as a function of the direction cosine along azimuth (cross-range) and down-range can be seen in Fig. 6.4. The three targets can be clearly differentiated.

Figure 6.5: Two corner reflectors in a semi-anechoic environment used as the experimental three-dimensional measurement scene. Image [15] © 2021 IEEE.

6.4 Experimental Three-Dimensional Imaging Results

Next, the three-dimensional image reconstruction algorithm was experimentally validated with measurements conducted in a semi-anechoic environment using two corner reflectors as shown in Fig. 6.5. The triangular corner reflector was mounted on a wooden tripod and was located at a distance of 1.8 m from the array, while the trihedral corner reflector was located at a distance of 3 m from the array. The three-dimensional active incoherent millimeter-wave imaging system is shown in Fig. 6.6, where the 24 receive antenna elements in an asymmetric Y formation, described in Chapter 4, were combined with four noise transmitters which illuminated the scene with the Gaussian-envelope noise pulses. The noise was generated using calibrated noise sources that were amplified at baseband and upconverted using an ADI HMC6787ALC5A upconverter using

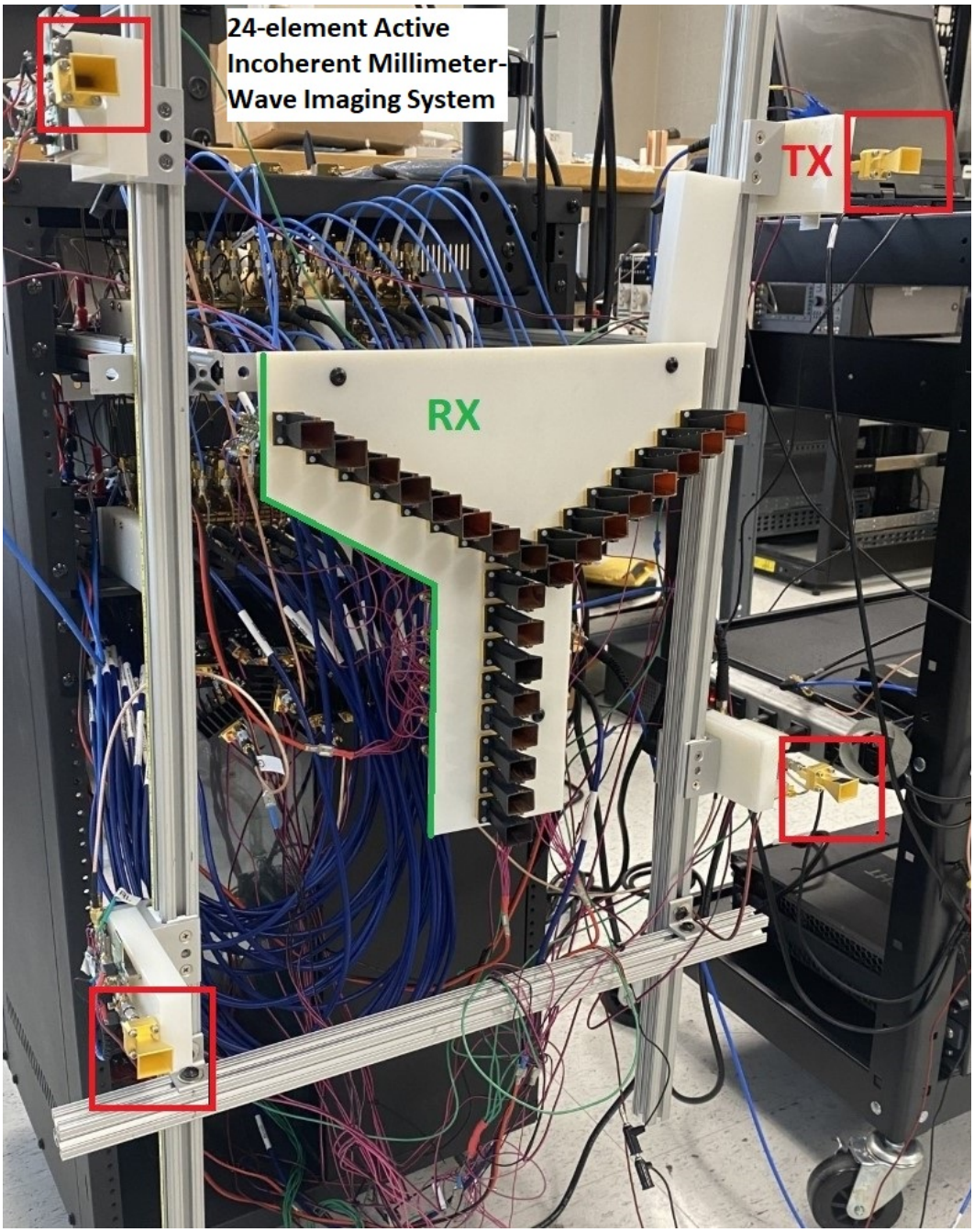

Figure 6.6: Photograph of the 3D AIM 38 GHz imaging array. The 4 noise transmitters (red) illuminate the scene using pulsed noise signals, and the 24 receivers (green) capture the reflections from the scene. Image [15] © 2021 IEEE.

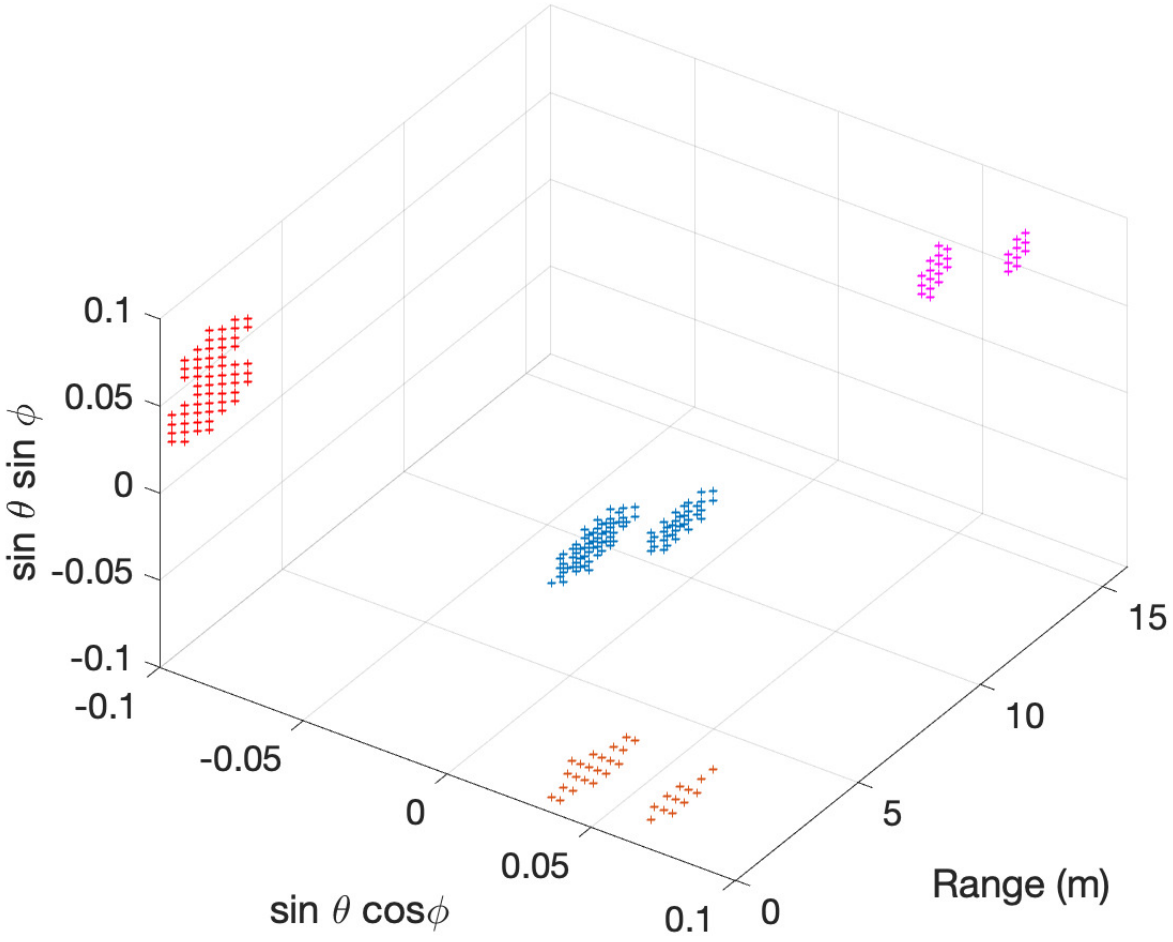

Figure 6.7: Three-dimensional imagery results of two corner reflectors shown with blue color. Red, magenta, and orange colors represent their projections in the different imaging planes. Image [15] © 2021 IEEE.

a 19 GHz Local Oscillator (LO). The pulses were implemented by modulating the 19 GHz LO on the upconverter with a Gaussian 40 MHz pulse generated using a Keysight M8190 Arbitrary Waveform Generator. For $\delta f = 40$ MHz, the resolution $\Delta z \approx 2.8$ m from (6.2), although in this particular system it is the sampling rate that is the limiting factor which is equal with 100 MSamples/s. The 24 receive signals were amplified at 38 GHz by 23 dB gain ADI HMC1040LP3CE low-noise amplifiers at the output of the antennas and then downconverted using ADI HMC6789BLC5A downconverters. Both transmit and receive elements employed 15 dBi horn antennas. The three-

dimensional experimental measurements of the two corner reflectors can be seen in Fig. 6.7, where the two targets are showing sufficient differentiation in azimuth, elevation and range dimensions, demonstrating the 3D AIM concept. The actual target responses are shown with blue color, while their projections in the three planes are shown with red, magenta, and orange.

6.5 Chapter Conclusion

In this chapter, the first experimental measurements of three-dimensional active incoherent millimeter-wave imaging using a two-dimensional planar antenna array is presented. An analysis of the three-dimensional image formation algorithm is presented, along with a way to bypass the typical high sampling requirements, and the approach using experimental measurements from a 38 GHz incoherent imaging array that uses incoherent noise pulses.

Although the results presented in this chapter are proof-of-concept, they present incoherent imaging that do not require phase-locking between transmit and receive. This may pave the way for larger-scale incoherent systems that can demonstrate three-dimensional imagery without wavelength level synchronization. Synchronization on the pulse-envelope level needs to take place but this is significantly easier.

CHAPTER 7

CONCLUSION

Millimeter-wave imaging is an emerging area which holds significant potential for gaining new knowledge and developing new technologies. This dissertation investigated microwave and millimeter-wave imaging architectures that can be implemented using low-cost and commercially available hardware and can operate at video-rate or higher imaging speeds. While the challenges of microwave and millimeter-wave imaging are numerous, including coarse spatial resolution or strong specular reflections, this dissertation addressed the problem of slow imaging speed and high system cost due to the large number of antennas needed. Interferometry has been a unique starting point for this dissertation, which is greatly underexplored in millimeter-wave imaging research outside the field of radio astronomy.

I investigated the problem of designing a space-time incoherent transmitter that can satisfy the Van Cittert-Zernike theorem requirements. In this setting, I discussed the problem of coherence in the cross-range and longitudinal dimensions. One interesting and easily interpretable result from my analysis is that when using N incoherent sources, partial coherence regions of $1/N$ can appear in far-field ranges. I also developed new metrics and measurements to simulate and evaluate the incoherence of a transmitter in both the spatial and temporal domain. After investigating how coherence propagates in the spatial domain, this dissertation includes experimental demonstrations of active incoherent microwave and millimeter-wave imagery. Imaging performance with regards to array sparsity is discussed, which shows that very sparse antenna arrays can achieve very good imaging results by utilizing random-thinning and minimum redundancy layouts. An analysis of antenna element failures and how they affect the quality of the image reconstruction is included using simulated and experimental data. I discuss a way to calibrate an incoherent antenna array, from a system-level perspective, that does not need any assumption regarding the imaging scene. The design and build of a high-speed incoherent digital array imager is also discussed. By focusing on both the hardware and software level, a frame-rate of 652 fps is achieved. Experimental

measurements of high-speed millimeter-wave video are included.

One significant advantage of incoherent imaging systems is that transmitters and receivers do not need to be phase locked or synchronized. This dissertation examined how stray communication signals in an environment can be used for imaging. Experimental image reconstructions are obtained using 5.5 GHz 16-QAM and 5G 38 GHz signals. Finally, it is challenging for incoherent imaging systems to obtain three-dimensional imagery because of the lack of synchronization between transmit and receive. This dissertation addresses this problem by using a novel pulse modulation and a new interferometric image formation algorithm. Experimental imagery using the proposed algorithm is also shown.

There is still considerable room for future research and millimeter-wave imaging can be a quite involved topic. Imaging at millimeter-wave frequencies manifests specularity. Strong specular reflections at specific directions can result in loss of information when there are no receivers present at the specific directions. Synthetic aperture and holographic techniques can illuminate the scene and capture reflections from multiple locations, but the compact and sparse array designs, that were presented in this dissertation, collect significantly less spatial samples. One area for future work will be to address the specularity issue by exploiting dynamics and new imaging architectures. Additionally, the problem of coherence was investigated, but there is still room for improvement especially on the far-field case. New incoherent transmit architectures can help introduce additional spatial variations and although noise transmitters satisfy the incoherence requirements, they are not power efficient and entail significant bandwidth occupation. Future work will address the optimization of power spectral density and spectral allocation such that the next generation of active incoherent imaging systems will show reduced coherence with optimized power consumption and less transmit bandwidth.

In summary, this dissertation can affect the millimeter-wave imaging state of the art in many promising ways. Using the presented results, high-speed millimeter-wave imaging can take place using sparse antenna arrays and incoherent signal transmission. Large-scale imaging systems with relaxed synchronization requirements between the transmit and receive hardware can achieve

three-dimensional imagery. Future wireless networks can utilize a dense electromagnetic environment and perform imaging in order to identify blockage and other issues. Finally, by investigating the properties of incoherence, the work presented in this dissertation can pave the way for advanced imaging and sensing modalities with simplified and reduced hardware requirements.

APPENDICES

APPENDIX A

IMAGE RECONSTRUCTION USING INTERFEROMETRIC ANTENNA ARRAYS IN THE SPATIAL AND SPATIAL FREQUENCY DOMAIN

```
clear all
close all

%%image

%% YOU CAN CHOOSE IMAGE 1 IS AN "E" CHARACTER AND IMAGE 2 IS A RECTANGLE

imgg=1;
% imgg=2;
image=zeros(256,256);

if imgg == 1
image(128,128-20:128+20)=1;
image(108,128-20:128+20)=1;
image(148,128-20:128+20)=1;
image(108:148,128-20)=1;
elseif imgg == 2
image(128-25:128+25,128-25:128+25)=1;
end

four_image=ifftshift(ifft2(image));


%%ARRAY LOCATIONS IN INTEGERS SO THAT THEY CAN BE USED AS MATRIX INDEXES
loc_x=2*[8 7 6 5 4 3 2 1 0 0 0 0 0 0 0 0 0 -1 -2 -3 -4 -5 -6 -7];
loc_y=2*[8 7 6 5 4 3 2 1 -14 -12 -10 -8 -6 -4 -2 0 2 3 4 5 6 7 8 9 ];

locx2=loc_x+16;
```

```
locy2=loc_y+30;


for  i=1:24

        array_loc(locy2(i),locx2(i))=1;

end

sincos=-1:2/255:1;
sinsin=-1:2/255:1;

%%SPATIAL FREQUENCY DIMENSIONS
u=sqrt(3)/2*(min(loc_x)-max(loc_x)):sqrt(3)/2:-sqrt(3)/2*(min(loc_x)-max(loc_x));

v=0.5*(min(loc_y)-max(loc_y)):0.5:-0.5*(min(loc_y)-max(loc_y));


%%AUTOCORRELATION FOR FINDING SAMPLING FUNCTION FROM ARRAY LAYOUT

S1=xcorr2(array_loc);
S2=padarray(S1,[(256-94)/2-1  (256-62)/2-1],0,'both');
S2(256,:)=0;
S2(:,256)=0;

%%PSF CALCULATION THROUGH AN INVERSE FOURIER TRANSFORM
psf2=abs(ifftshift(ifft2(S2,256,256)));

%%SPATIAL FREQUENCY RECONSTRUCTION USING ELEMENT BY ELEMENT MULTIPLICATION
%%WITH THE SAMPLING FUNCTION
recSam2=abs(ifftshift(ifft2(four_image.*S2,256,256)));

%%SPATIAL DOMAIN RECONSTRUCTION USING SPATIAL CONVOLUTION WITH THE PSF
```

```
recPsf2=conv2(psf2,image,'same');

figure(2)

x0=100;
y0=100;
width=950;
height=550;
set(gcf,'position',[x0,y0,width,height])

subplot(2,3,1);
scatter(sqrt(3)/2*loc_x,1/2*loc_y,'k');
% axis off
axis equal
xlabel('x (\lambda)')
ylabel('y (\lambda)')
title('(a) Array Locations')
xlim([-15 15])
ylim([-15 11])
set(gca,'FontSize',14);

subplot(2,3,2);
imagesc(u,v,S1)
colorbar
axis xy
title('(c) Sampling Function')
xlabel('u')
ylabel('v')
h = colorbar;
ylabel(h, 'A. U.')
set(gca,'FontSize',14);

subplot(2,3,3);
```

```
imagesc(sinsin,sincos,fliplr(recSam2/max(recSam2(:))))
colorbar
axis xy
title('(e) Spatial Frequency Reconstruction')
xlabel('sin \theta cos \phi')
ylabel('sin \theta sin \phi')
h = colorbar;
ylabel(h, 'N. U.')
set(gca,'FontSize',14);

subplot(2,3,4)
imagesc(sinsin,sincos,image);
axis xy
title('(b) Original Image')
xlabel('sin \theta cos \phi')
ylabel('sin \theta sin \phi')
set(gca,'FontSize',14);

subplot(2,3,5);
imagesc(sinsin,sincos,psf2/max(psf2(:)))
colorbar
axis xy
title('(d) Point Spread Function')
xlabel('sin \theta cos \phi')
ylabel('sin \theta sin \phi')
xlabel('sin \theta cos \phi')
ylabel('sin \theta sin \phi')
h = colorbar;
ylabel(h, 'N. U')
set(gca,'FontSize',14);

subplot(2,3,6);
imagesc(sinsin,sincos,recPsf2/max(recPsf2(:)))
```

```
colorbar
axis xy
title('(f) Spatial Domain Reconstruction')
xlabel('sin \theta cos \phi')
ylabel('sin \theta sin \phi')
h = colorbar;
ylabel(h, 'N. U.')
set(gca,'FontSize',14);
```

APPENDIX B

EVALUATION OF SPATIAL COHERENCE ALONG THE CROSS-RANGE DIMENSION

```
% close all
clear all

%CARRIER FREQUENCY
f=37e9;

%%BANDWIDTH BIN
df=f/1000;

%SAMPLING FREQUENCY
fs=10*f;
ts=1/fs;

%%SPEED OF LIGHT
c=3e8;

%%WAVELENGTH
lambda=c/f;

%%TOTAL TIME AND TIME VECTOR
T=10e-9;
t=0:ts:T;



%%COURANT STABILITY CONDITION AND CREATING THE GRID

S=1/(2^0.5);
dx=0.5*c*ts/S;
```

```
dy=dx;
x=-100e-2:dx:100e-2;
xx=repmat(x,length(x),1);
y=-100e-2:dx:100e-2;



yy=260e-2;


x1=-10e-2;
y1=0;
x2=10e-2;
y2=0;
x3=15e-2;
y3=0;
x4=-4;
y4=0;
R=sqrt((xx^2+yy^2));
R1=sqrt((x-x1).^2+(yy-y1)^2);
R2=sqrt((x-x2).^2+(yy-y2)^2);
R3=sqrt((x-x3).^2+(yy-y3)^2);
R4=sqrt((x-x4).^2+(yy-y4)^2);



%%RUNNING THROUGH THE TIME STEPS AND INTEGRATING OVER THE BANDWIDTH


for i=1:length(t)
    for f=f-1*df:df:f+1*df
    f1=(1+0.1*randn)*f;
    f2=(1+0.1*randn)*f;
    f3=(1+0.1*randn)*f;
    f4=(1+0.01*randn)*f;


    E=exp(1i*2*pi*(f1)*t(i))*sin(atan2((yy-y1),(x-x1)))...
```

```
    .*exp(1i*2*pi*(f1)*(1/c*R1))./R1+...
    exp(1i*2*pi*(f2)*t(i))*sin(atan2((yy-y2),(x-x2)))...
    .*exp(1i*2*pi*(f2)*(1/c*R2))./R2+...
    exp(1i*2*pi*(f3)*t(i))*sin(atan2((yy-y3),(x-x3)))...
    .*exp(1i*2*pi*(f3)*(1/c*R3))./R3;


a(i,:)=E(end,:);
    end
end

%%REMOVE THE MEAN AND CORRELATE EVERY POINT IN THE LINE WITH ITSELF

a=(a-mean(a))./max(abs(a-mean(a)));
corre=a'*a;
corre=corre./max(abs(corre));

%%PLOT THE MUTUAL COHERENCE MATRIX
figure(2),imagesc(x,y,(abs(corre)));
colorbar
xlabel('x (m)')
ylabel('x (m)')

h = colorbar;
ylabel(h, '\gamma (N. U.)')
 set(gca,'FontSize',14);
```

APPENDIX C

EVALUATION OF LONGITUDINAL COHERENCE

```
%%LONGITUDINAL COHERENCE CALCULATION SCRIPT

close all
clear all
%%CARRIER FREQUENCY
f=38e9;

%%BANDWIDTH BIN
df=f/1000;

%%SAMPING FREQUENCY
fs=10*f;

%% TIME INCREMENTS
ts=1/fs;

%%WAVEFRONT PROPAGATION SPEED
c=3e8;

%%WAVELENGTH
lambda=c/f;

%%OBSERVATION TIME
T=1*1e-9;

%%TIME VECTOR
t=0:ts:T;

%%COURANT STABILITY CONDITION AND CREATING THE GRID
```

```
S=1/(2^0.5);
dx=0.5*c*ts/S;
dy=dx;


x=0;
xx=repmat(x,length(x),1);
y=0:dx:50e-2;


yy=500e-2;


x1=-50e-2;
y1=0;
x2=50e-2;
y2=0;
x3=35e-2;
y3=0;
x4=-40e-2;
y4=0;
R=sqrt((xx^2+yy^2));

%%DISTANCE OF EVERY POINT FROM THE TWO TRANSMIT LOCATIONS
R1=sqrt((x-x1)^2+(y-y1).^2);
R2=sqrt((x-x2)^2+(y-y2).^2);

for i=1:length(t)
    for f=f-1*df:df:f+1*df
        %%RANDOM INSTANTANEOUS FREQUENCY OF THE TRANSMITTERS
    f1=(1+0.1*randn)*f;
    f2=(1+0.1*randn)*f;
```

```
    %%ELECTRIC FIELD CALCULATION
E=exp(1i*2*pi*(f1)*t(i))*sin(atan2((y-y1),(x-x1)))...
    .*exp(1i*2*pi*(f1)*(1/c*R1))...
    ./R1+exp(1i*2*pi*(f2)*t(i))*sin(atan2((y-y2),(x-x2)))...
    .*exp(1i*2*pi*(f2)*(1/c*R2))./R2;

a(i,:)=E(end,:);
     end
end

%%NORMALIZING
a=(a-mean(a))./max(abs(a-mean(a)));

%%COHERENCE CALCULATION
corre=a'*a;
corre=corre./max(abs(corre));
figure(2),imagesc(y,y,(abs(corre)));
colorbar
xlabel('y (m)')
ylabel('y (m)')

h = colorbar;
ylabel(h, '\gamma (N. U.)')
 set(gca,'FontSize',14);

%PRINT TBP VALUE
TBP=0.5*fs*T
```

APPENDIX D

CALIBRATION OF A LINEAR ARRAY USING REDUNDANT BASELINES

```
%%CALIBRATION SCRIPT FOR AN N-ELEMENT LINEAR ARRAY

clear all;
close all;

%%NUMBER OF ANTENNA ELEMENTS  - THIS NUMBER CAN CHANGE
N=21;

%%LOCATIONS OF ANTENNA ELEMENTS  ( UNIFORM LINEAR ARRAY)
loc=1:N;

%%RANDOM PHASE AND AMPLITUDE CORRESPONDING TO ANTENNA ELEMENT IMPERFECTIONS

gain_complex=exp(1*((rand(1,N))-0.5)+1i*0.5*pi*(rand(1,N)-0.5));

int=zeros(1,2*N+1);
intt=int;
for i=1:N-1
    for j=i+1:N




    int(loc(j)-loc(i)+N)=gain_complex(i)*conj(gain_complex(j));
    %% CORRELATIONS FOR VISIBILITIES
    %THESE LOOPS DO NOT CAPTURE EVERYTHING BUT IT IS RELATED WITH HOW WE
    %SET UP THE LEAST SQUARES PROBLEM

     u_obs(i,j)= gain_complex(i)*conj(gain_complex(j));
     %%COLLECT THE REDUNDANT VISIBILITIES
```

```
    end
end


for i=1:N
    for j=1:N

       %%capturing all the redundant visibility points

    intt(loc(j)-loc(i)+N)= gain_complex(i)*conj(gain_complex(j));


    end
end

sin=-1:2/(255):1;

beam_uncal=ifftshift(ifft(intt,256));
% figure(1),plot(sin,abs(beam_uncal)/max(abs(beam_uncal)));
% figure(19),plot(1:2*N+1,abs(intt),1:2*N+1,unwrap(angle(intt)));


u_o2=(u_obs)';
b_obs=u_o2(:);
%%TURNING ALL THE VISIBILITY POINTS INTO A VECTOR
%%TO DO LEAST SQUARE ESTIMATION
b_obs=nonzeros(b_obs);

%%CONSTRUCT THE GAIN MATRIX

k=zeros(1,N);
```

```
k(1)=1;
for i=2:N-1
    k(i)=k(i-1)+(N+1-i);
 end
% k(N)=N*(N-1)*0.5;
for i=1:N-1

    Ag(k(i):k(i+1)-1,i)=1; %%FIRST ANTENNA ELEMENT

    for j=k(i):k(i+1)-1
      Ag(j,i+j-k(i)+1)=1; %%SECOND ANTENNA ELEMENT
      Ag(j,N+j-k(i)+1)=1; %%TRUE VISIBILITIES
    end
end

Ag(end+1,N-1:N+1)=1;  %%CONDITION THAT SUM ( GAINS) = 0


Ag(end+1,1:N)=1;

b_g=log(abs(b_obs));
b_g(end+1)=0;
% b_g(N*(N-1)*0.5+1)=0; %%this is just because log(0)=-inf.
sol_g=(Ag'*Ag)\Ag'*b_g;  %%LEAST-SQUARES ESTIMATION


figure(1),imagesc(Ag);
colorbar
title('Gain Matrix')
%%PLOT THE GAIN MATRIX.
%%THE ROWS REPRESENT THE NUMBER OF EQUATIONS WE HAVE.
%%THE FIRST N COLUMNS REPRESENT THE ANTENNA ELEMENTS
%%AND THE REST REPRESENT THE TRUE VISIBILITIES
```

```
%%CONSTRUCT THE PHASE MATRIX
for i=1:N-1

    Ap(k(i):k(i+1)-1,i)=1; %%FIRST ANTENNA ELEMENT

    for j=k(i):k(i+1)-1
      Ap(j,i+j-k(i)+1)=-1; %%SECOND ANTENNA ELEMENT
      %%(MINUS BECAUSE OF CORRELATION)
      Ap(j,N+j-k(i)+1)=1;  %%TRUE VISIBILITIES
    end
end

Ap(end+1,N-1:N+1)=[1 -1 1];
Ap(end+1,1:N)=1; %% SUMMATIONS OF ALL PHASE SHOULD BE ZERO
Ap(end+1,1:N)= -(N-1)/2: (N-1)/2;    %%INTRODUCE THE ARRAY GEOMETRY




 b_p=unwrap(angle((b_obs)));  %%UNWRAP THE PHASES
 b_p(end+1)=0;
 b_p(end+1)=0;
figure(2),imagesc(Ap);
colorbar
title('Phase Matrix')
%%PLOT THE PHASE MATRIX.
%%THE ROWS REPRESENT THE NUMBER OF EQUATIONS WE HAVE
%%THE FIRST N COLUMNS REPRESENT THE ANTENNA ELEMENTS
%% AND THE REST REPRESENT THE TRUE VISIBILITIES
```

```
sol_p=(Ap'*Ap)\Ap'*b_p;   %% LEAST-SQUARES ESTIMATION

c=exp(-1*sol_g+1i*sol_p);

weight2=c(1:N); %%GRAB THE WEIGHTS ( FIRST N ELEMENTS).
%%THE REST ARE TRUE VISIBILITIES
int2=zeros(1,2*N+1);
% intt2=int;


for i=1:N
    for j=1:N



    int2(loc(j)-loc(i)+N)= weight2(i)*conj(weight2(j))*...
   (gain_complex(i)*conj(gain_complex(j)));
   %%CALIBRATE USING WEIGHT MULTIPLICATION

    end
end

beam_cal=ifftshift(ifft(int2,256));
figure(3),plot(sin,abs(beam_uncal)/max(abs(beam_uncal)),...
    '--',sin,abs(beam_cal)/max(abs(beam_cal)));
xlabel('sin(\theta)')
ylabel('N. U.')
legend('"Dirty" Beam', 'Calibrated Beam')
set(gca,'fontsize', 12);
```

BIBLIOGRAPHY

BIBLIOGRAPHY

[1] Stavros Vakalis, Daniel Chen, and Jeffrey A. Nanzer. Millimeter-wave imaging at 652 frames per second. *IEEE Journal of Microwaves*, 1(3):738–746, 2021.

[2] Jeffrey A. Nanzer. Millimeter-wave interferometric imaging sensors. In *SENSORS, 2013 IEEE*, pages 1–4, 2013.

[3] S. Vakalis and J. A. Nanzer. Microwave imaging using noise signals. *IEEE Transactions on Microwave Theory and Techniques*, 66(12):5842–5851, Dec 2018.

[4] S. Vakalis and J. A. Nanzer. Analysis of array sparsity in active incoherent microwave imaging. *IEEE Geoscience and Remote Sensing Letters*, 17(1):57–61, Jan 2020.

[5] S. Vakalis, L. Gong, and J. A. Nanzer. Imaging with wifi. *IEEE Access*, 7:28616–28624, 2019.

[6] Stavros Vakalis, Daniel Chen, and Jeffrey A. Nanzer. Toward space–time incoherent transmitter design for millimeter-wave imaging. *IEEE Antennas and Wireless Propagation Letters*, 19(9):1471–1475, 2020.

[7] Stavros Vakalis and Jeffrey A. Nanzer. The near field effect in transmitter design for incoherent millimeter-wave imaging. In *2021 XXXIVth General Assembly and Scientific Symposium of the International Union of Radio Science (URSI GASS)*, pages 01–04, 2021.

[8] Stavros Vakalis, Serge Mghabghab, and Jeffrey A. Nanzer. Fourier domain millimeter-wave imaging using non-cooperative 5g communications signals. *IEEE Transactions on Antennas and Propagation, accepted*, 2022.

[9] S. Vakalis and J. A. Nanzer. Analysis of element failures in active incoherent microwave imaging arrays using noise signals. *IEEE Microwave and Wireless Components Letters*, 29(2):161–163, Feb 2019.

[10] S. Vakalis, L. Gong, J. Papapolymerou, and J. Nanzer. 40-ghz active interferometric imaging with noise transmitters. In *European Radar Conference (EuRAD)*, October 2019.

[11] Stavros Vakalis, Liang Gong, Yuxiao He, John Papapolymerou, and Jeffrey A. Nanzer. Experimental demonstration and calibration of a 16-element active incoherent millimeter-wave imaging array. *IEEE Transactions on Microwave Theory and Techniques*, 68(9):3804–3813, Sep. 2020.

[12] Jorge R. Colon-Berrios, Stavros Vakalis, Daniel Chen, and Jeffrey A. Nanzer. Incoherent point spread function estimation and multipoint deconvolution for active incoherent millimeter-wave imaging. *IEEE Microwave and Wireless Components Letters*, 2022.

[13] Stavros Vakalis, Serge Mghabghab, and Jeffrey A. Nanzer. Passive non-cooperative millimeter-wave imaging using 5g signals of opportunity. In *2021 IEEE MTT-S International Microwave Symposium (IMS)*, pages 549–552, 2021.

[14] Stavros Vakalis and Jeffrey A. Nanzer. Towards three-dimensional active incoherent millimeter-wave imaging. In *2021 IEEE International Conference on Autonomous Systems (ICAS)*, pages 1–5, 2021.

[15] Stavros Vakalis, Jorge R. Colon-Berrios, and Jeffrey A. Nanzer. Passive non-cooperative millimeter-wave imaging using 5g signals of opportunity. In *2022 IEEE MTT-S International Microwave Symposium (IMS)*, 2022.

[16] S. Hu, E.A. Hoffman, and J.M. Reinhardt. Automatic lung segmentation for accurate quantitation of volumetric x-ray ct images. *IEEE Transactions on Medical Imaging*, 20(6):490–498, 2001.

[17] A. Reigber and A. Moreira. First demonstration of airborne sar tomography using multibaseline l-band data. *IEEE Transactions on Geoscience and Remote Sensing*, 38(5):2142–2152, 2000.

[18] Mickael Tanter and Mathias Fink. Ultrafast imaging in biomedical ultrasound. *IEEE Transactions on Ultrasonics, Ferroelectrics, and Frequency Control*, 61(1):102–119, 2014.

[19] K.A. Dines and R.J. Lytle. Computerized geophysical tomography. *Proceedings of the IEEE*, 67(7):1065–1073, 1979.

[20] Christiaan Huygens. *Traité de la lumière* . Chez Pierre vander Aa, marchand libraire, 1690.

[21] James Clerk Maxwell. *A Treatise on Electricity and Magnetism*, volume 1 of *Cambridge Library Collection - Physical Sciences*. Cambridge University Press, 2010.

[22] H. Hertz. Ueber die ausbreitungsgeschwindigkeit der electrodynamischen wirkungen. *Annalen der Physik und Chemie*, 270(7):551–569, 1888.

[23] D. M. Sheen, D. L. McMakin, and T. E. Hall. Three-dimensional millimeter-wave imaging for concealed weapon detection. *IEEE Transactions on Microwave Theory and Techniques*, 49(9):1581–1592, Sep. 2001.

[24] R. Appleby and H. B. Wallace. Standoff detection of weapons and contraband in the 100 ghz to 1 thz region. *IEEE Transactions on Antennas and Propagation*, 55(11):2944–2956, Nov 2007.

[25] C. S. Ruf, C. T. Swift, A. B. Tanner, and D. M. Le Vine. Interferometric synthetic aperture microwave radiometry for the remote sensing of the earth. *IEEE Transactions on Geoscience and Remote Sensing*, 26(5):597–611, Sep. 1988.

[26] E. J. Bond, Xu Li, S. C. Hagness, and B. D. Van Veen. Microwave imaging via space-time beamforming for early detection of breast cancer. *IEEE Transactions on Antennas and Propagation*, 51(8):1690–1705, Aug 2003.

[27] M. Bassi, M. Caruso, M. S. Khan, A. Bevilacqua, A. D. Capobianco, and A. Neviani. An integrated microwave imaging radar with planar antennas for breast cancer detection. *IEEE Transactions on Microwave Theory and Techniques*, 61(5):2108–2118, May 2013.

[28] F. Zidane, J. Lanteri, J. Marot, L. Brochier, N. Joachimowicz, H. Roussel, and C. Migliaccio. Nondestructive control of fruit quality via millimeter waves and classification techniques: Investigations in the automated health monitoring of fruits. *IEEE Antennas and Propagation Magazine*, 62(5):43–54, 2020.

[29] J. A. Nanzer. *Microwave and Millimeter-Wave Remote Sensing for Security Applications*. Artech House, 2012.

[30] J. J. Lynch, H. P. Moyer, J. H. Schaffner, Y. Royter, M. Sokolich, B. Hughes, Y. J. Yoon, and J. N. Schulman. Passive millimeter-wave imaging module with preamplified zero-bias detection. *IEEE Transactions on Microwave Theory and Techniques*, 56(7):1592–1600, July 2008.

[31] R. C. Hansen. *Phased Array Antennas*. Wiley-Interscience, 2009.

[32] A. Clemente, L. Dussopt, R. Sauleau, P. Potier, and P. Pouliguen. Wideband 400-element electronically reconfigurable transmitarray in x band. *IEEE Transactions on Antennas and Propagation*, 61(10):5017–5027, Oct. 2013.

[33] Mohammadreza F. Imani, Jonah N. Gollub, Okan Yurduseven, Aaron V. Diebold, Michael Boyarsky, Thomas Fromenteze, Laura Pulido-Mancera, Timothy Sleasman, and David R. Smith. Review of metasurface antennas for computational microwave imaging. *IEEE Transactions on Antennas and Propagation*, 68(3):1860–1875, 2020.

[34] D. A. Scribner, M. R. Kruer, and J. M. Killiany. Infrared focal plane array technology. *Proceedings of the IEEE*, 79(1):66–85, Jan 1991.

[35] Georgios C. Trichopoulos, H. Lee Mosbacker, Don Burdette, and Kubilay Sertel. A broadband focal plane array camera for real-time thz imaging applications. *IEEE Transactions on Antennas and Propagation*, 61(4):1733–1740, 2013.

[36] John Hunt, Tom Driscoll, Alex Mrozack, Guy Lipworth, Matthew Reynolds, David Brady, and David R. Smith. Metamaterial apertures for computational imaging. *Science*, 339(6117):310–313, 2013.

[37] A. Moffet. Minimum-redundancy linear arrays. *IEEE Transactions on Antennas and Propagation*, 16(2):172–175, 1968.

[38] R. J. Mailloux. *Phased Array Antenna Handbook*. Artech House, 2005.

[39] C. Ward, P. Hargrave, and J. McWhirter. A novel algorithm and architecture for adaptive digital beamforming. *IEEE Transactions on Antennas and Propagation*, 34(3):338–346, March 1986.

[40] Richard Obermeier and Jose Angel Martinez-Lorenzo. Sensing matrix design via mutual coherence minimization for electromagnetic compressive imaging applications. *IEEE Transactions on Computational Imaging*, 3(2):217–229, 2017.

[41] R. Feger, C. Wagner, S. Schuster, S. Scheiblhofer, H. Jager, and A. Stelzer. A 77-ghz fmcw mimo radar based on an sige single-chip transceiver. *IEEE Transactions on Microwave Theory and Techniques*, 57(5):1020–1035, May 2009.

[42] J. Li and P. Stoica. Mimo radar with colocated antennas. *IEEE Signal Processing Magazine*, 24(5):106–114, Sep. 2007.

[43] Sherif Sayed Ahmed, Andreas Schiessl, Frank Gumbmann, Marc Tiebout, Sebastian Methfessel, and Lorenz-Peter Schmidt. Advanced microwave imaging. *IEEE Microwave Magazine*, 13(6):26–43, 2012.

[44] Sherif Sayed Ahmed, Andreas Schiessl, and Lorenz-Peter Schmidt. A novel fully electronic active real-time imager based on a planar multistatic sparse array. *IEEE Transactions on Microwave Theory and Techniques*, 59(12):3567–3576, 2011.

[45] A. R. Thompson, J. M. Moran, and G. W. Swenson. *Interferometry and Synthesis in Radio Astronomy*. John Wiley and Sons, 2001.

[46] Max Born and Emil Wolf. *Principles of optics*. Cambridge Univ. Pr., 1999.

[47] P. H. van Cittert. Die wahrscheinliche schwingungsverteilung in einer von einer lichtquelle direkt oder mittels einer linse beleuchteten ebene. *Physica*, 1:201–210, 1934.

[48] F. Zernike. The concept of degree of coherence and its application to optical problems. *Physica*, 5:785–795, 1938.

[49] L. Yujiri, M. Schoucri, and P. Moffa. Passive millimeter-wave imaging. *IEEE Microwave Magazine*, 4:39–50, 2003.

[50] Neil A. Salmon, Rod Macpherson, Andy Harvey, Peter Hall, Steve Hayward, Peter Wilkinson, and Chris Taylor. First video rate imagery from a 32-channel 22-ghz aperture synthesis passive millimetre wave imager. *Proceedings of SPIE*, 8188, 2011.

[51] Neil A. Salmon, Rod Macpherson, Andy Harvey, Peter Hall, Steve Hayward, Peter Wilkinson, and Chris Taylor. First video rate imagery from a 32-channel 22-GHz aperture synthesis passive millimetre wave imager. In *Proceedings of SPIE Eur. Security + Defence, Millim. Wave, Terahertz Sens. Technol. IV*, volume 8188, pages 1 – 12, 2011.

[52] James J Condon and Scott M Ransom. *Essential radio astronomy*. Princeton Series in Modern Observational Astronomy. Princeton University Press, Princeton, NJ, April 2016.

[53] Nanbo Jin and Yahya Rahmat-Samii. Analysis and particle swarm optimization of correlator antenna arrays for radio astronomy applications. *IEEE Transactions on Antennas and Propagation*, 56(5):1269–1279, 2008.

[54] Aaron V. Diebold, Mohammadreza F. Imani, Timothy Sleasman, and David R. Smith. Phaseless coherent and incoherent microwave ghost imaging with dynamic metasurface apertures. *Optica*, 5(12):1529–1541, Dec 2018.

[55] Stavros Vakalis and Jeffrey A. Nanzer. Distributed array transmitter spatial coherence in active incoherent millimeter-wave imaging. In *2020 IEEE International Symposium on Antennas and Propagation and North American Radio Science Meeting*, pages 1169–1170, 2020.

[56] Rony Komissarov, Vitali Kozlov, Dmitry Filonov, and Pavel Ginzburg. Partially coherent radar unties range resolution from bandwidth limitations. *Nature Communications*, 10(1423), Dec. 2019.

[57] R. M. Narayanan and M. Dawood. Doppler estimation using a coherent ultrawide-band random noise radar. *IEEE Transactions on Antennas and Propagation*, 48(6):868–878, Jun 2000.

[58] David L. Donoho and Michael Elad. Optimally sparse representation in general (nonorthogonal) dictionaries via l1 minimization. *Proceedings of the National Academy of Sciences*, 100(5):2197–2202, 2003.

[59] Mark H. Wieringa. An investigation of the telescope based calibration methods 'redundancy' and 'self-cal'. *Experimental Astronomy*, 2(4):203–225, Jul 1992.

[60] E. W. Marchand and E. Wolf. Angular correlation and the far-zone behavior of partially coherent fields$*$. *Journal of the Optical Society of America*, 62(3):379–385, Mar. 1972.

[61] W. N. Christiansen and J. A. Hogbom. *Radiotelescopes*. Cambridge University Press, 1969.

[62] Larry Yujiri, Hiroshi H. Agravante, Mike Biedenbender, G. Samuel Dow, Martin R. Flannery, Steven W. Fornaca, Bruce I. Hauss, Ronald L. Johnson, Roger T. Kuroda, Karen Jordan, Paul S. Lee, Dennis Lo, Bill H. Quon, Arlen W. Rowe, Thomas K. Samec, Merit Shoucri, Karen E. Yokoyama, and John Yun. Passive millimeter-wave camera. *Proceedings of SPIE*, 3064:3064 – 3064 – 8, 1997.

[63] Jonathan Drewes and Robert P.Daly. Design of a high-resolution passive millimeter-wavelength camera for security applications. *Proceedings of SPIE*, 7309:7309 – 7309 – 12, 2009.

[64] Hitoshi Nohmi, Seiki Ohnishi, and Osamu Kujubu. Passive millimeter-wave camera with interferometric processing. *Proceedings of SPIE*, 6548:6548 – 6548 – 8, 2007.

[65] V. M. Patel and J. N. Mait. Passive millimeter-wave imaging with extended depth of field and sparse data. In *2012 IEEE International Conference on Acoustics, Speech and Signal Processing (ICASSP)*, pages 2521–2524, March 2012.

[66] Daniel Becker, James Beall, Hsiao-Mei Cho, William Duncan, Gene Hilton, Rob Horansky, Kent Irwin, Peter Lowell, Michael Niemack, Nick Paulter, Carl Reintsema, Frank Schima, Robert Schwall, Ki Won Yoon, Peter Ade, Carole Tucker, Simon Dicker, and Mark Halpern. A 350-ghz high-resolution high-sensitivity passive video imaging system. *Proceedings of SPIE*, 7670:7670 – 7670 – 7, 2010.

[67] Tekbaş Mustafa Işiker Hakan, Ünal İlhami and Özdemir Caner. An auto-classification procedure for concealed weapon detection in millimeter-wave radiometric imaging systems. *Microwave and Optical Technology Letters*, 60(3):583–594.

[68] Nanbo Jin and Yahya Rahmat-Samii. Advances in particle swarm optimization for antenna designs: Real-number, binary, single-objective and multiobjective implementations. *IEEE Transactions on Antennas and Propagation*, 55(3):556–567, 2007.

[69] B. Gonzalez-Valdes, G. Allan, Y. Rodriguez-Vaqueiro, Y. Álvarez, S. Mantzavinos, M. Nickerson, B. Berkowitz, J. A. Martı´nez-Lorenzo, F. Las-Heras, and C. M. Rappaport. Sparse array optimization using simulated annealing and compressed sensing for near-field millimeter wave imaging. *IEEE Transactions on Antennas and Propagation*, 62(4):1716–1722, April 2014.

[70] Adrian Liu, Max Tegmark, Scott Morrison, Andrew Lutomirski, and Matias Zaldarriaga. Precision calibration of radio interferometers using redundant baselines. *Monthly Notices of the Royal Astronomical Society*, 408(2):1029–1050, Oct. 2010.

[71] A. Camps, J. Bara, I. C. Sanahuja, and F. Torres. The processing of hexagonally sampled signals with standard rectangular techniques: application to 2-d large aperture synthesis interferometric radiometers. *IEEE Transactions on Geoscience and Remote Sensing*, 35(1):183–190, Jan 1997.

[72] Y. He and J. Papapolymerou. Conformal antipodal vivaldi antenna with parasitic elements for 5g millimeter wave applications. In *IEEE International Symposium on Antennas and Propagation*, July 2019.

[73] D. C. Thompson, O. Tantot, H. Jallageas, G. E. Ponchak, M. M. Tentzeris, and J. Papapolymerou. Characterization of liquid crystal polymer (lcp) material and transmission lines on lcp substrates from 30 to 110 ghz. *IEEE Transactions on Microwave Theory and Techniques*, 52(4):1343–1352, April 2004.

[74] C. Zheng, X. Yao, A. Hu, and J. Miao. A passive millimeter-wave imager used for concealed weapon detection. *Progress In Electromagnetics Research B*, 46:379–397, 2013.

[75] A. B. Tanner and C. T. Swift. Calibration of a synthetic aperture radiometer. *IEEE Transactions on Geoscience and Remote Sensing*, 31(1):257–267, Jan 1993.

[76] J. A. Nanzer and R. L. Rogers. A ka-band correlation radiometer for human presence detection from a moving platform. In *2007 IEEE/MTT-S International Microwave Symposium*, pages 385–388, 2007.

[77] L. Yujiri, M. Shoucri, and P. Moffa. Passive millimeter wave imaging. *IEEE Microwave Magazine*, 4(3):39–50, Sep. 2003.

[78] Stavros Vakalis and Jeffrey A. Nanzer. Impact of time-bandwidth product on active incoherent millimeter-wave imaging. In *2021 IEEE International Symposium on Antennas and Propagation and USNC-URSI Radio Science Meeting (APS/URSI)*, pages 1835–1836, 2021.

[79] Alan B. Tanner, William J. Wilson, Bjorn H. Lambrigsten, Steve J. Dinardo, Shannon T. Brown, Pekka P. Kangaslahti, Todd C. Gaier, Christopher S. Ruf, Steven M. Gross, Boon H. Lim, Stephen B. Musko, Steven A. Rogacki, and Jeff R. Piepmeier. Initial results of the geostationary synthetic thinned array radiometer (geostar) demonstrator instrument. *IEEE Transactions on Geoscience and Remote Sensing*, 45(7):1947–1957, 2007.

[80] Stavros Vakalis and Jeffrey A. Nanzer. A digital interferometric array with active noise illumination for millimeter-wave imaging at 13.7 fps. In *2020 IEEE/MTT-S International Microwave Symposium (IMS)*, pages 1141–1144, 2020.

[81] Antonin Chambolle. An algorithm for total variation minimization and applications. *Journal of Mathematical Imaging and Vision*, 20(1–2):89–97, Jan. 2004.

[82] C. Sturm and W. Wiesbeck. Waveform design and signal processing aspects for fusion of wireless communications and radar sensing. *Proceedings of the IEEE*, 99(7):1236–1259, Jul. 2011.

[83] M. G. Amin, Y. D. Zhang, F. Ahmad, and K. C. D. Ho. Radar signal processing for elderly fall detection: The future for in-home monitoring. *IEEE Signal Processing Magazine*, 33(2):71–80, Mar. 2016.

[84] G. Li, H. Wu, G. Jiang, S. Xu, and H. Liu. Dynamic gesture recognition in the internet of things. *IEEE Access*, 7:23713–23724, 2019.

[85] E. Klinefelter and J. A. Nanzer. Interferometric radar for spatially-persistent gesture recognition in human-computer interaction. In *2019 IEEE Radar Conference (RadarConf)*, pages 1–5, 2019.

[86] Bryan Paul, Alex R. Chiriyath, and Daniel W. Bliss. Survey of rf communications and sensing convergence research. *IEEE Access*, 5:252–270, 2017.

[87] Manikanta Kotaru, Kiran Joshi, Dinesh Bharadia, and Sachin Katti. SpotFi: Decimeter Level Localization Using WiFi. *ACM SIGCOMM Computer Communication Review*, 45(4):269–282, August 2015.

[88] Fadel Adib and Dina Katabi. See through walls with WiFi! In *Proceedings of the ACM SIGCOMM 2013 conference on SIGCOMM*, SIGCOMM '13, pages 75–86, Hong Kong, China, August 2013. Association for Computing Machinery.

[89] K. Chetty, G. E. Smith, and K. Woodbridge. Through-the-wall sensing of personnel using passive bistatic wifi radar at standoff distances. *IEEE Transactions on Geoscience and Remote Sensing*, 50(4):1218–1226, Apr. 2012.

[90] Donny Huang, Rajalakshmi Nandakumar, and Shyamnath Gollakota. Feasibility and limits of wi-fi imaging. In *Proceedings of the 12th ACM Conference on Embedded Network Sensor Systems*, SenSys '14, page 266–279, New York, NY, USA, 2014. Association for Computing Machinery.

[91] Saandeep Depatla, Lucas Buckland, and Yasamin Mostofi. X-ray vision with only wifi power measurements using rytov wave models. *IEEE Transactions on Vehicular Technology*, 64(4):1376–1387, 2015.

[92] Chitra R. Karanam and Yasamin Mostofi. 3d through-wall imaging with unmanned aerial vehicles using wifi. In *Proceedings of the 16th ACM/IEEE International Conference on Information Processing in Sensor Networks*, IPSN '17, page 131–142, New York, NY, USA, 2017. Association for Computing Machinery.

[93] Philipp M. Holl and Friedemann Reinhard. Holography of wi-fi radiation. *Phys. Rev. Lett.*, 118:183901, May 2017.

[94] J. Guan, A. Paidimarri, A. Valdes-Garcia, and B. Sadhu. 3d imaging using mmwave 5g signals. In *2020 IEEE Radio Frequency Integrated Circuits Symposium (RFIC)*, pages 147–150, 2020.

[95] A. Valdes-Garcia, A. Paidimarri, and B. Sadhu. Hardware-software co-integration for configurable 5g mmwave systems. In *2020 IEEE Symposium on VLSI Technology*, pages 1–2, 2020.

[96] Junfeng Guan, Arun Paidimarri, Alberto Valdes-Garcia, and Bodhisatwa Sadhu. 3-d imaging using millimeter-wave 5g signal reflections. *IEEE Transactions on Microwave Theory and Techniques*, 69(6):2936–2948, Jun. 2021.

[97] Emmanuel J. Candes and Michael B. Wakin. An introduction to compressive sampling. *IEEE Signal Processing Magazine*, 25(2):21–30, 2008.

[98] Richard Obermeier and Jose Angel Martinez-Lorenzo. Sensing matrix design via mutual coherence minimization for electromagnetic compressive imaging applications. *IEEE Transactions on Computational Imaging*, 3(2):217–229, 2017.

[99] Julio Martin Duarte-Carvajalino and Guillermo Sapiro. Learning to sense sparse signals: Simultaneous sensing matrix and sparsifying dictionary optimization. *IEEE Transactions on Image Processing*, 18(7):1395–1408, 2009.

[100] D. Kundur and D. Hatzinakos. Blind image deconvolution. *IEEE Signal Processing Magazine*, 13(3):43–64, 1996.

[101] J. Hasch, E. Topak, R. Schnabel, T. Zwick, R. Weigel, and C. Waldschmidt. Millimeter-wave technology for automotive radar sensors in the 77 ghz frequency band. *IEEE Transactions on Microwave Theory and Techniques*, 60(3):845–860, Mar. 2012.

[102] Flora Zidane, Jérôme Lanteri, Laurent Brochier, Nadine Joachimowicz, Hélène Roussel, and Claire Migliaccio. Damaged apple sorting with mmwave imaging and nonlinear support vector machine. *IEEE Transactions on Antennas and Propagation*, 68(12):8062–8071, Dec. 2020.

[103] Saptarshi Mukherjee, Lalita Udpa, Satish Udpa, Edward J. Rothwell, and Yiming Deng. A time reversal-based microwave imaging system for detection of breast tumors. *IEEE Transactions on Microwave Theory and Techniques*, 67(5):2062–2075, May 2019.

[104] N. A. Salmon. 3-d radiometric aperture synthesis imaging. *IEEE Transactions on Microwave Theory and Techniques*, 63(11):3579–3587, Nov. 2015.

[105] Joseph Rosen and Amnon Yariv. Three-dimensional imaging of random radiation sources. *Optics Letters*, 21(14):1011–1013, Jul. 1996.

[106] B. Ku, P. Schmalenberg, O. Inac, O. D. Gurbuz, J. S. Lee, K. Shiozaki, and G. M. Rebeiz. A 77–81-ghz 16-element phased-array receiver with $\pm 50^{\circ}$ beam scanning for advanced automotive radars. *IEEE Transactions on Microwave Theory and Techniques*, 62(11):2823–2832, Nov. 2014.

[107] Aaron V. Diebold, John B. Pendry, Alberto Favaro, Mohammadreza F. Imani, and David R. Smith. Spatial coherence in 2d holography. *Journal of the Optical Society of America A*, 38(5):727–736, May 2021.